

Final Report
AE 432 – Flight Dynamics and Control
Terrific Trio
F-4 Phantom Trim 2

Alex Joby, Gabriel Rodriguez, Sierra Simmons

Contents

Abstract.....	3
Simulation Development and Open-Loop Analysis.....	3
Aircraft Overview	3
F-4 Trim Characteristics and Nonlinear Simulation Development	5
Initial Trim Condition Test	5
Nonlinear Simulations of Control Input Doublets	9
Linear Model Development	23
Stability Derivatives.....	23
Longitudinal Linearized Model	23
Lateral Linearized Model	24
Linearized Simulations of Control Input Doublets.....	26
Stability Augmentation System	42
Open-Loop and Closed-Loop Comparison	42
Resulting Longitudinal and Lateral Stability Augmentation Systems.....	43
Linear Open-Loop and Closed-Loop Simulations.....	44
Nonlinear Open-Loop and Closed-Loop Simulations	49
Autopilot Control Design	59
Roll Control Autopilot	59
Heading Hold Autopilot.....	61
Roll and Sideslip Control Autopilot.....	64
Altitude Hold Autopilot	65
Velocity Hold Autopilot	68
Altitude and Velocity Hold Autopilot	71
Waypoint Navigation	75
Waypoint Navigation Overview and Control Implementation	75
Simulation Results and Controller Performance	75
Conclusion	79
Appendix	80
References	82

Abstract

The McDonnell Douglas F-4 Phantom II is not only an iconic aircraft, but one that can be investigated for its desirable flight characteristics and evident success on the battlefield. Enclosed in this final report, the Terrific Trio details various investigations into the F4. First, the trim conditions are determined and tested in the full nonlinear model of the aircraft, evaluating the flight characteristics when set at trim conditions and when inducing oscillations using control surface and thrust doublets. The linearized longitudinal and lateral models of the aircraft are then developed, and their responses and simulations compared with the nonlinear model. Second, the aircraft modes are investigated, stability augmentation system goals are set, and longitudinal and lateral stability augmentation systems are created. They are first tested on the mode approximations, then the full linear models, and finally the nonlinear model of the aircraft. Third, four different autopilots are designed to control the aircraft. They include a roll control, heading hold, velocity hold, and altitude hold autopilots. They are first tested in isolation on the linearized models, then in conjunction on the linearized models. Lastly, the created autopilots were integrated into the nonlinear model and tasked with a waypoint following mission. After extensive tuning, the aircraft was not able to follow the waypoints, and needs better controls systems.

Simulation Development and Open-Loop Analysis

Aircraft Overview

The McDonnell Douglas F-4 Phantom II, shown in Figure 3-1, is a name synonymous with power and Cold War might. Engineered with the need for a supersonic, all-weather interceptor for the US Navy, the F-4's design dared to be different. Its unconventional tandem seating and twin engines, while initially met with skepticism, proved to be its strength. Nicknamed the "Double Ugly" for its unconventional looks, it became a versatile warrior, adept at both air-to-air combat and air-to-ground attack, leaving its mark on numerous conflicts and earning a reputation as a workhorse of American airpower.



Figure 3-1: The McDonnell Douglas F-4 Phantom II

With a max speed of Mach 2.2 [1], the F-4 dominated the skies with its speed and altitude advantage. Its long-range capabilities, fueled by internal tanks and the option for externals, ensured it could reach distant targets. Packed with cutting-edge avionics, including a powerful pulse-Doppler radar and advanced navigation systems [2], the F-4 pilots had a keen eye on the battlefield. This technological marvel could carry a diverse arsenal, from bombs and missiles to rockets, adapting to any mission thrown its way.

However, the F-4 wasn't without its limitations. Its size made it a lumbering giant in dogfights, vulnerable to more agile opponents. The McDonnell Douglas F-4 Phantom II had its faults, including smoky engines and a hazardous, often fatal, stall-spin characteristic. Maintenance man-hours were high, and cockpit ergonomics were poor [3].

Despite these shortcomings, the F-4's legacy is undeniable. With over 5,100 produced, it holds the title of the most-produced American supersonic jet fighter. It served in the Vietnam War, Yom Kippur War, Falklands War, and Gulf War, shaping air combat doctrines and showcasing American technological prowess. Today, preserved F-4s stand tall in museums, silent testaments to an era when this "Double Ugly" soared high, forever etching its name in aviation history. In this project's context, the aircraft's key characteristics needed to be defined for simulation and analysis. The following are some key properties of the Phantom:

Table 3-1: Key Mass and Geometry Properties of the McDonnell Douglas F-4 Phantom II

$V_T = 1742.6 \text{ [ft/s]}$	$h = 55,000 \text{ [ft]}$
$W = 39000 \text{ [lbs]}$	$S = 530.0 \text{ [ft}^2]$
$m = \text{[slugs]}$	$b = 38.7 \text{ [ft]}$
$I_x = 25,000 \text{ [slug}\cdot\text{ft}^2]$	$\bar{c} = 16.0 \text{ [ft]}$
$I_y = 122,200 \text{ [slug}\cdot\text{ft}^2]$	$\rho = 2.865 \times 10^{-4} \text{ [slug}/\text{ft}^3]$
$I_z = 139,800 \text{ [slug}\cdot\text{ft}^2]$	$a = 968.1 \text{ [ft/s]}$
$I_{xz} = 2,200 \text{ [slug}\cdot\text{ft}^2]$	$M^* = 1.80$

Table 3-2: Key Aerodynamic Coefficients of the McDonnell Douglas F-4 Phantom II

$C_{L_0} = 0.010$	$C_{D_{Mach}} = -0.03$	$\bar{C}_{n_p} = 0.0$
$C_{D_0} = 0.0439$	$C_{m_{Mach}} = -0.10$	$\bar{C}_{Y_r} = 0.0$
$C_{m_0} = 0.025$	$C_{L_{\delta_e}} = 0.25$	$\bar{C}_{l_r} = 0.040$
$C_{L_\alpha} = 2.80$	$C_{D_{\delta_e}} = -0.15$	$\bar{C}_{n_r} = -0.260$
$C_{D_\alpha} = 0.40$	$C_{m_{\delta_e}} = -0.380$	$C_{Y_{\delta_a}} = -0.010$
$C_{m_\alpha} = -0.780$	$C_{Y_\beta} = -0.70$	$C_{l_{\delta_a}} = 0.0150$
$\bar{C}_{L_\alpha} = 0.17$	$C_{l_\beta} = -0.025$	$C_{n_{\delta_a}} = -0.0009$
$\bar{C}_{m_\alpha} = -0.25$	$C_{n_\beta} = 0.09$	$C_{Y_{\delta_r}} = 0.05$

$\bar{C}_{L_q} = 1.30$	$\bar{C}_{Y_p} = 1.30$	$C_{l_{\delta_r}} = 0.0030$
$\bar{C}_{m_q} = -2.0$	$\bar{C}_{l_p} = 1.30$	$C_{n_{\delta_r}} = -0.025$
$C_{L_{Mach}} = -0.10$	-----	-----

F-4 Trim Characteristics and Nonlinear Simulation Development

The F-4 was manufactured with two General Electric J-79-GE-15s, with a maximum thrust of 17,000 [lbs] each. Thus, taking this and the given trim condition parameters, mass/geometry properties, and aerodynamic coefficients, a model of the system could begin to be created. Given that only two of the five trim conditions were given, the remaining three values were found. Using the three longitudinal trim equations:

$$T^* + (C_L^* Q_w^* S_w) \sin(\alpha^*) - (C_D^* Q_w^* S_w) \cos(\alpha^*) - mg \sin(\alpha^* + \gamma^*) = 0$$

$$-(C_L^* Q_w^* S_w) \cos(\alpha^*) - (C_D^* Q_w^* S_w) \sin(\alpha^*) + mg \cos(\alpha^* + \gamma^*) = 0$$

$$C_m^* Q_w^* S_w \bar{C} = 0 \xrightarrow{\text{yields}} C_m^* = 0$$

Where the trim lift, drag, and moment aerodynamic coefficients are defined as:

$$\begin{aligned} C_L^* &= C_{L_0} + C_{L_\alpha} \alpha^* + C_{L_{\delta_e}} \delta_e^* \\ C_D^* &= C_{D_0} + C_{D_\alpha} \alpha^* + C_{D_{\delta_e}} \delta_e^* \\ C_m^* &= C_{m_0} + C_{m_\alpha} \alpha^* + C_{m_{\delta_e}} \delta_e^* \end{aligned}$$

The three nonlinear functions were solved using a MATLAB function for the remaining trim conditions.

Table 3-3: Trim Conditions

Trim Condition:	γ^* (degrees)	V_T^* (m/s)	α^* (degrees)	T^* (lbs)	δ_e^* (degrees)
Value:	0	1742.6	3.4593	17732	-3.3312

Using the given Simulink model, adjustments were made to model the F-4. First, the coefficients of lift, drag, and moment were edited to consider Mach effects. Second, the engine model was changed from a propeller to a jet engine. Last, the aerodynamic coefficients and mass/geometry properties were substituted in the MATLAB script. The simulation was then used for open-loop analysis in this configuration.

Initial Trim Condition Test

To verify the trim conditions tabulated in Table 3-3, a 100 second simulation was evaluated. The following plots characterize the trim simulation. The calculated longitudinal trim conditions and the result of their simulation are shown in Figures 3-2, 3-3, 3-4, 3-5, 3-6, and 3-7.

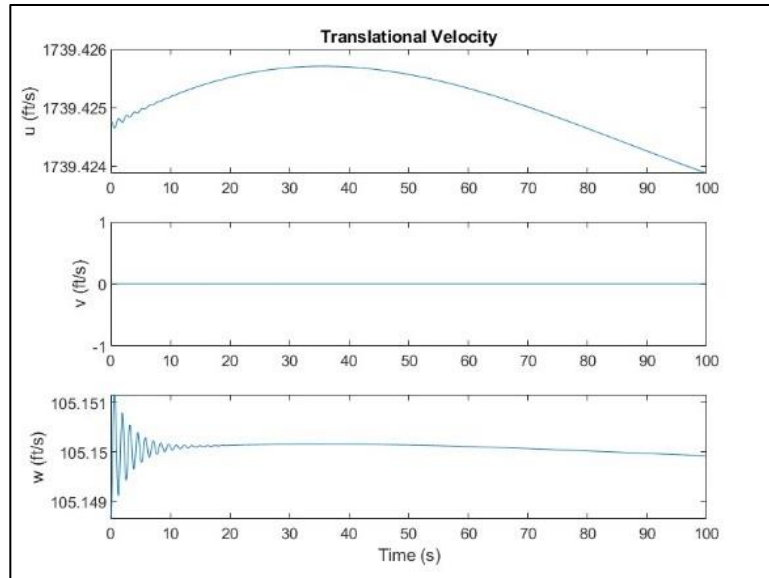


Figure 3-2: Translational Trim Velocities over Time.

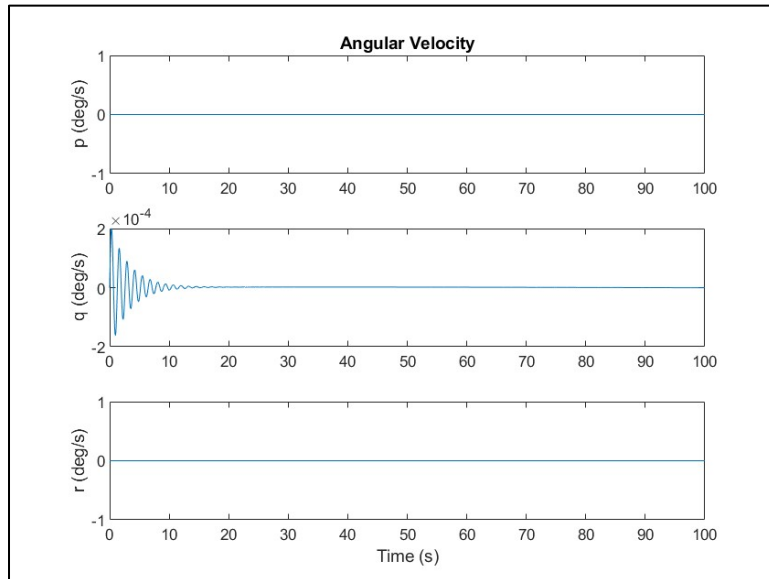


Figure 3-3: Angular Trim Velocities over Time.

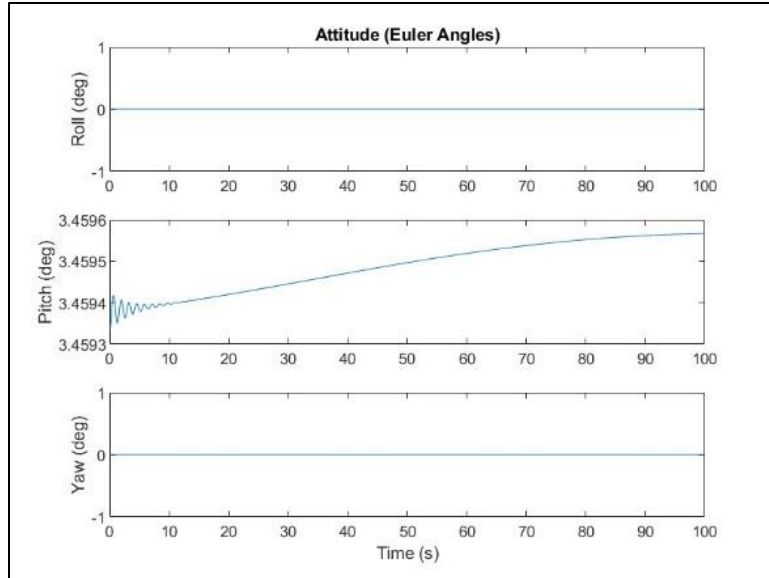


Figure 3-4: Trim Attitude (Euler Angles) over Time.

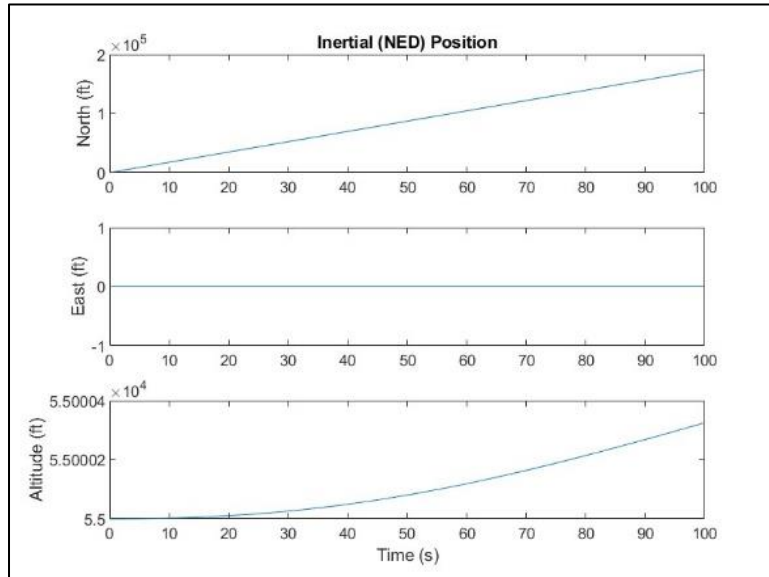


Figure 3-5: Trim Inertial (NED) Position over Time.

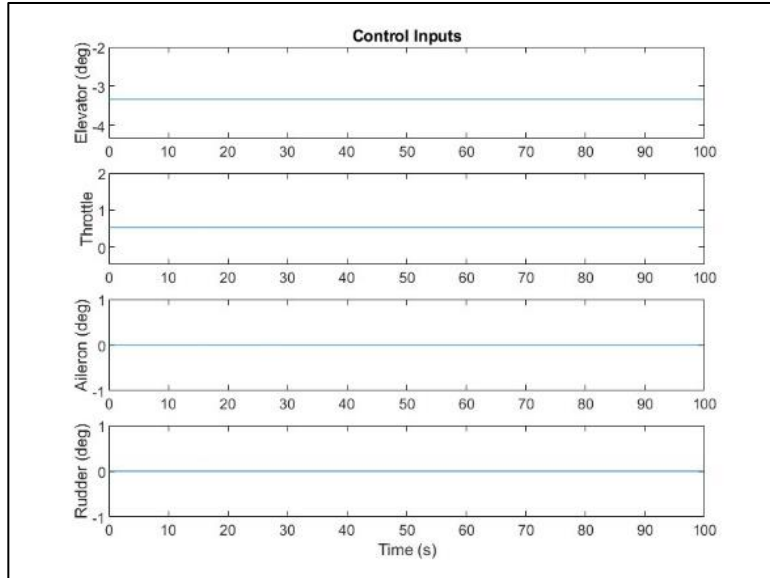


Figure 3-6: Inputs for Control Surfaces and Throttle.

4

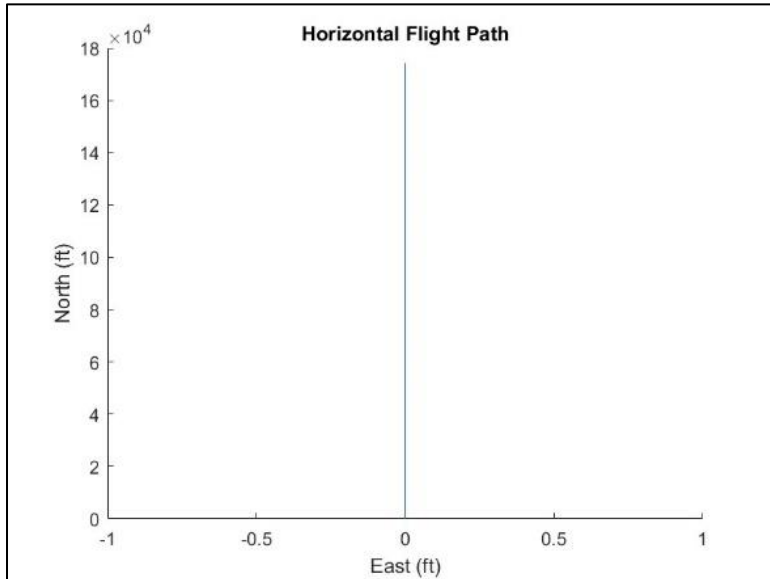


Figure 3-7: The Horizontal Flight Path at Trim Conditions.

After analyzing the 12 aircraft states and 4 control inputs, the calculated trim conditions were verified. All the aircraft states stayed roughly constant, other than the inertial position, which was expected to change. This was achieved without any changes in control input, meaning that trim has been achieved. As expected, the translational trim velocity from Figure 3-2, is roughly constant, verifying the calculated trim conditions. The angular velocity shown in Figure 3-3 produces negligibly small oscillations in pitch rate. Figure 3-4 shows the trim attitude, again with negligible oscillations. With small variations in pitch, the reason for the

slight altitude variation is evident; otherwise, the trim condition is held and verified. Disregarding the negligible change in altitude, the trim condition for inertial position from Figure 3-5, is again verified, traveling strictly North. The control inputs shown in Figure 3-6 are constant and only have nonzero values for the throttle and elevator controls, as expected.

Nonlinear Simulations of Control Input Doublets

Elevator Doublet

After verifying the trim conditions, doublet simulations commenced. The first was an elevator doublet which was conducted by deflecting the elevator half a degree from trim in either direction for 2 seconds each. If the aircraft is dynamically stable, it will return to trim over the 500 second simulation. The results of the 500 second elevator doublet simulation are shown in Figures 3-8, 3-9, 3-10, 3-11, 3-12, and 3-13.

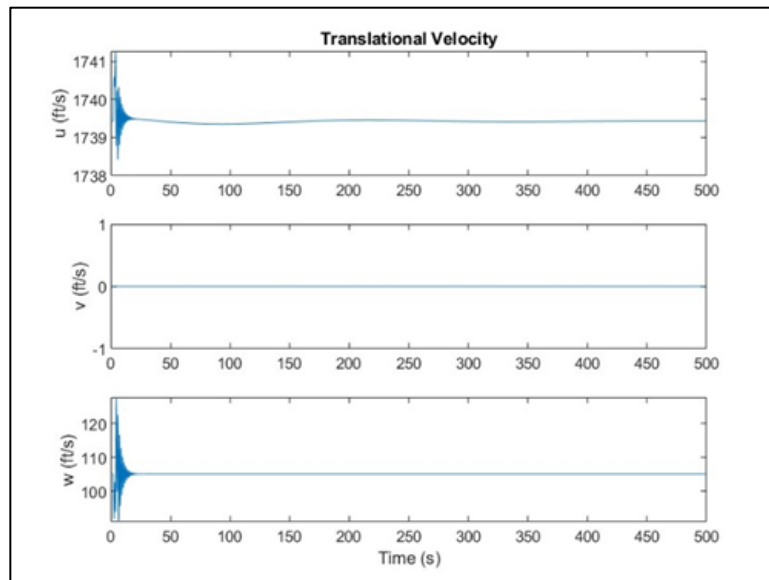


Figure 3-8: Translational Velocities for the Elevator Doublet.

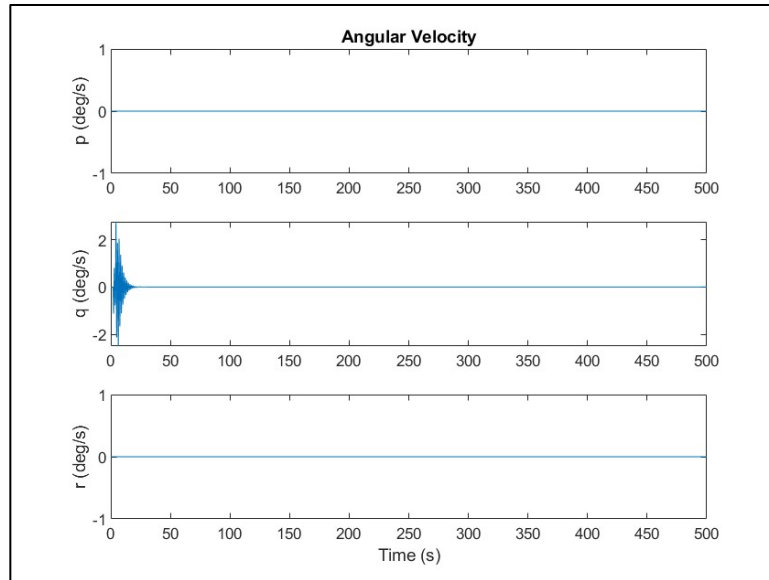


Figure 3-9: Angular Velocities for the Elevator Doublet.

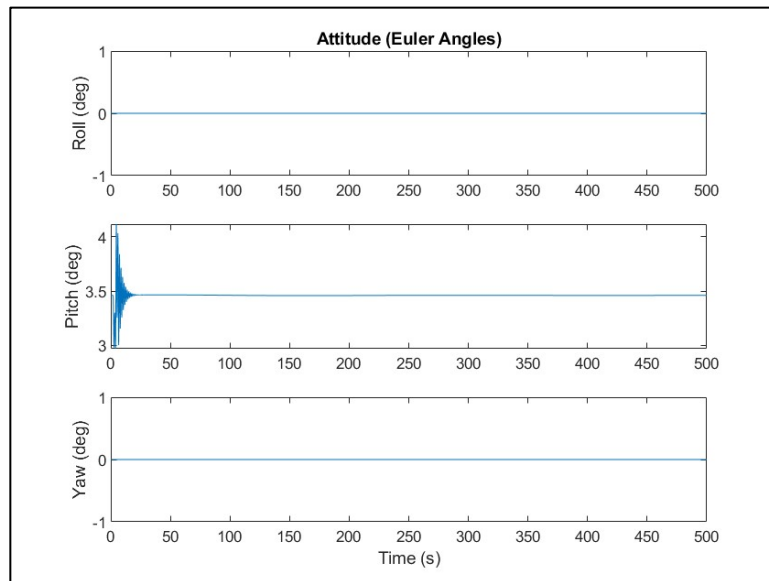


Figure 3-10: Aircraft Attitude for the Elevator Doublet.

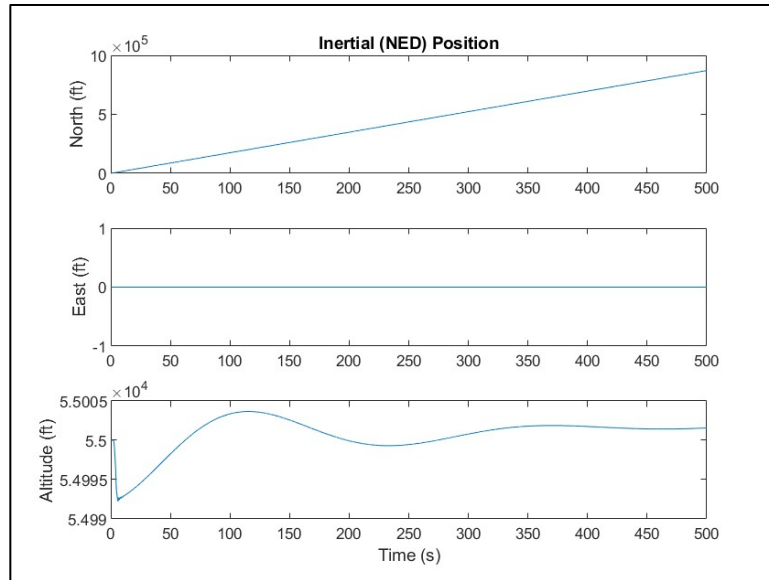


Figure 3-11: Inertial Position for the Elevator Doublet.

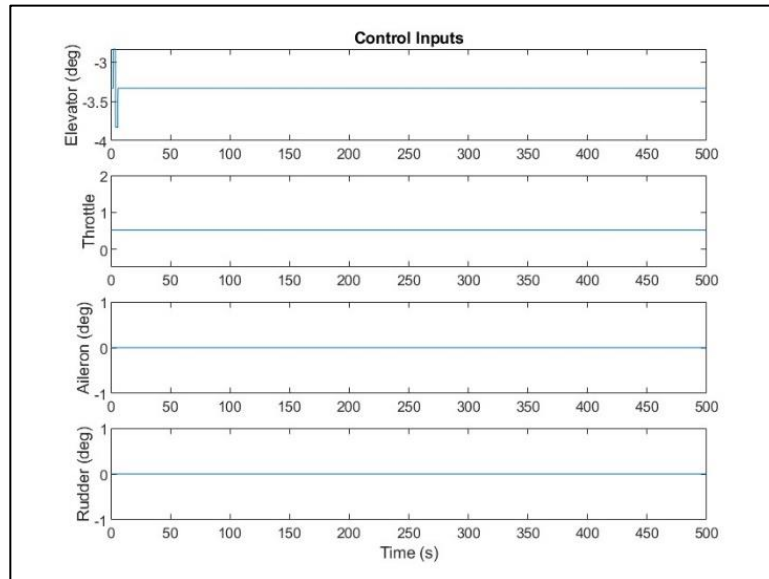


Figure 3-12: Control Inputs for the Elevator Doublet.

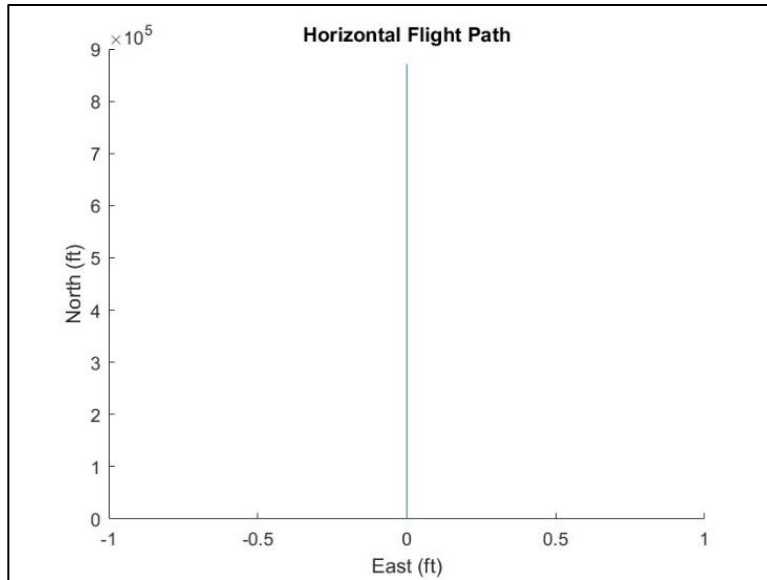


Figure 3-13: The Horizontal Flight Path for the Elevator Doublet.

In summation, deduced from the various figures, the elevator doublet induced small oscillations in the pitch and pitch rate. The elevator doublet excited the aircraft's short period mode, causing the oscillations. Essentially, the aircraft responded to the elevator control input with pitch, and the damping, primarily from the horizontal tail, allowed the aircraft to return to trim after the control input was returned to trim conditions.

Quickly analyzing each figure, Figure 3-8 shows small oscillations in the longitudinal components of the translational velocity. This is followed by the translational velocity returning to approximately trim conditions. Figure 3-9 shows the same short period oscillations, shown in the pitch rate variation for the first 20 seconds, after which it returns to trim conditions. Meanwhile, the roll and the yaw remain constant and are not affected by the elevator doublet. This is further reinforced by Figure 3-10, which shows small oscillations in pitch in the first 20 seconds while the yaw and roll are unaffected. The aircraft's direction is unaffected, but the altitude changes due to the doublet and becomes relatively constant after 350s at approximately 55,000ft, as shown in Figure 3-11. This result indicates that the phugoid mode was also excited by the elevator doublet. The doublet performed on the elevator is shown in Figure 3-12, with the only variation being in the elevator deflection, as expected.

Thrust Doublet

Next, a thrust doublet was simulated. The throttle was increased from trim for 10 seconds and decreased from trim for 10 seconds. The plotted results of this simulation can be found in Figures 3-14, 3-15, 3-16, 3-17, 3-18, and 3-19.

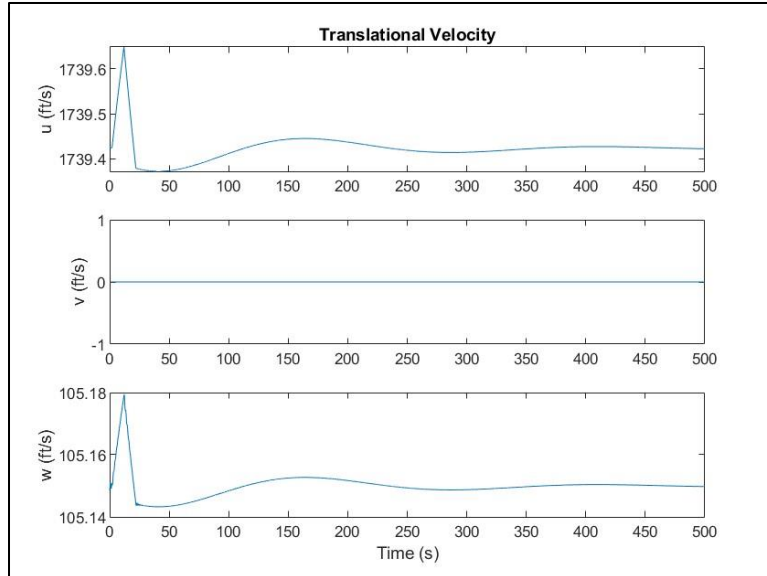


Figure 3-14: Translational Velocities for the Thrust Doublet.

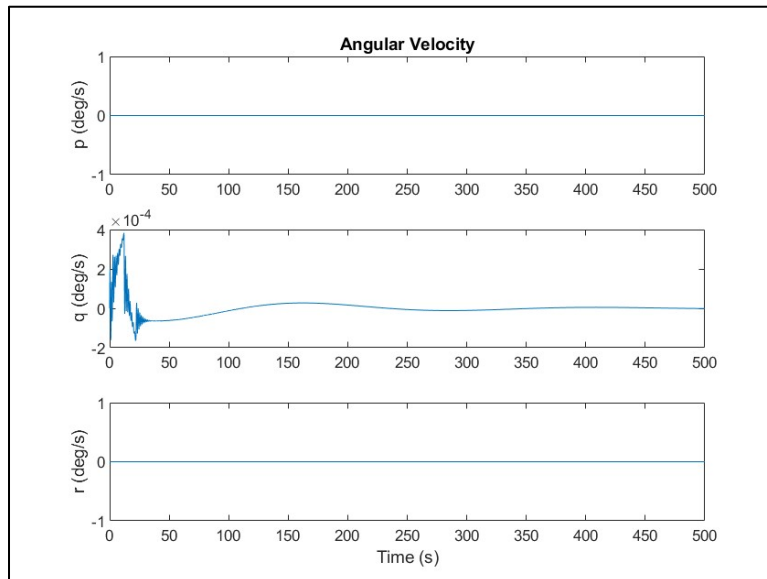


Figure 3-15: Angular Velocities for the Thrust Doublet.

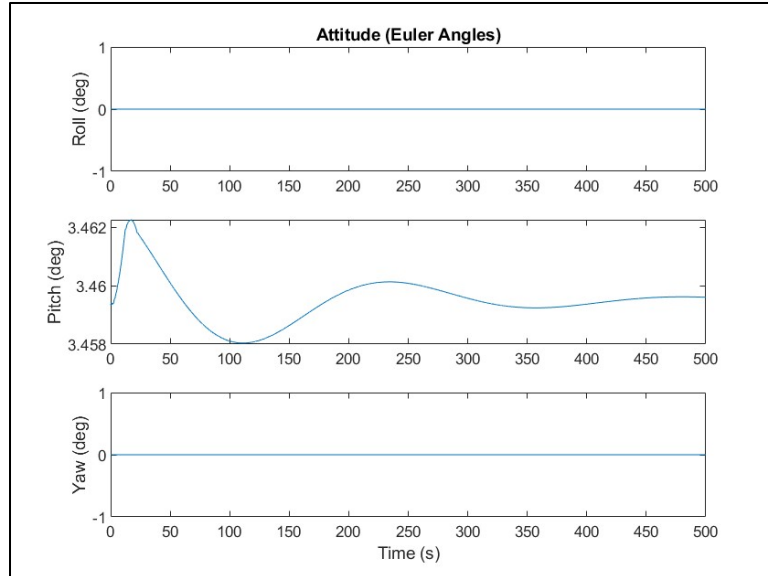


Figure 3-16: Aircraft Attitude for the Thrust Doublet.

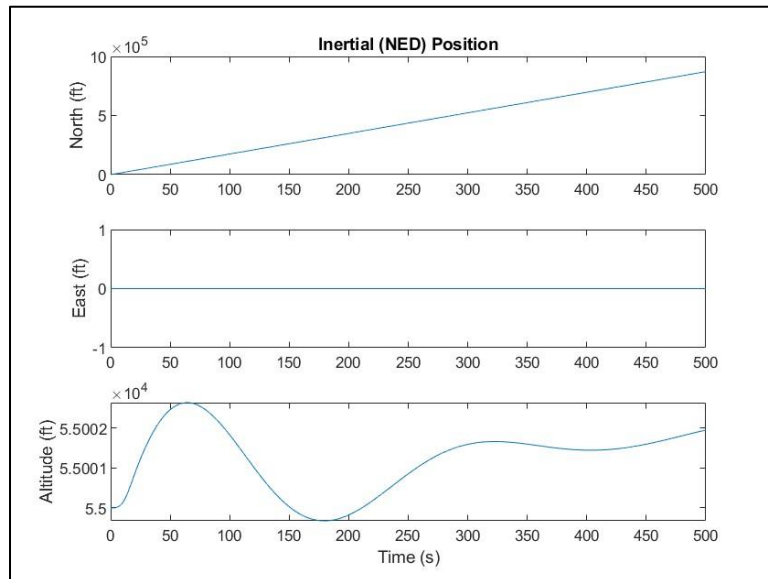


Figure 3-17: Inertial Position for the Thrust Doublet.

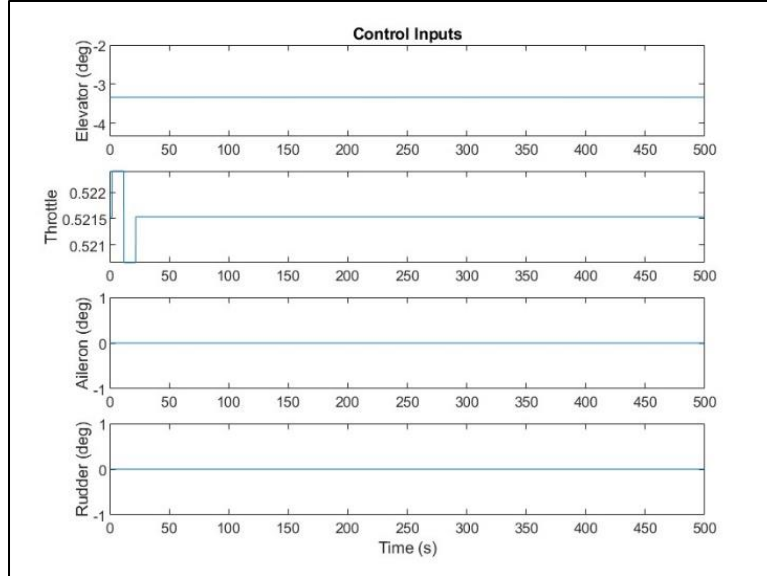


Figure 3-18: Control Inputs for the Thrust Doublet.

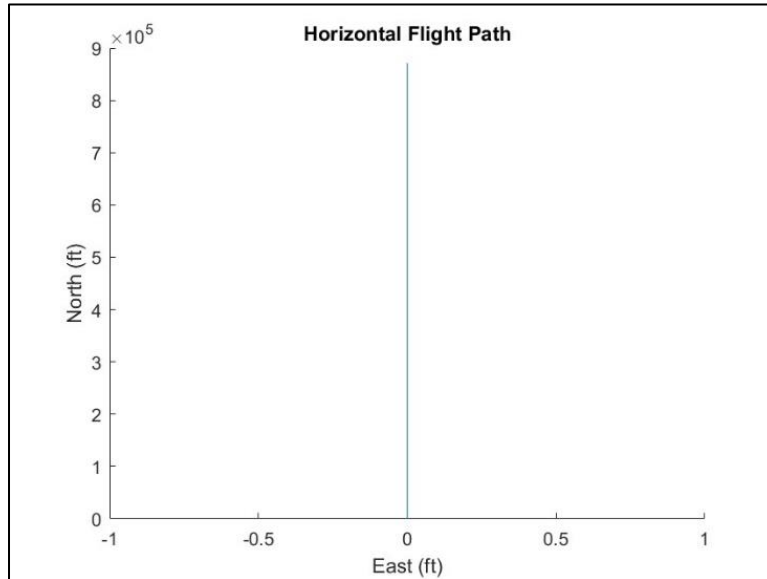


Figure 3-19: Inertial Position for the Thrust Doublet.

The important characteristics of the thrust doublet are expressed in the longitudinal variations. Evidently, as seen in Figure 3-14, there are noticeable changes in the velocity due to the change in thrust from the throttle control. The components of the change in velocity are only in the body frame X and Z directions because we are assuming the thrust of each engine is equal. The thrust vector, due to the positive angle of attack, has a downward component; thus, propelling the aircraft upward in the inertial frame. The aircraft also experiences an increase in lift due to the increased dynamic pressure from the increased velocity. This increase in lift increases the pitch up moment. Thus, when the thrust is increased, the aircraft experiences an increase in pitch rate, and when the thrust is decreased, the aircraft experiences a decrease in pitch rate.

These effects can be seen in Figure 3-15, where the change in pitch rate is shown, and in Figure 3-16, where the change in pitch is shown.

Due to the dynamic stability of the aircraft, the oscillatory reactions of aircraft from the thrust doublet were damped and the aircraft returned to trim conditions with a very low amplitude, long period oscillation in pitch (and therefore altitude) that is negligible when considering whether the aircraft is trimmed or not. It is also important to note that in the thrust doublet, as seen in Figure 3-18, the only control variable manipulated was the throttle control.

Aileron Doublet

The third simulation carried out on the supersonic F-4 model was an aileron doublet. Translational and angular velocities, attitude and inertial position are plotted over time and shown in Figures 3-20, 3-21, 3-21, 3-22 respectively. Figures 3-23, and 3-24 show the control input and resulting flight path.

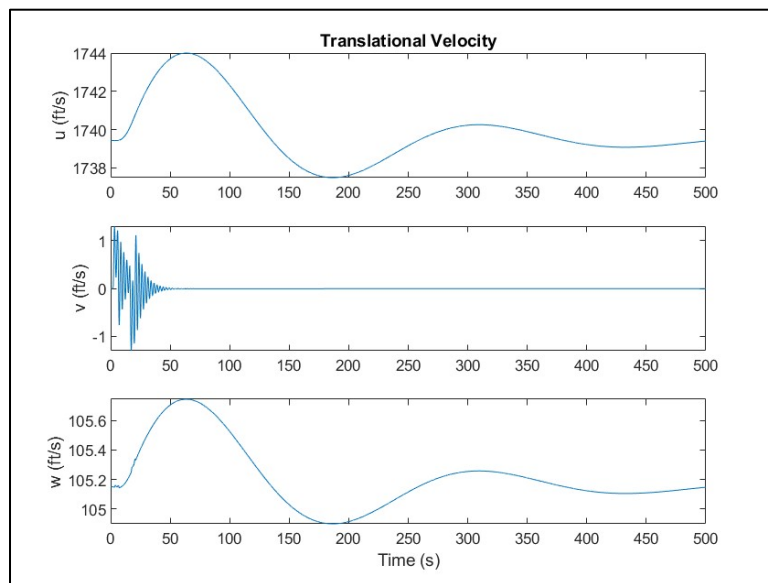


Figure 3-20: Translational Velocities for the Aileron Doublet.

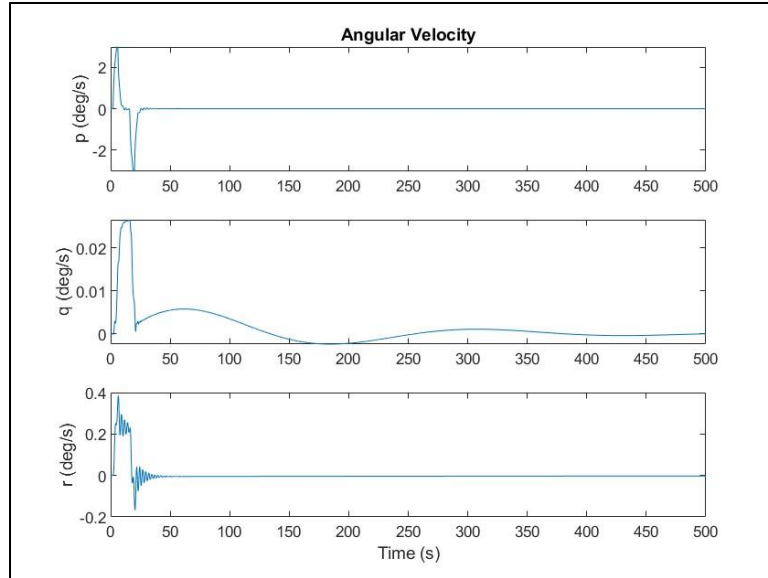


Figure 3-21: Angular Velocities for the Aileron Doublet.

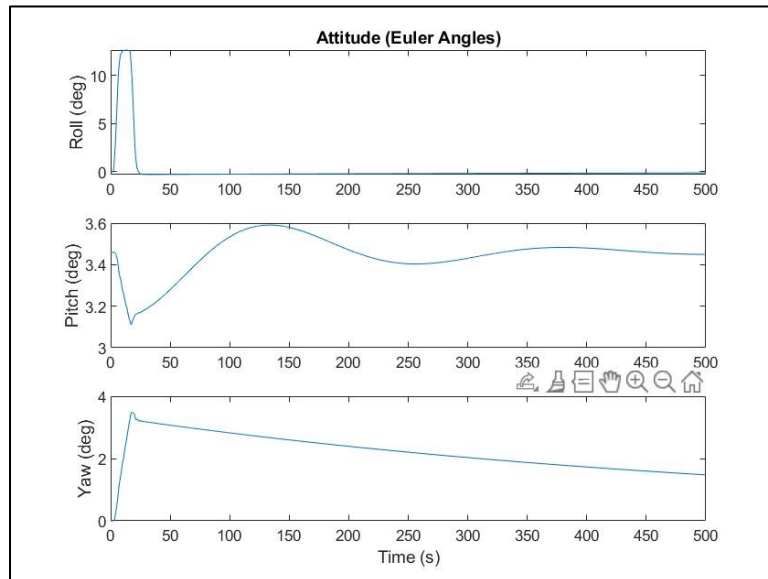


Figure 3-22: Attitude for the Aileron Doublet.

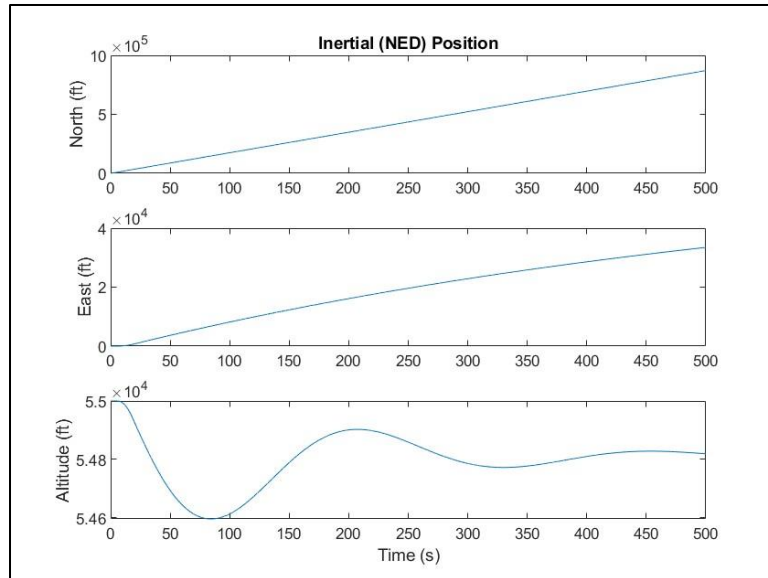


Figure 3-23: Inertial Position for the Aileron Deflection.

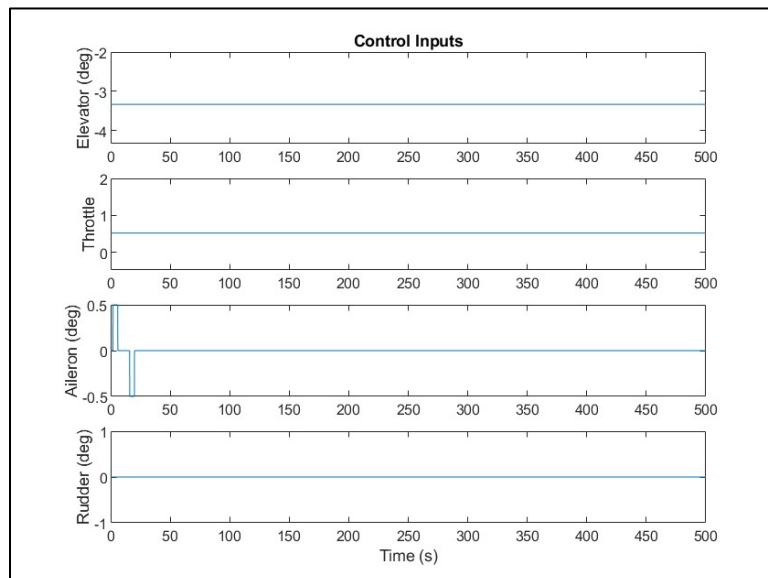


Figure 3-24: Control Inputs for the Aileron Deflection.

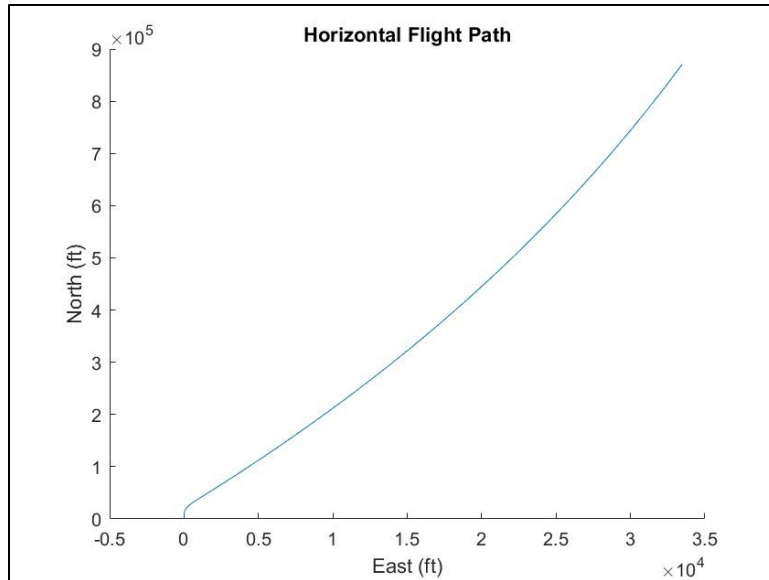


Figure 3-25: Horizontal Flight Path for the Aileron Doublet.

As seen in Figure 3-20, the aileron doublet affected all the translational velocities. The plots indicate that the Dutch roll and long period modes were excited by the aileron deflection, but were damped out, retuning the aircraft to trim conditions. The resulting heading was offset from the original, causing an eastern flight path direction, as seen in Figure 3-25. Verified by Figure 3-24, the only change in control input was from the aileron doublet. The aileron doublet again verifies the dynamic stability of the aircraft and the initial trim conditions.

Rudder Doublet

The fourth simulation carried out on the supersonic F-4 model was a rudder doublet. Translational and angular velocities, attitude and inertial position were plotted over time and shown in Figures 3-26, 3-27, 3-28, 3-29 respectively. Figures 3-30 and 3-31 show the control input and resulting flight path when the rudder was deflected.

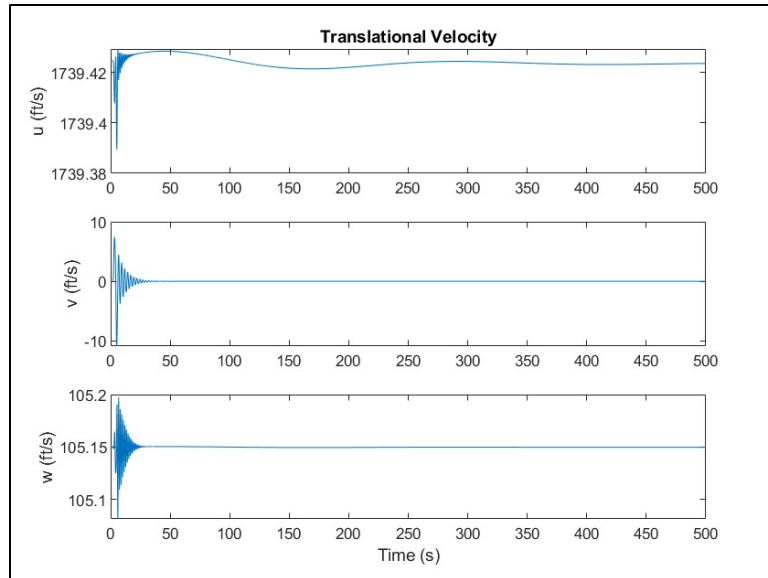


Figure 3-26: Translational Velocities for the Rudder Doublet.

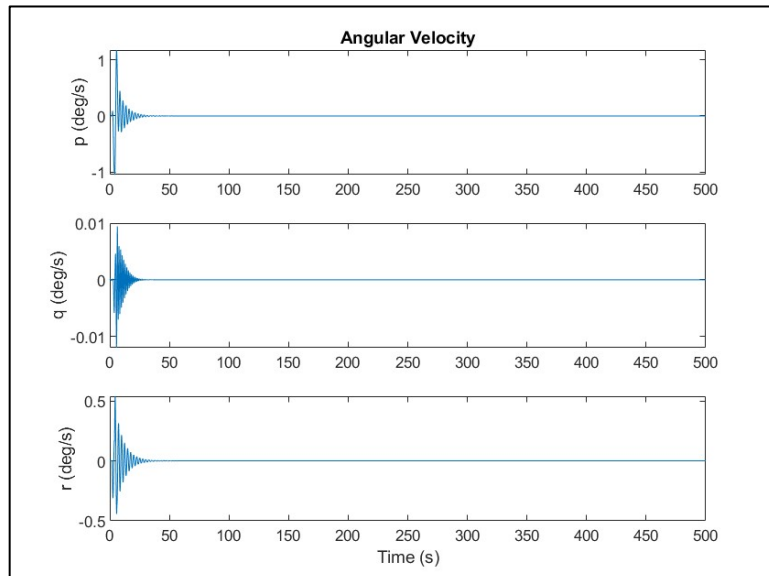


Figure 3-27: Angular Velocities for the Rudder Doublet.

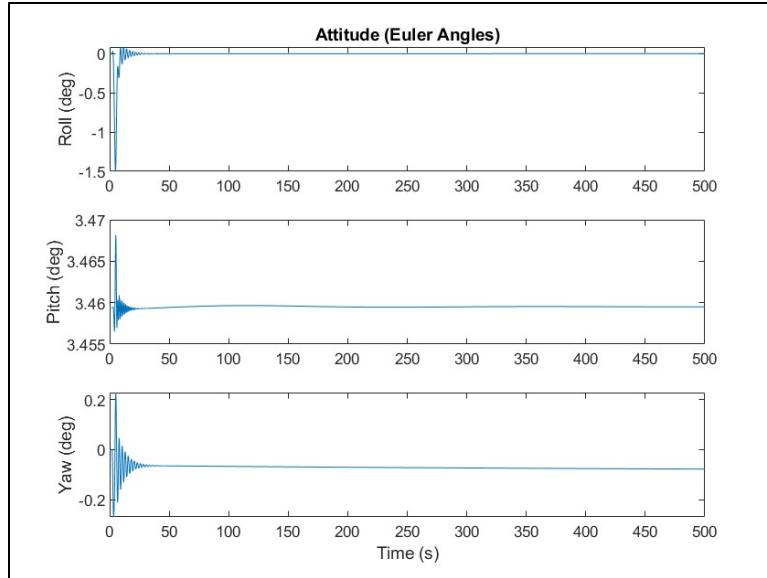


Figure 3-28: Aircraft Attitude for the Rudder Doublet.

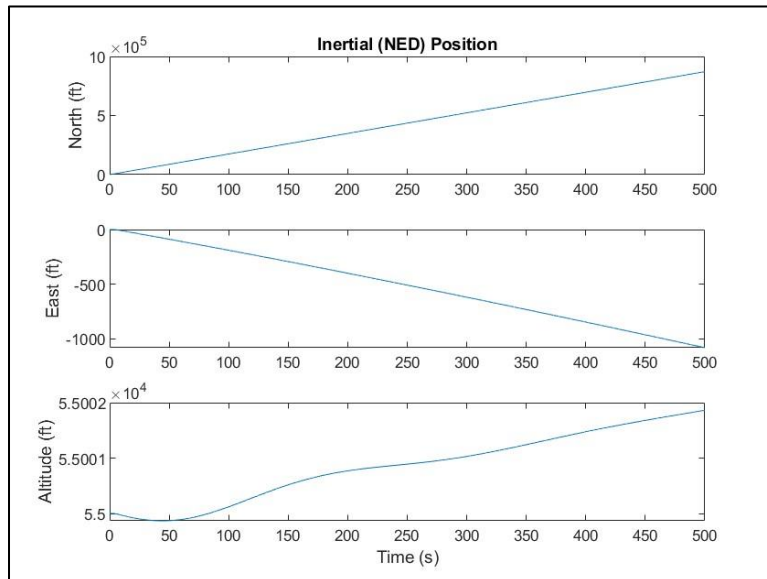


Figure 3-29: Inertial Position for the Rudder Doublet.

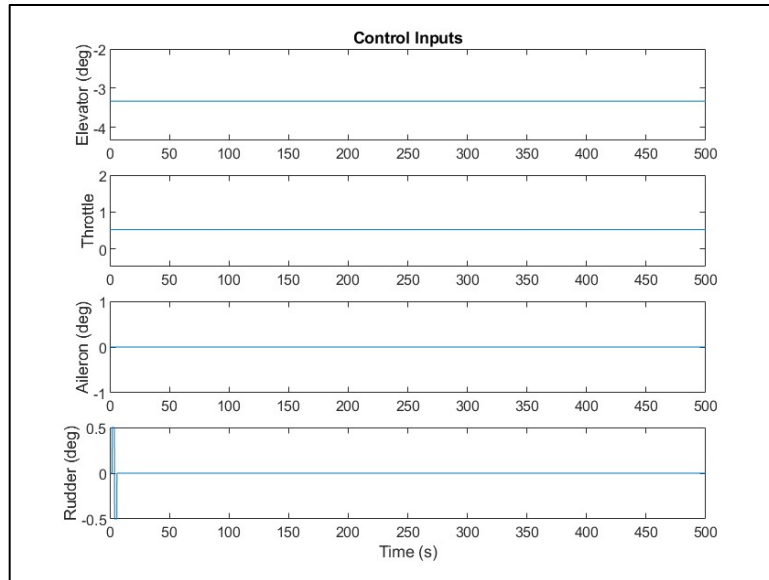


Figure 3-30: Control Inputs for the Rudder Doublet.

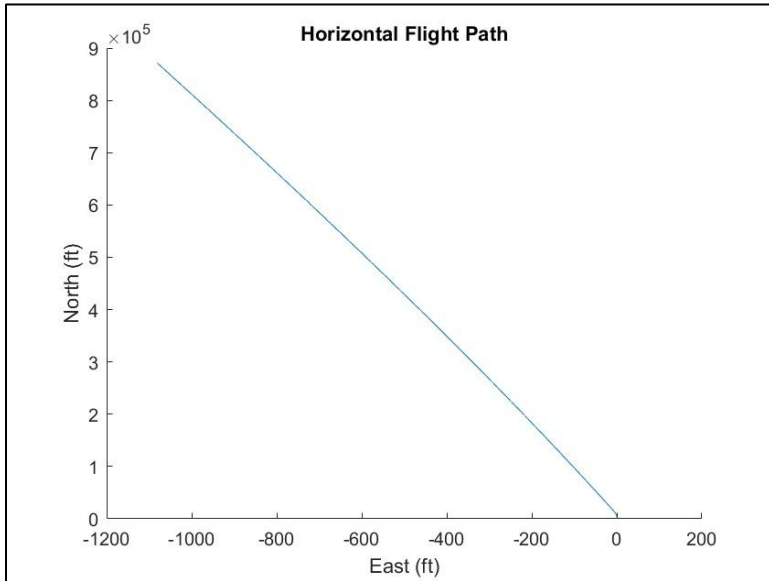


Figure 3-31: Horizontal Flight Path for the Rudder Doublet.

The rudder doublet caused oscillations from the Dutch roll mode, shown in the plot of translational velocities (Figure 3-26). The oscillations had small periods and were damped out and reverted quickly to original conditions. The quick change in roll, as shown in Figure 3-31, caused the aircraft to turn West, and the dampening allowed it to maintain the heading rather than head back to the original. Due to the rudder doublet minimally affecting the pitch, the altitude remained relatively constant as shown in Figure 3-29, but there was a very small force upwards that caused a small, yet gradual increase in altitude.

Linear Model Development

Stability Derivatives

To create the linearized longitudinal and lateral models of the F4, the stability derivatives needed to be calculated. Using MATLAB, the following stability derivatives were found:

Table 3-4: Longitudinal Stability Derivatives

$D_u = 0.0109 \text{ lbf/s}$ $L_u = 0.0163 \text{ lbf/s}$ $M_u = 9.3372e-04 \text{ lbf/s}$	$D_q = 0 \text{ lbf*ft/rad/s}$ $L_q = 1.134 \text{ lbf*ft/rad/s}$ $M_q = -0.2767 \text{ lbf*ft/rad/s}$	$D_{adot} = 0 \text{ lbf*ft/rad/s}$ $L_{adot} = 0.1483 \text{ lbf*ft/rad/s}$ $M_{adot} = -0.0346 \text{ lbf*ft/rad/s}$
$D_a = 44.661 \text{ lbf*ft/rad}$ $L_a = 545.605 \text{lbf*ft/rad}$ $M_a = -23.4598 \text{ lbf*ft/rad}$	$D_{de} = -28.4488 \text{ lbf*ft/rad}$ $L_{de} = 47.4147 \text{lbf*ft/rad}$ $M_{de} = -11.4292 \text{ lbf*ft/rad}$	$T_{dt} = 28.0718 \text{ lbf/rad}$ $T_u = 0 \text{ lbf/ft/s}$
$X_u = -.0099 \text{ lbf/ft/s}$ $X_a = -11.6577 \text{ lbf/rad}$ $X_q = 0.0684 \text{lbf/rad/s}$ $X_{de} = 31.258 \text{ lbf/rad}$ $X_{adot} = 0.0089 \text{ lbf/rad}$ $X_w = -0.0067 \text{ lbf/rad}$	$Z_u = -0.0169 \text{ lbf/ft/s}$ $Z_a = -547.306 \text{ lbf/rad}$ $Z_q = -1.1319 \text{ lbf/rad/s}$ $Z_{de} = -45.6117 \text{ lbf/rad}$ $Z_{adot} = -0.148 \text{ lbf/rad/s}$ $Z_w = -0.3146 \text{ lbf/rad}$	$X_{wdot} = 5.1441e-06 \text{ lbf/rad/s}$ $Z_{wdot} = -8.5096e-05 \text{ lbf/rad/s}$ $M_{wdot} = -1.9882e-05 \text{ lbf*ft/rad/s}$

Table 3-5: Lateral Stability Derivatives

$l_p = -0.7911 \text{ lbf/rad/s}$ $Y_p = 0 \text{ lbs/rad/s}$ $N_p = 0 \text{ lbs*ft/rad/s}$	$l_r = 0.1582 \text{ lbf*ft/rad/s}$ $Y_r = 0 \text{ lbf/rad/s}$ $N_r = -0.1839 \text{ lbf*ft/rad/s}$	$l_b = -8.8898 \text{ lbf*ft/rad}$ $Y_b = -132.761 \text{ lbf/rad}$ $N_b = 5.7231 \text{ lbf/rad}$
$l_{dr} = 1.0668 \text{ lbf*ft/rad}$ $Y_{dr} = 9.4829 \text{ lbf/rad}$ $N_{dr} = -1.5897 \text{ lbf*ft/rad}$	$l_{da} = 5.3339 \text{ lbf*ft/rad}$ $Y_{da} = -1.8966 \text{ lbf/rad}$ $N_{da} = -0.0572 \text{ lbf*ft/rad}$	$l_v = -0.0051 \text{ lbf/s}$ $Y_v = -0.0763 \text{ lbf/ft/s}$ $N_v = 0.0033 \text{ lbf/s}$

Longitudinal Linearized Model

The longitudinal stability derivatives shown in Tables 3-4 could formalize the A and B matrices for the longitudinal model.

$$A_{LONG} = \begin{bmatrix} -0.0099 & -0.0067 & -105.1 & -32.14 \\ -0.0169 & -0.3146 & 1739.4 & -1.943 \\ 9.3406e-04 & -0.0135 & -0.3112 & 3.862e-05 \\ 0 & 0 & 1 & 0 \end{bmatrix}$$

$$B_{LONG} = \begin{bmatrix} 31.3722 & 28.0718 \\ -45.7745 & 0 \\ -11.4700 & 0 \\ 0 & 0 \end{bmatrix}$$

Finding the eigenvalues of the A matrix, the long period and short period were found to be stable. The following are the resulting eigenvalues of the longitudinal model:

$$\begin{aligned}\lambda_{1,2} &= -0.3126 \pm 4.8594i \\ \lambda_{3,4} &= -0.0064 \pm 0.0257i\end{aligned}$$

Evidently, the first two eigenvalues correspond to the short-period mode, while the other two eigenvalues correspond to the long-period (phugoid) mode. The corresponding mode frequencies and damping ratios are the following:

$$\begin{aligned}\omega_{SP} &= 4.869 \left[\frac{\text{rad}}{\text{s}} \right], \zeta_{SP} = 0.064 \\ \omega_{LP} &= 0.02646 \left[\frac{\text{rad}}{\text{s}} \right], \zeta_{LP} = 0.241\end{aligned}$$

These frequencies and damping ratios correspond to Level 1 flying qualities in the long period/phugoid mode and Level 4 flying qualities in the short period mode. This can be due to normal shocks and the like at supersonic conditions. The following figure plots the longitudinal eigenvalues on real and imaginary axes. Due to their negative real part, which is apparent in the figure, both modes are stable. As expected, the short period has a larger imaginary part, resulting in a higher frequency.

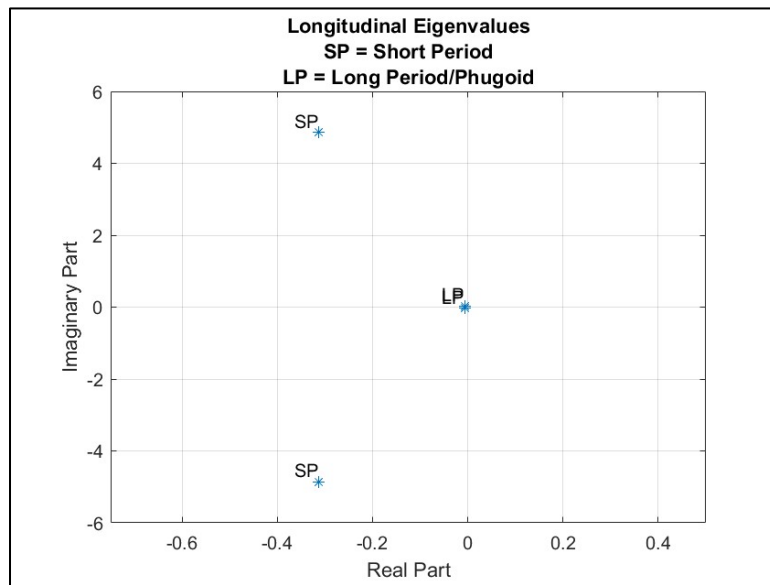


Figure 3-32: Longitudinal Eigenvalues

Lateral Linearized Model

Using the stability derivative found in Table 3-5, the resulting A and B matrices of the linearized lateral model are the following:

$$A_{LAT} = \begin{bmatrix} -0.0763 & 105.1486 & -1.739e+03 & 32.14 \\ -0.0048 & -0.7922 & 0.1422 & 0 \\ 0.0032 & -0.01247 & -0.1817 & 0 \\ 0 & 1 & 0.0605 & 0 \end{bmatrix}$$

$$B_{LAT} = \begin{bmatrix} -1.8966 & 9.4829 \\ 5.3362 & 0.982 \\ 0.0267 & -1.5751 \\ 0 & 0 \end{bmatrix}$$

All the lateral modes were found to be stable in finding the eigenvalues of the A matrix. The following are the resulting eigenvalues of the lateral model:

$$\lambda_{1,2} = -0.1371 \pm 2.4669i$$

$$\lambda_3 = -0.7744$$

$$\lambda_4 = -0.0018$$

Evidently, the first two eigenvalues correspond to the Dutch roll mode, while the third applied to the roll mode, and the fourth to the spiral mode. The corresponding Dutch roll mode frequency, Dutch roll mode damping ratio, roll time constant, and time to half amplitude are the following:

$$\omega_{DR} = 2.471 \left[\frac{\text{rad}}{\text{s}} \right], \zeta_{DR} = 0.055$$

$$\tau_R = 1.291 [\text{s}]$$

$$T_{1/2} = 388.43 [\text{s}]$$

The Dutch roll's frequency and damping ratio correspond to Level 2 flying qualities. The roll time constant and time to half amplitude correspond to Level 1 and Level 1 flying qualities for the roll mode and spiral mode, respectively. The following figure plots the lateral eigenvalues on real and imaginary axes. Due to their negative real part, which is apparent in the figure, both modes are stable.

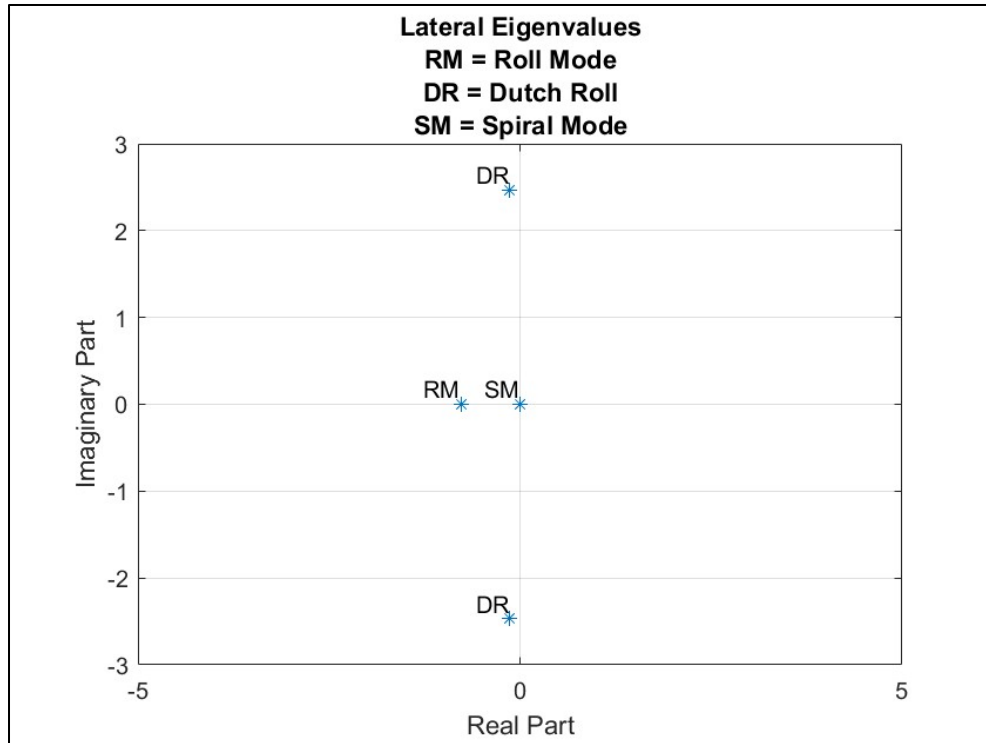


Figure 3-33: Lateral Eigenvalues

Linearized Simulations of Control Input Doublets

Elevator Doublet

First, the linear model was used to estimate the response from the elevator doublet. The following are the resulting plots for the 4 longitudinal states and 2 longitudinal controls.

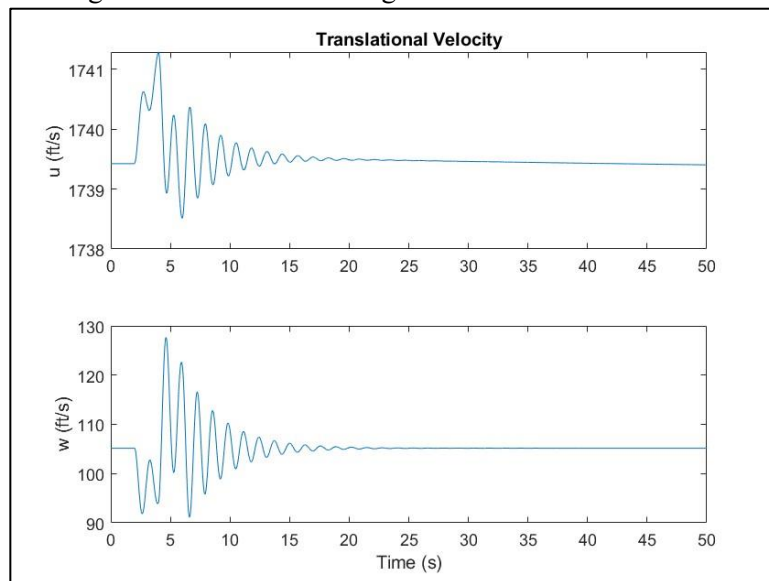


Figure 3-34: Elevator Doublet Body X and Z Velocities

As seen in Figure 3-34, the elevator doublet induced oscillations in the body X_B and Z_B velocities. The aircraft, as expected, returns to trim after some time due to the stability of the short period and long period modes.

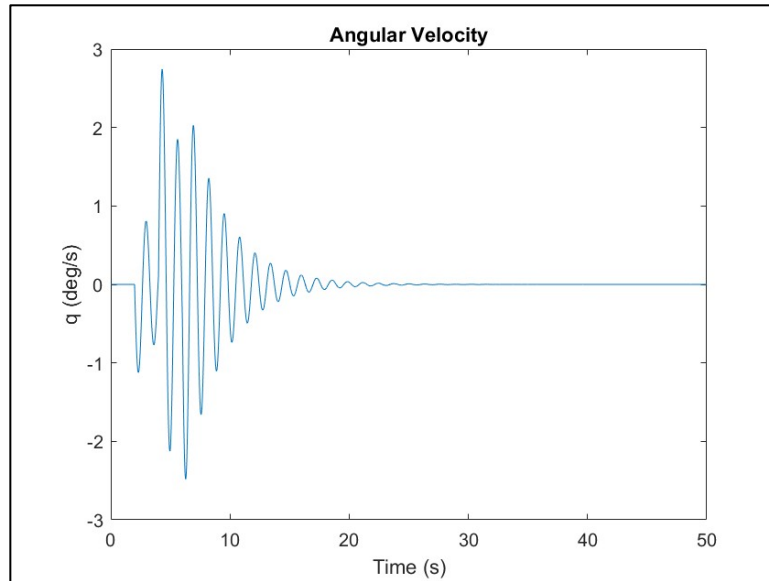


Figure 3-35: Elevator Doublet Pitch Rate

Oscillations in the pitch rate, as seen in Figure 3-35 were also induced by the elevator doublet and were damped out due to the aircraft's dynamic stability.

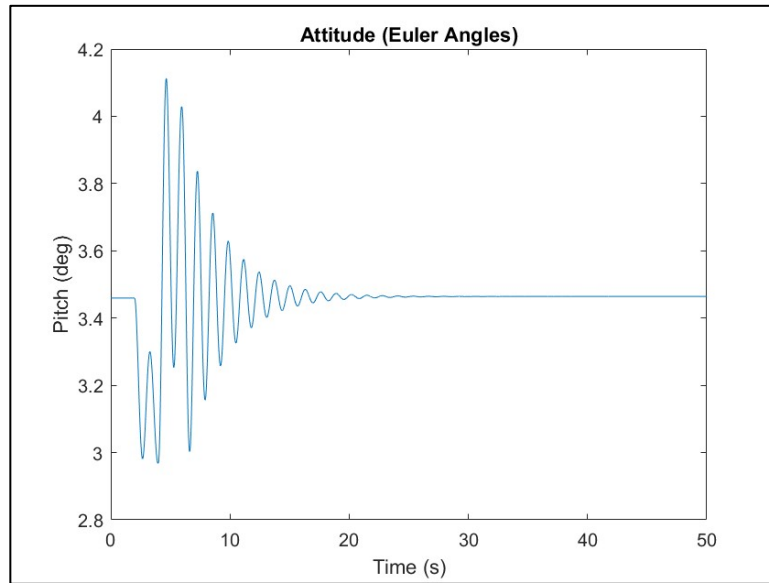


Figure 3-36: Elevator Doublet Pitch

As expected, the elevator doublet also induced oscillations in the pitch that were also damped out. The following figure plots the control inputs into the system. The 0.5° deflections are confirmed by Figure 3-37.

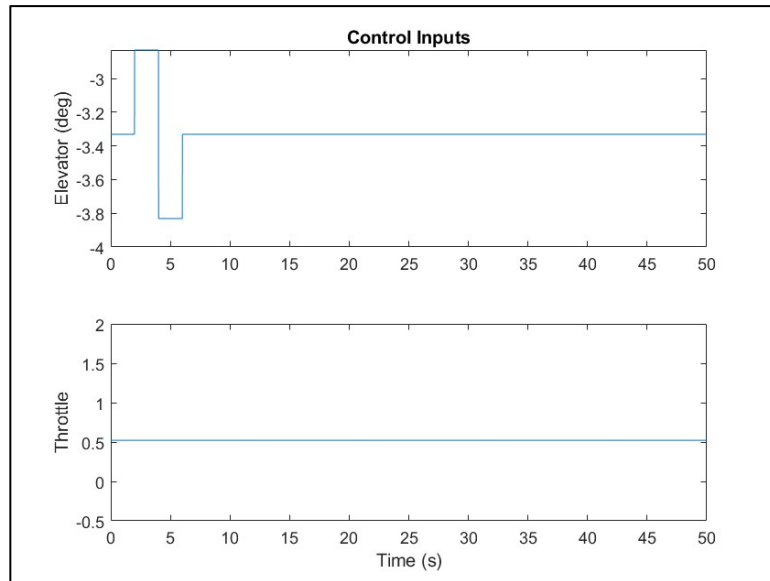


Figure 3-37: Elevator Doublet Control Inputs

To aide in comparison between the linearized longitudinal model and the full nonlinear model, the simulations were superimposed in the following plots. Yaw is not included in the linearized models, so there will be no estimate for it in the plots.

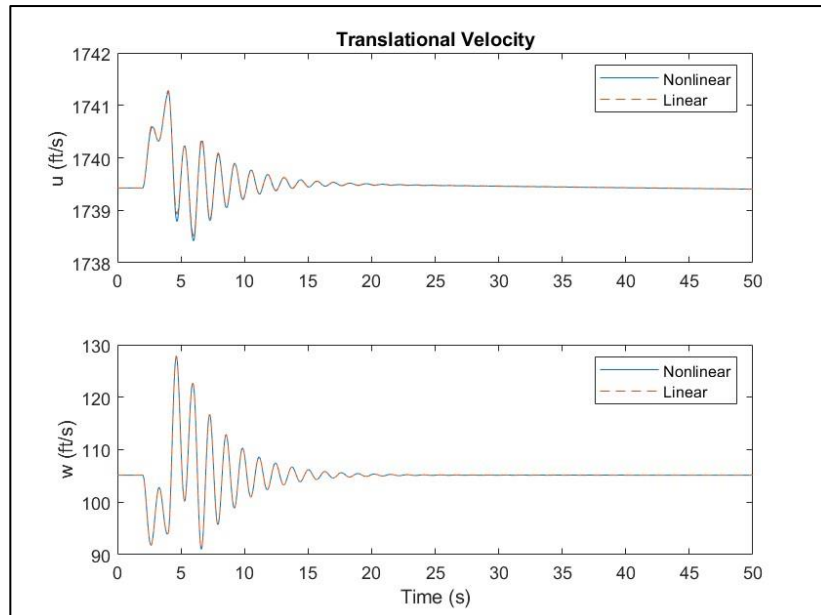


Figure 3-38: Elevator Doublet Linear and Nonlinear Translational Velocities

As seen in Figure 3-38, the nonlinear and linear simulations produced similar results to the elevator doublet. One interesting difference is that the phugoid mode is damped out slower in the nonlinear model than the linear model. In the context of application of these linearized models for some sort of control it is most important that the short period mode is accurately modeled as the pilot will have more time to input controls to stop the phugoid mode seen in the nonlinear model.

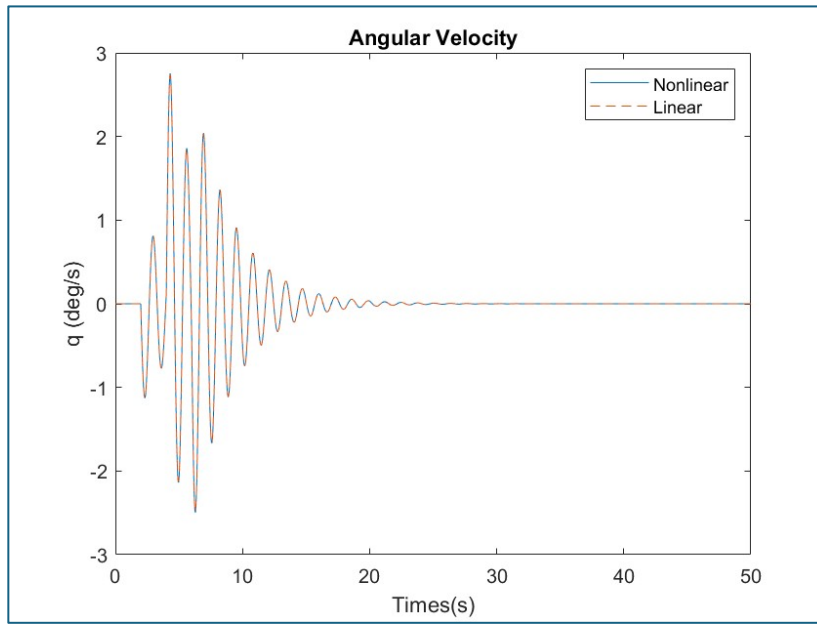


Figure 3-39: Elevator Doublet Linear and Nonlinear Angular Velocities

Again, as seen in Figure 3-39, the linear and nonlinear models see good agreement in their response to the elevator doublet. It is important to note that the lateral linearized model is not accounted for because there will not be any significant lateral responses to elevator deflection. The same agreement can be found in Figure 3-40.

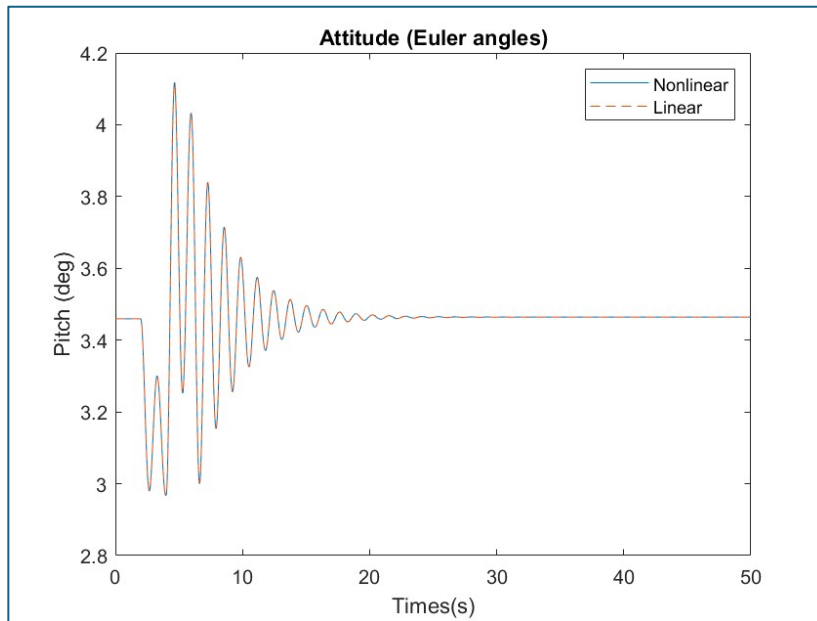


Figure 3-40: Elevator Doublet Linear and Nonlinear Attitude Responses

To ensure that the same control inputs were seen by both simulations, the control inputs were plotted.

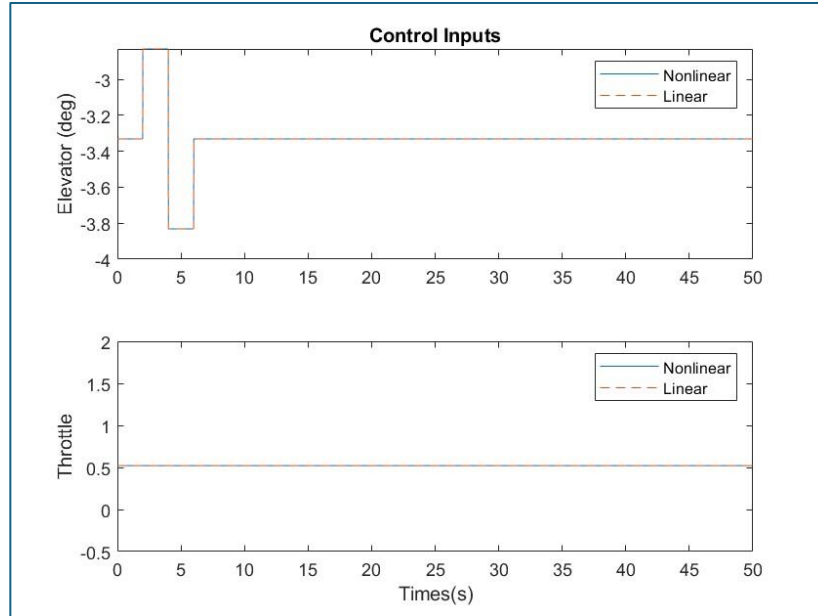


Figure 3-41: Elevator Doublet Linear and Nonlinear Control Inputs

Thrust Doublet

The linearized longitudinal model was also used to predict the response to a thrust doublet. The following are the resulting plots for the 4 longitudinal states and 2 longitudinal controls.

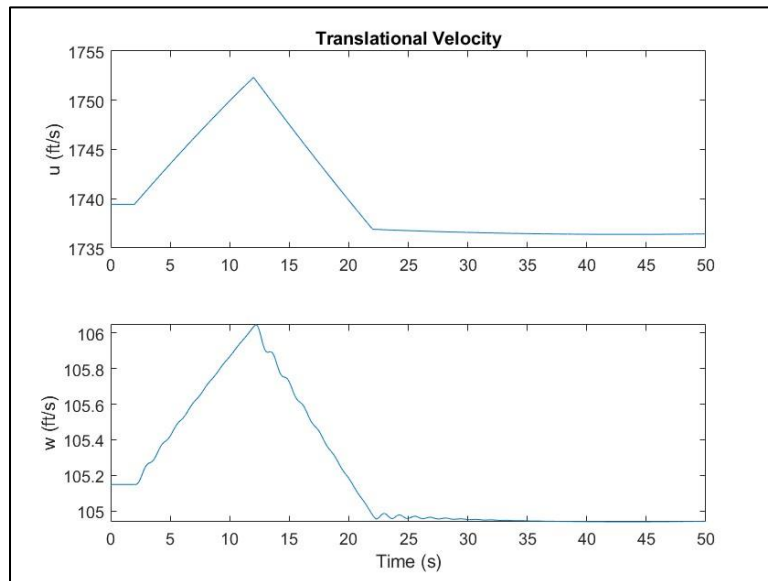


Figure 3-42: Thrust Doublet Linear Translational Velocities

As shown in Figure 3-42, only very small variations in the body X and Z velocities were produced.

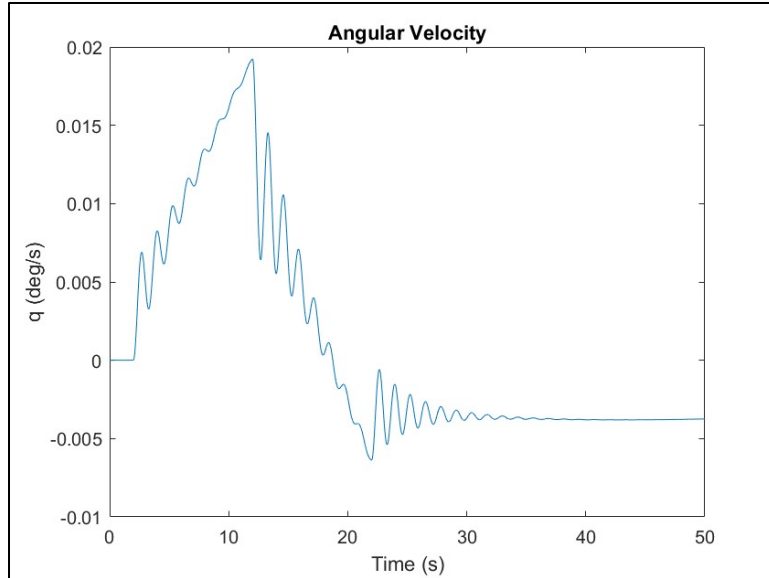


Figure 3-43: Thrust Doublet Linear Angular Velocity

The thrust doublet did induce oscillations in the pitch rate.

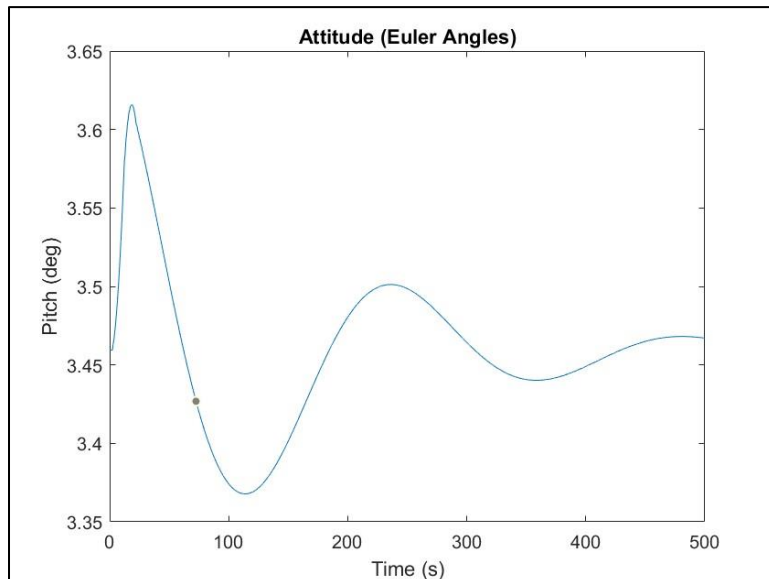


Figure 3-44: Thrust Doublet Linear Attitude Responses

Finally, the control inputs for the thrust doublet were plotted.

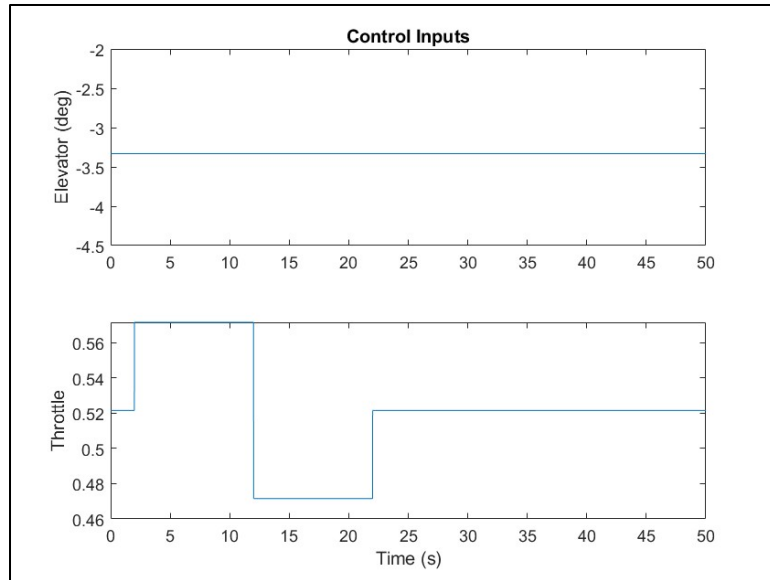


Figure 3-45: Thrust Doublet Control Inputs

As in the case for the elevator doublet, the thrust doublet responses for the nonlinear and linear cases were superimposed in the following plots.

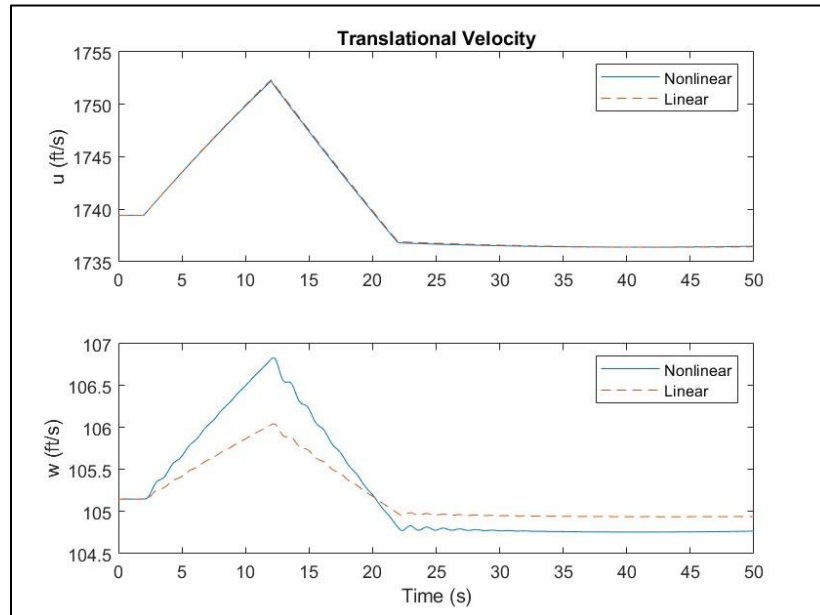


Figure 3-46: Thrust Doublet Nonlinear and Linear Translational Velocities

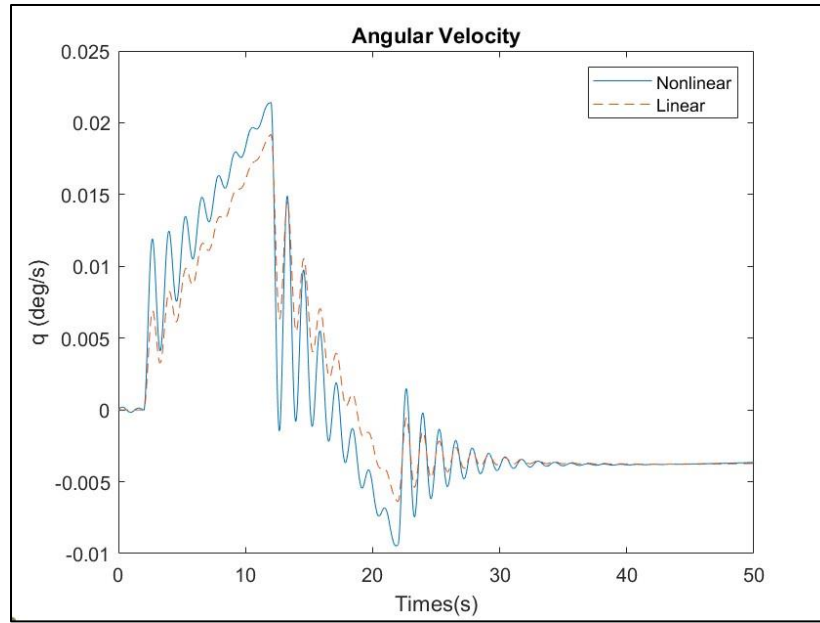


Figure 3-47: Thrust Doublet Nonlinear and Linear Angular Velocities

From Figures 3-46 and 3-47, it is evident that the linearized longitudinal model does not do well to simulate the phugoid mode induced by the thrust doublet. This is similar to the elevator doublet case. Again, it is important to note these are small amplitude oscillations with low frequencies, allowing the pilot plenty of time to input control.

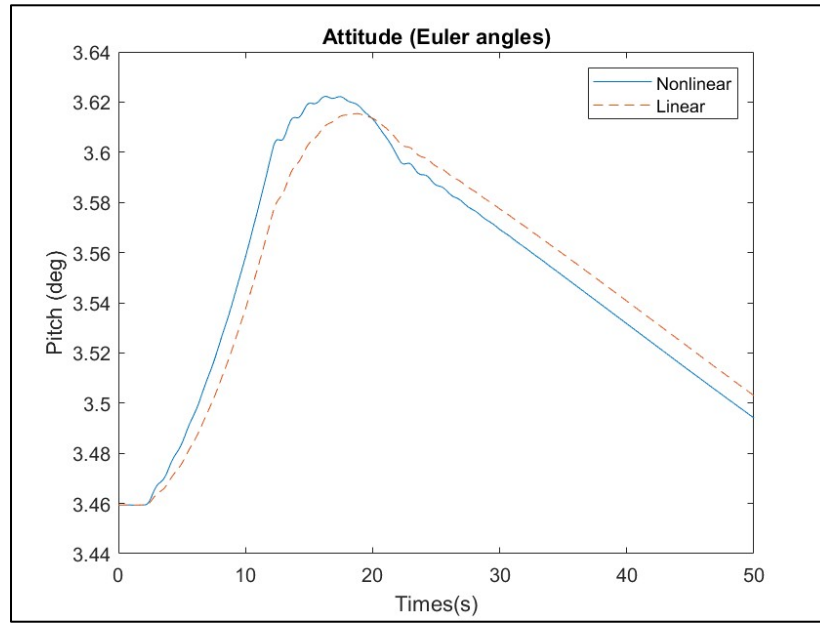


Figure 3-48: Thrust Doublet Nonlinear and Linear Angular Velocities Attitude Response

Finally, the control inputs were plotted.

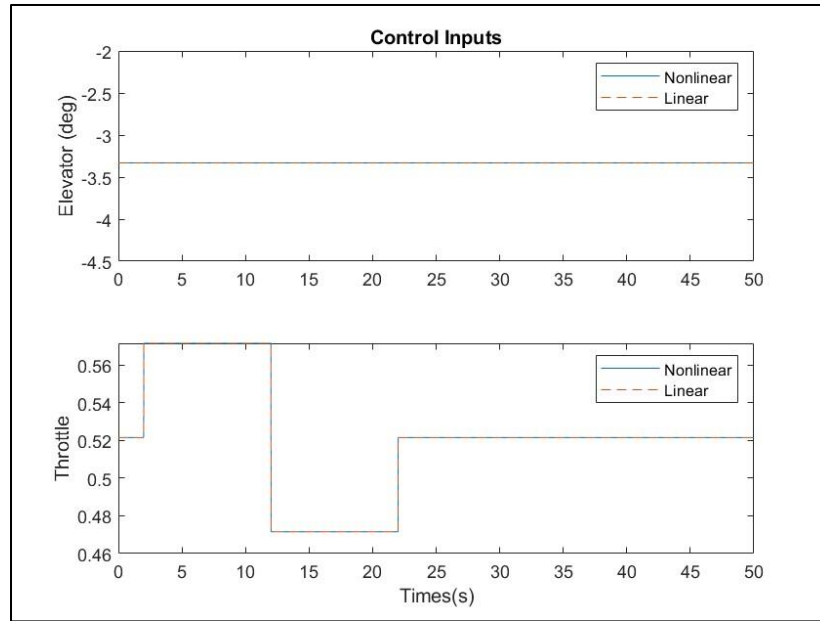


Figure 3-49: Thrust Doublet Control Inputs

Evidently, the inputs were the same for the nonlinear and linear simulations.

Aileron Doublet

The following plots show the linearized lateral model responses to an aileron doublet.

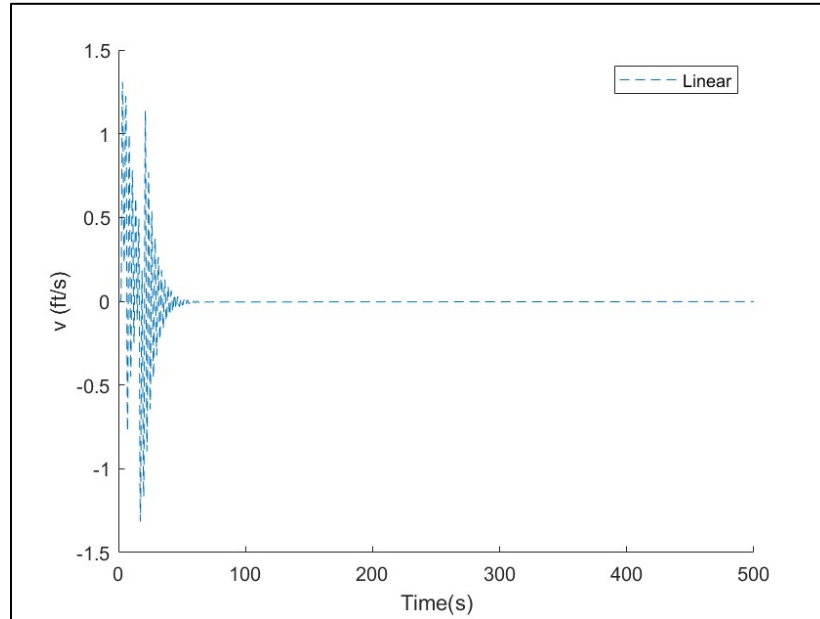


Figure 3-50: Aileron Doublet Linear Translational Velocity

The aileron doublet, inducing Dutch roll dynamics, causes oscillations in the body Y-velocity.

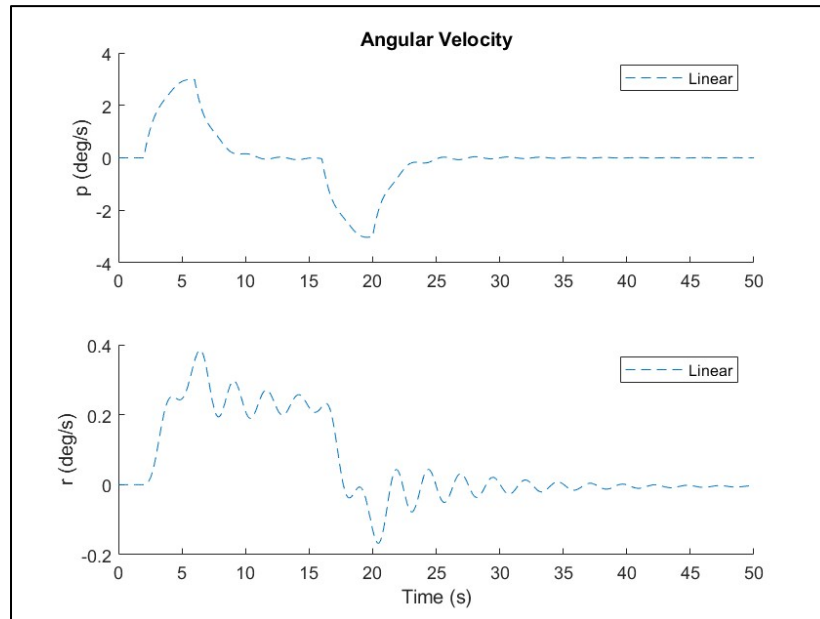


Figure 3-51: Aileron Doublet Linear Angular Velocities

Oscillations are also apparent in the roll and yaw rate.

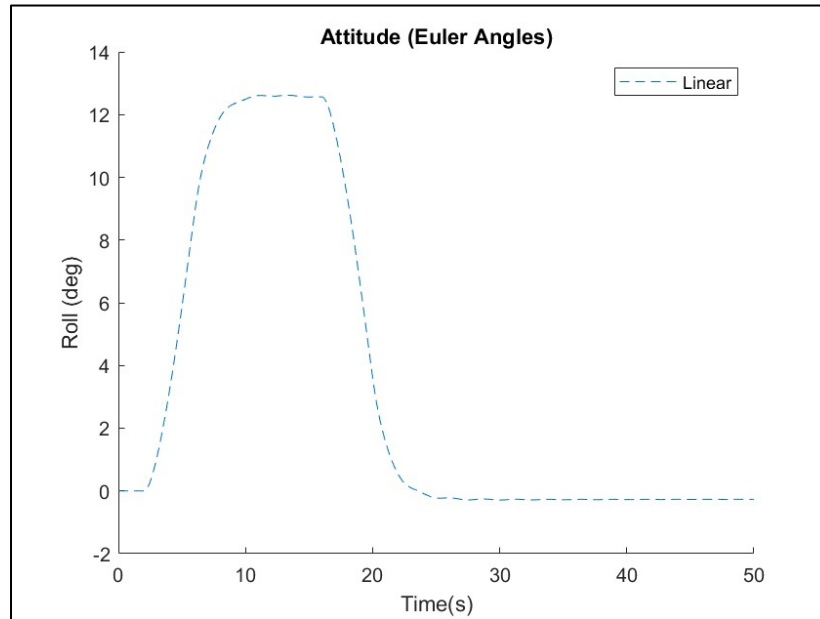


Figure 3-52: Aileron Doublet Linear Attitude Responses

Again, to verify the control inputs, they were plotted.

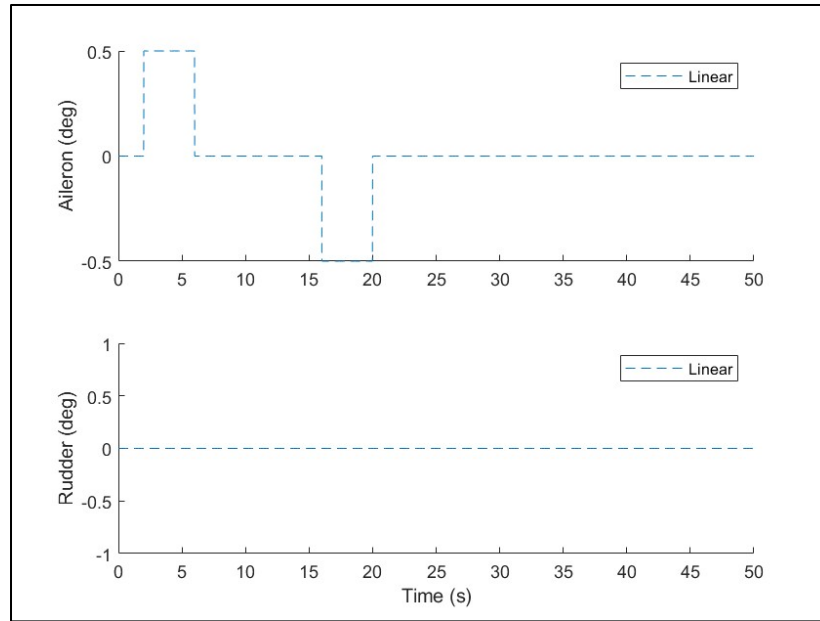


Figure 3-53: Aileron Doublet Control Inputs

As was done for the elevator and thrust doublets, the nonlinear and linear dynamics were superimposed.

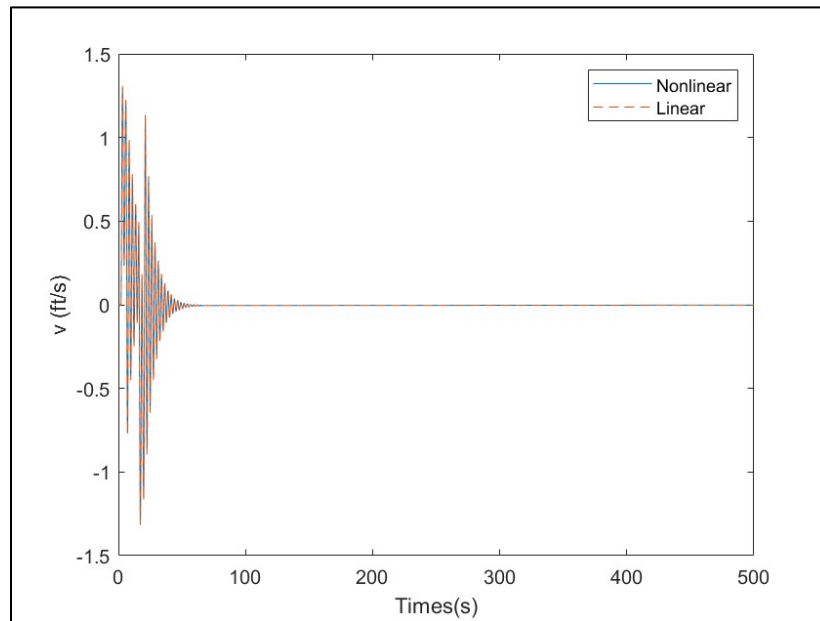


Figure 3-54: Aileron Doublet Nonlinear and Linear Translational Velocities

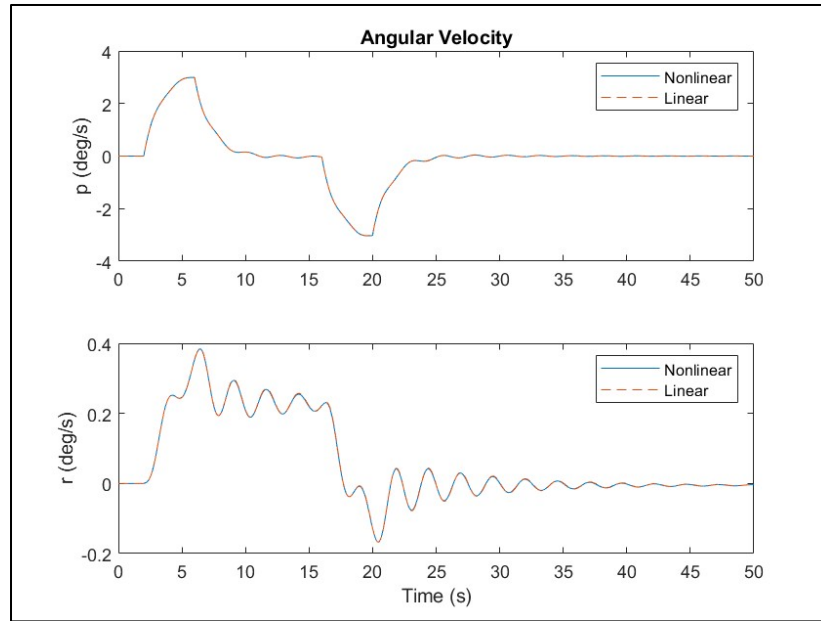


Figure 3-55: Aileron Doublet Nonlinear and Linear Angular Velocities

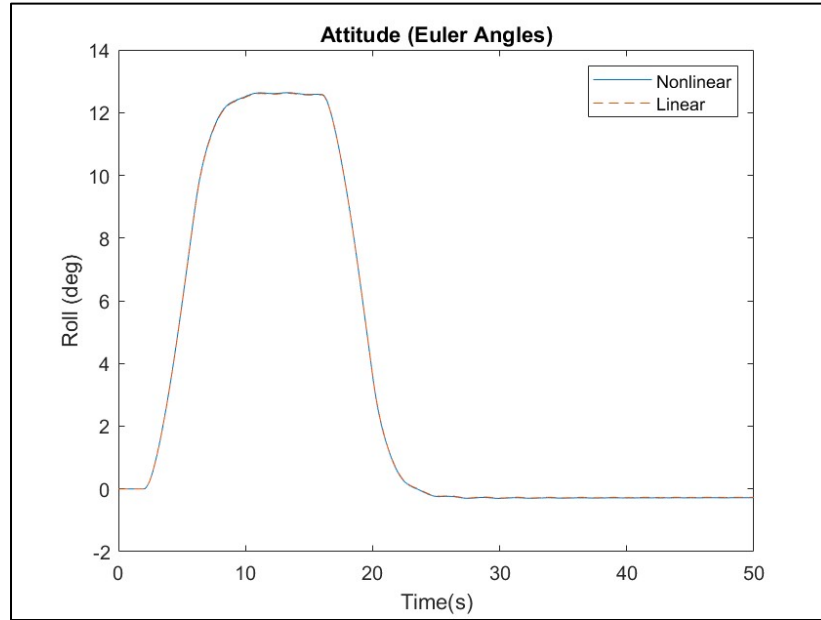


Figure 3-56: Aileron Doublet Nonlinear and Linear Attitude Responses

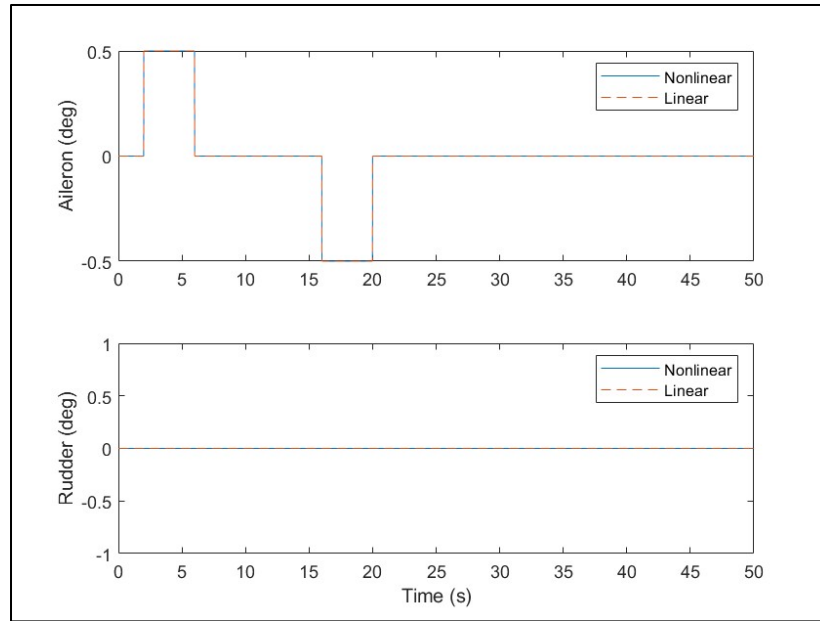


Figure 3-57: Aileron Doublet Nonlinear and Linear Control Inputs

The simulation response comparisons found in Figures 23, 24, and 25 point to an interesting shortcoming in the linearized lateral model. Dutch roll causes oscillations not only in the lateral state variables, but also in the longitudinal state variables. Thus, since the linearized lateral model does not consider the longitudinal responses, they are completely left out by the simulation. For those that it did simulate, however, there was good agreement between the linear and nonlinear models.

Rudder Doublet

The following plots show the linearized lateral model responses to a rudder doublet.

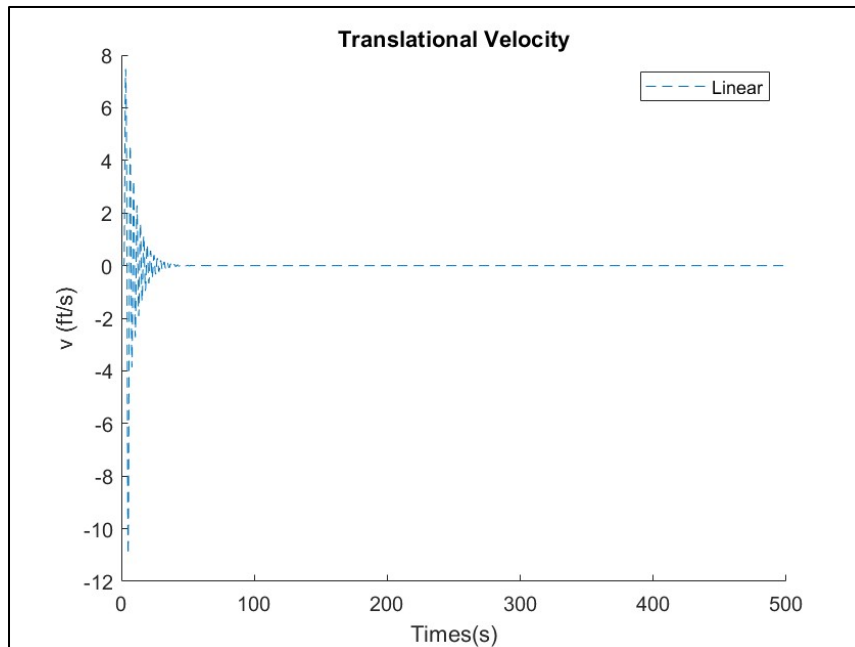


Figure 3-58: Rudder Doublet lateral translational velocity

The rudder doublet causes oscillations in the body Y-velocity, as shown in Figure 3-58.

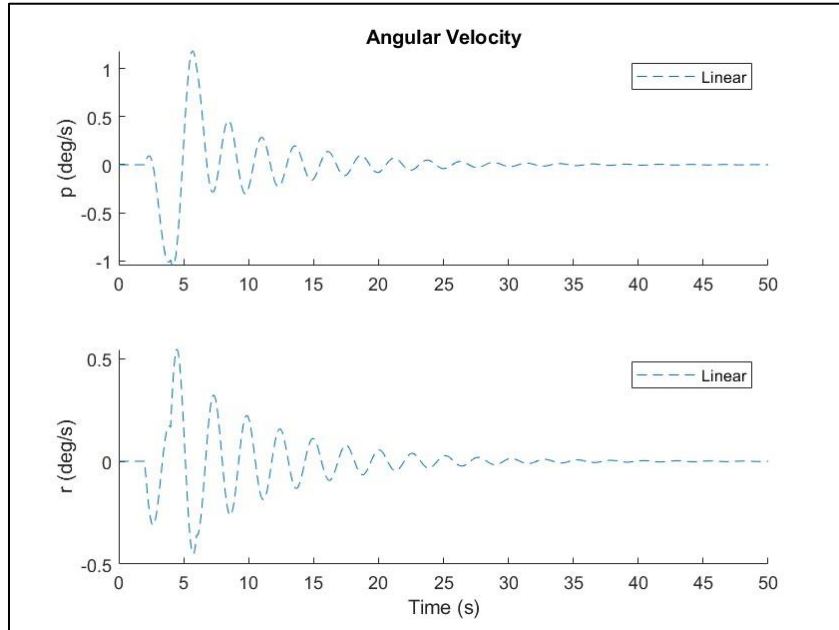


Figure 3-59: Rudder Doublet Lateral Angular Velocity

There are also oscillations that can be seen in the roll and yaw rate as shown in Figure 3-59.

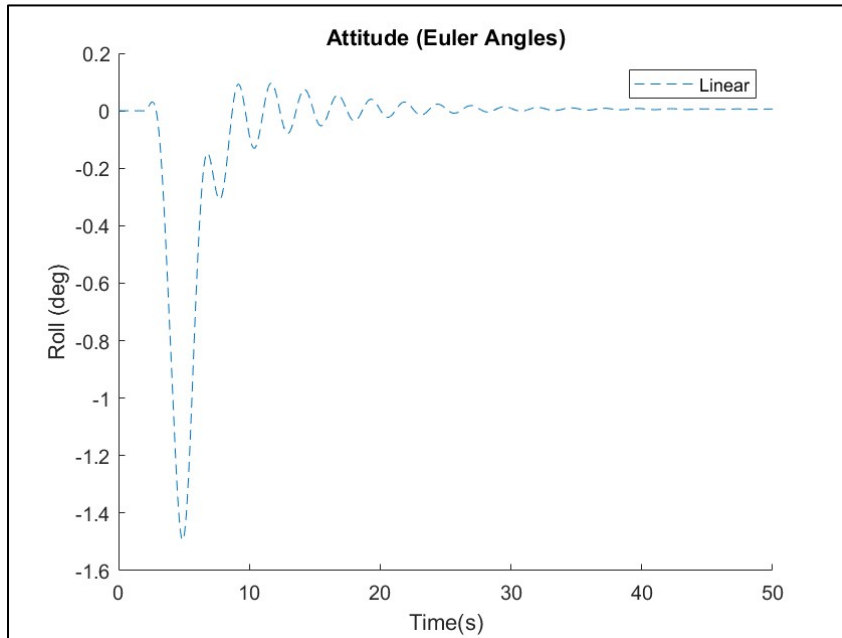


Figure 3-60: Rudder Doublet Lateral Attitude Response

The rudder doublet causes visible oscillations in the roll angle which finally stabilizes as shown in Figure 3-60.

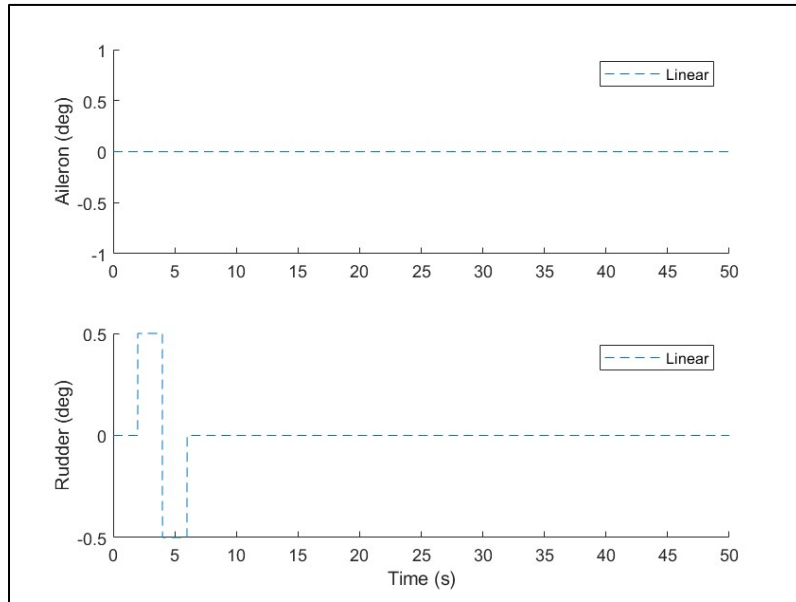


Figure 3-61: Rudder Doublet Control Inputs

The control inputs were then plotted as shown in Figure 3-61.

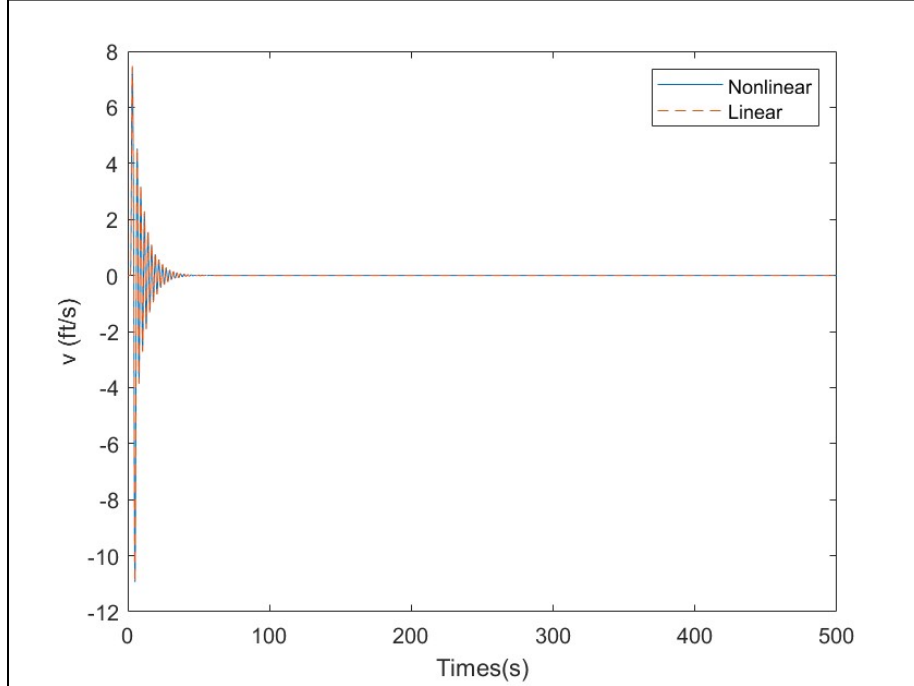


Figure 3-62: Rudder Doublet Nonlinear and Linear translational velocities

The next few graphs are the product of superimposing the nonlinear and linear dynamics.

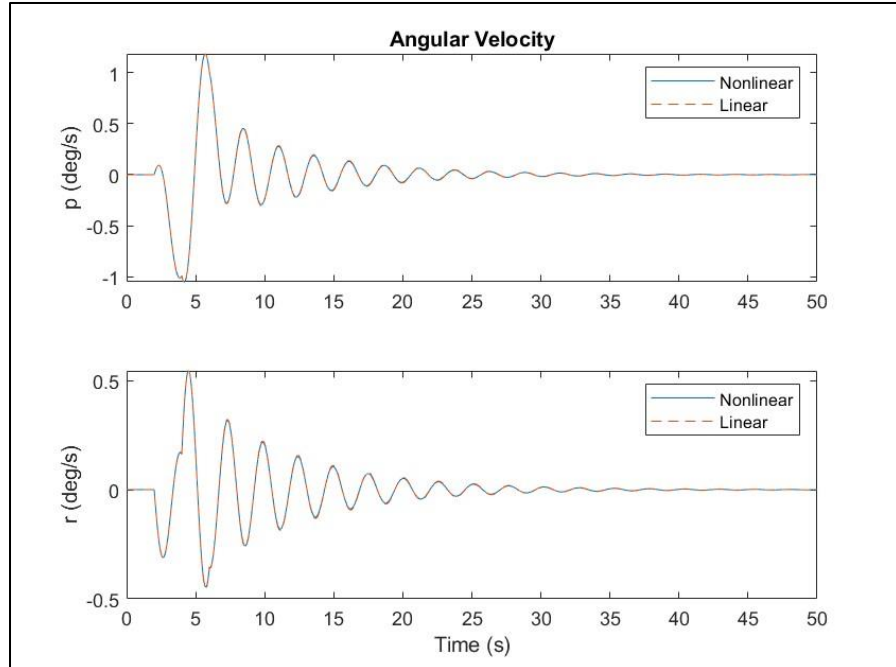


Figure 3-63: Rudder Doublet Nonlinear and Linear angular velocities

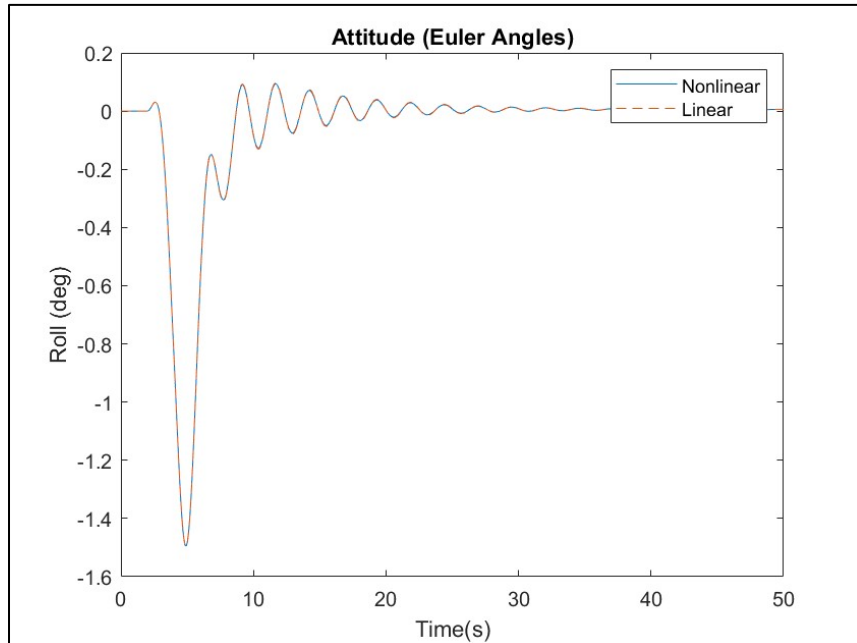


Figure 3-64: Rudder Doublet Nonlinear and Linear Attitude Responses

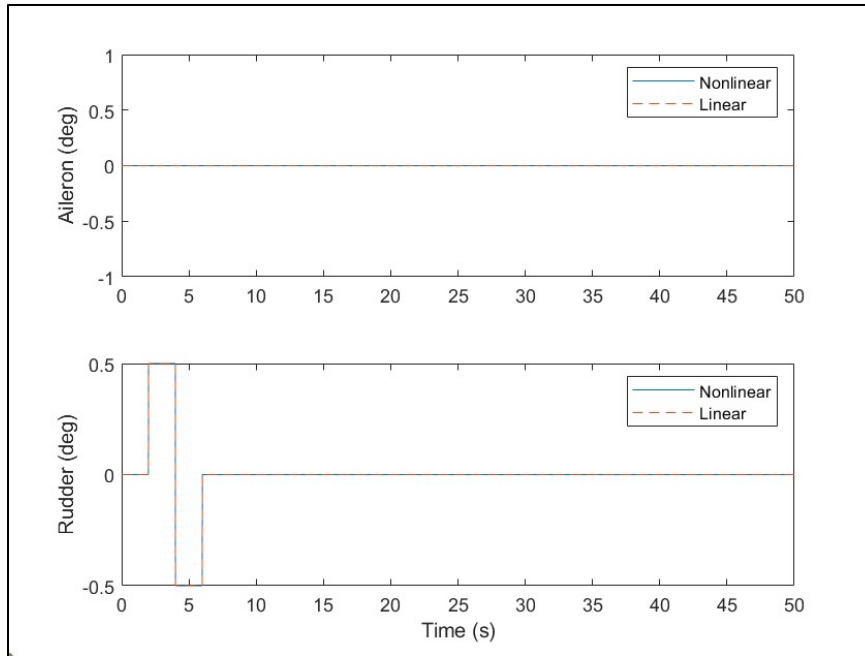


Figure 3-65: Rudder Doublet Control Inputs

In Figures 3-62, 3-63, 3-64, and 3-65, we can see that the thrust doublet only causes oscillations in the lateral state variables for the linear model, but the nonlinear model shows the effects on the longitudinal state variables as well. For the lateral state variables, the linear and nonlinear models agree well.

Stability Augmentation System

Open-Loop and Closed-Loop Comparison

After first investigating the open-loop linear longitudinal and lateral models, the team set out to create a stability augmentation system. This system is a feedback control system. To create this system, goals for its performance were set.

Table 4-1: Open-Loop Flying Qualities

Mode:	Flying Quality Level
Phugoid	1
Short Period	3
Dutch Roll	2
Roll	1
Spiral	1

As directed, control goals were determined based on the flying qualities of the open-loop system. The phugoid mode, since it was already Level 1, was only slightly improved by increasing the damping ratio by 10%. The short period mode, since it was Level 3, was improved to Level 1 conditions by bringing the damping ratio to an increased value and keeping the frequency constant. Like the short period mode, the Dutch roll needed to be improved to Level 1 conditions. To complete this, the damping ratio was

increased, and the frequency was held constant. For the roll mode, since it was already Level 1, no changes were made. The spiral mode, on the other hand, was improved to have a shorter time to half amplitude. The following table contains the desired mode parameters.

Table 4-2: Desired Closed-Loop Mode Values

Mode:	Open-Loop Value	Closed-Loop Desired Value
Phugoid	$\zeta_{LP} = 0.241$	$\zeta_{LP} = 0.2656$
Short Period	$\zeta_{SP} = 0.064$	$\zeta_{SP} = 0.3500$
Dutch Roll	$\zeta_{DR} = 0.055$	$\zeta_{DR} = 0.0900$
Roll	$\tau_R = 1.2914 \text{ [s]}$	$\tau_R = 1.2914 \text{ [s]}$
Spiral	$T_{1/2} = 388.430 \text{ [s]}$	$T_{1/2} = 10 \text{ [s]}$

To achieve these goals, the desired damping ratios and frequencies were used to calculate the desired eigenvalues.

Resulting Longitudinal and Lateral Stability Augmentation Systems

Then, using the Bass-Gura method, the gain matrices for both the longitudinal and lateral models were found. The rudder and aileron were weight based on their maximum deflection. The following are the calculated gain matrices:

$$K_{LONG} = \begin{bmatrix} 1.9778e-06 & 4.1770e-05 & -0.2429 & -0.0106 \\ 0 & 0 & 0 & 0 \end{bmatrix}$$

$$K_{LAT} = \begin{bmatrix} -2.6456e-07 & 0.0230 & -0.0482 & 0.0164 \\ -3.1747e-07 & 0.0276 & -0.0579 & 0.0197 \end{bmatrix}$$

Using these gain matrices, the respective mode dynamics could be found for the closed-loop system. This was done by finding the eigenvalues of $[A-BK]$ and calculating the corresponding parameters.

Table 4-3: Oscillatory Modes

Mode	ξ (open)	ξ (closed)	ω_n (open) [rad/s]	ω_n (closed) [rad/s]
Phugoid	0.2415	0.2656	0.0265	0.0265
Short Period	0.0642	0.3500	4.8695	4.8695
Dutch Roll	0.0555	0.0900	2.4707	2.4707

Table 3-4: Non-Oscillatory Modes

Mode	$T_{1/2}$ (open) [s]	$T_{1/2}$ (closed) [s]	τ_R (open) [s]	τ_R (closed) [s]
Spiral	388.43	10.000	-	-
Roll	-	-	1.2914	1.2914

After analyzing the closed-loop system it is apparent that the gain matrices are correct because they return the same mode values as the desired ones. The benefits of the new mode dynamics will become apparent in the following simulations.

Linear Open-Loop and Closed-Loop Simulations

Yaw Rate Disturbance

First, the lateral case was determined by setting the IC to:

$$\{\Delta v \ \Delta p \ \Delta r \ \Delta \Phi\}^T = \{0 \ 0 \ 2\text{deg/s} \ 0\}^T$$

These initial conditions result in the following figures.

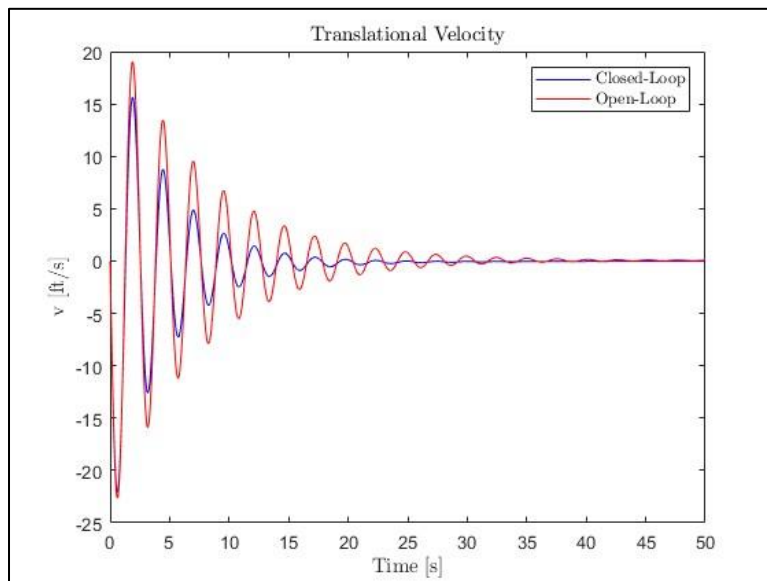


Figure 4-1: Linear Yaw Rate Disturbance Translational Velocities

Figure 4-1 demonstrates how the closed-loop system achieves a more dynamically stable lateral response, and a more desirable transient response than the open-loop system. The closed-loop configuration exhibits a lower settling time, meaning it dampens oscillations quickly to reach a steady state velocity ($v = 0$ [ft/s]). Additionally, the closed-loop response not only settles faster, but also has a lower amplitude of oscillations, indicating less pronounced deviations from the trim lateral velocity.

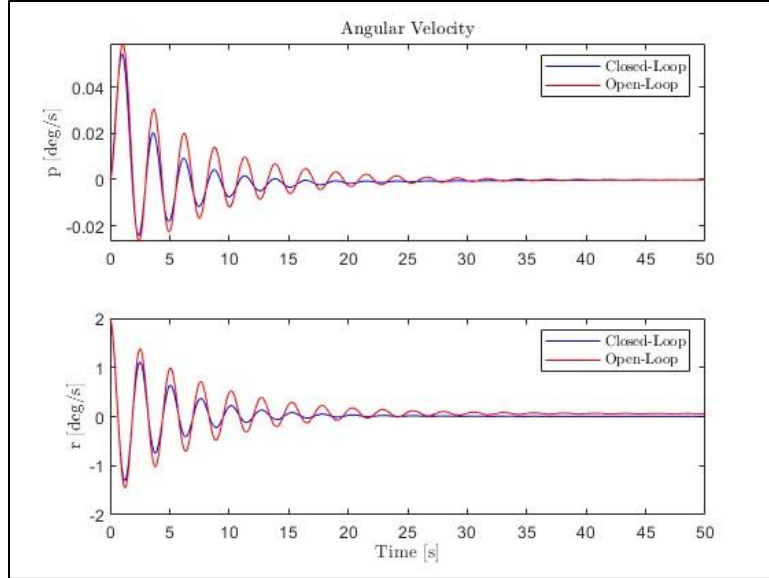


Figure 4-2: Linear Yaw Rate Disturbance Angular Velocities

Figure 4-2 shows that while both configurations experience similar oscillation amplitudes, the closed-loop system achieves stabilization significantly faster. This implies that the control system effectively reduces unwanted rolling (p) and yawing (r) motions as a result of the Dutch roll mode, allowing the aircraft to reach a steady state quicker compared to the uncontrolled (open-loop) scenario.

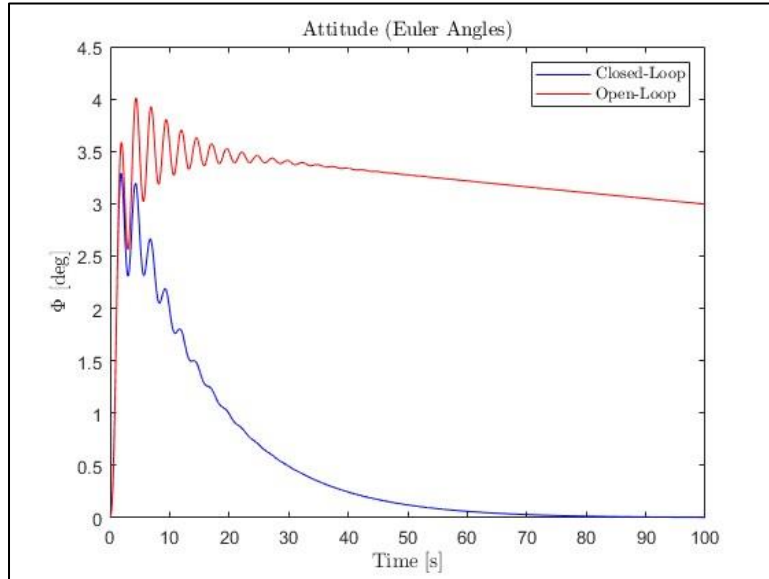


Figure 4-3: Linear Yaw Rate Disturbance Attitude

The closed-loop system's advantage extends to the aircraft's attitude, for the lateral case. Although both open-loop and closed-loop configurations exhibit oscillations in the roll angle due to Dutch roll, Figure 4-3 demonstrates a clear difference. The closed-loop system's attitude oscillations settle to zero much faster than the open-loop system's oscillations, and trends towards zero roll angle much faster. The changes made to the Dutch roll dampen out the oscillations, and the decrease of time to half-amplitude in the roll mode quickly returns the aircraft to wings level. Overall, this behavior reinforces the effectiveness of the feedback control system.

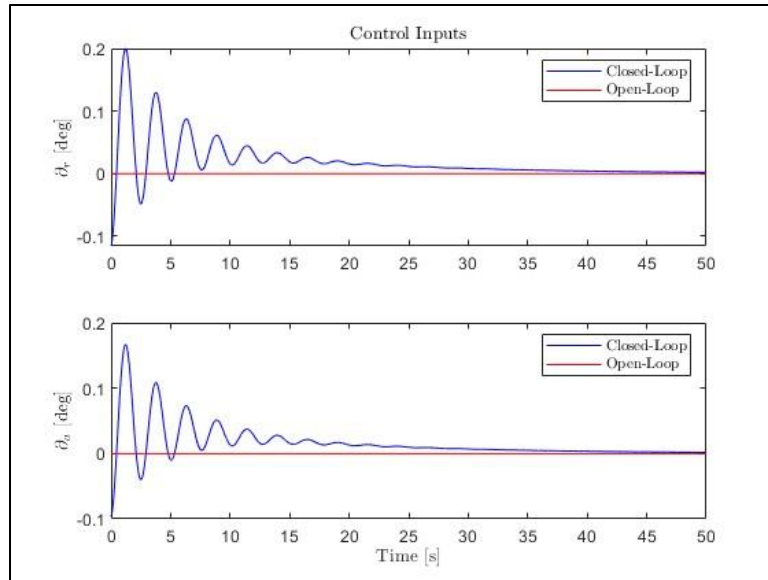


Figure 4-4: Linear Yaw Rate Disturbance Control Inputs

The control surface deflections in the lateral maneuver further highlights the role of the closed-loop system. Unlike the open-loop scenario, where both the aileron and rudder remain at zero deflection throughout due to no pilot input, the closed-loop system exhibits controlled oscillations in both control surfaces. This is shown in Figure 4-4. These oscillations suggest the control system actively adjusts the aileron and rudder to counter any deviations. This achieves the desired lateral movement. Importantly, these oscillations eventually dampen out, indicating the control system's success in stabilizing the aircraft, and returning to trim conditions.

Pitch Rate Disturbance

Now, for the longitudinal case, setting the initial conditions to the following:

$$\{\Delta u \ \Delta w \ \Delta q \ \Delta \Theta\}^T = \{0 \ 0 \ 2\text{deg/s} \ 0\}^T$$

The following plots were obtained from the above equation.

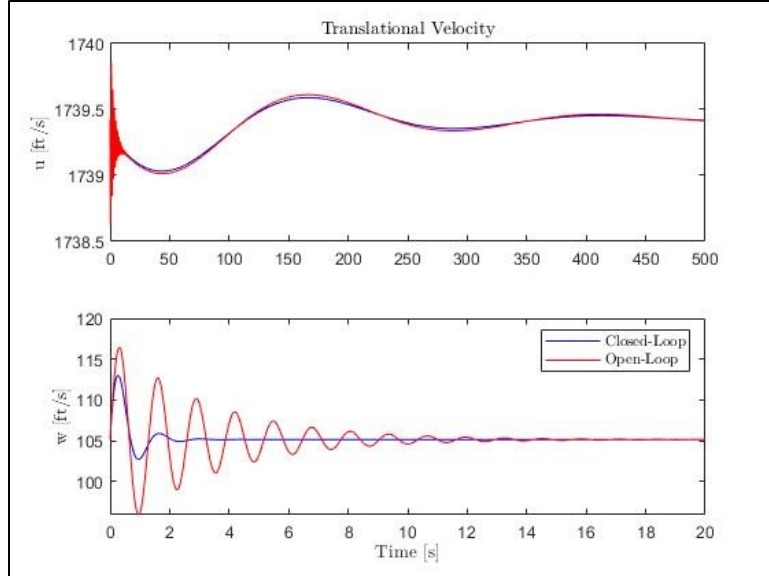


Figure 4-5: Linear Pitch Rate Disturbance Translational Velocities

As seen in Figure 4-5, the aircraft simulation exhibited similar translational velocity responses in the X-body frame direction (u) between the open-loop and closed-loop scenarios when started with an initial pitch rate. The small difference seen is due to the 10% increase in damping ratio for the long period mode. Conversely, the translational velocity in Z-body frame direction (w) showed more discrepancies between the open-loop and closed-loop cases because the short period mode was significantly affected by the control system to change the flying qualities from Level 3 to Level 1, and the short period mode affects w more than u traditionally. The open-loop results for w had a slightly higher amplitude than the closed-loop results, and a longer settling time as opposed to the closed-loop results. This points to increased damping and better flying qualities in the closed-loop system, as expected.

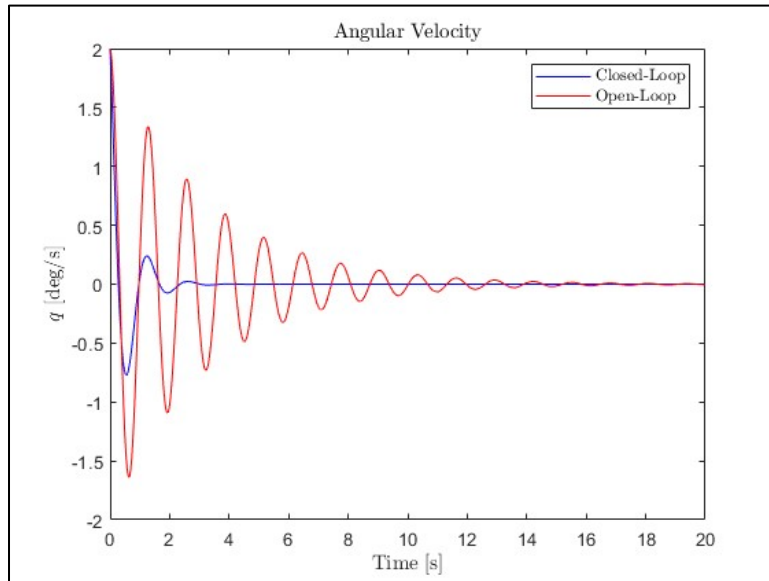


Figure 4-6: Linear Pitch Rate Disturbance Angular Velocities

As shown in Figure 4-6, the closed-loop system stabilizes faster than the open-loop system. The oscillations in q are mainly due to the short period mode, thus the increased damping improves the short

period mode flying qualities. This essentially means that the control chosen in the closed-loop system is working.

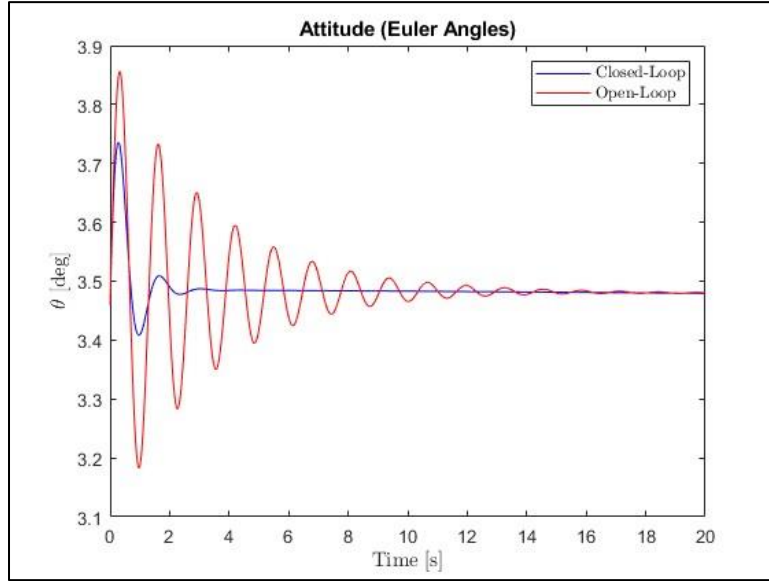


Figure 4-7: Linear Pitch Rate Disturbance Attitude

Similarly, Figure 4-7 shows the pitch against time in both the closed and open-loop systems, with the open-loop system having a higher amplitude and a longer time to dampen and stabilize, further showing the effectiveness of the closed-loop system, especially in damping out the short period mode.

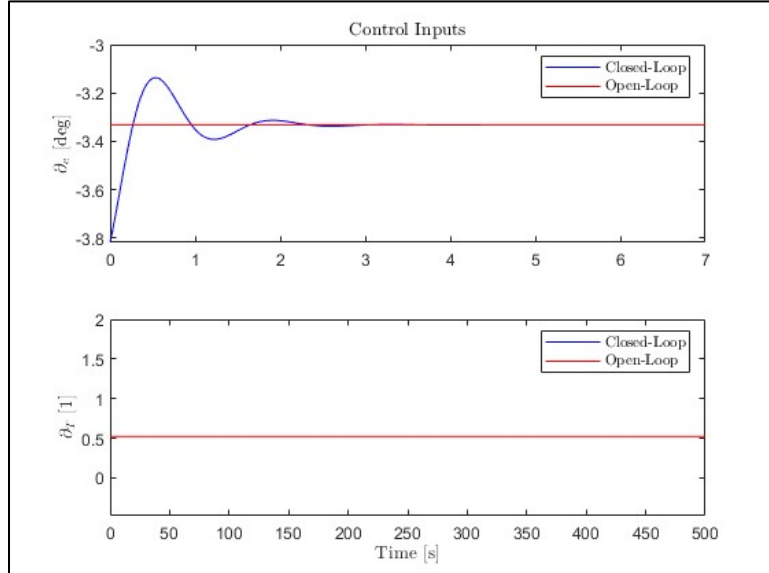


Figure 4-8: Linear Pitch Rate Disturbance Control Inputs

Figure 4-8 shows that in the longitudinal case, the control inputs differed significantly between the closed-loop and open-loop systems. For the open-loop scenario, the elevator is kept at a trim deflection of -3.3 degrees, and the thrust is kept at trim condition. In the closed-loop system, the elevator varies from trim to damp out oscillations, while the thrust stays constant, as it was set to using the g matrix.

Nonlinear Open-Loop and Closed-Loop Simulations

The stability augmentation systems for the longitudinal and lateral models were implemented into the nonlinear simulation, creating a closed-loop feedback control system. Using the new closed-loop model and the previous open-loop model, the results could be compared and the effectiveness of the linear approximations for control can be investigated. Three different simulations were run, with different initial conditions a constant pilot inputs of trim conditions.

Pitch Rate Disturbance

First, the pitch rate was given an initial condition of 2 [deg/s]. This initial condition is expected to excite the short period and long period modes. The following plots compare the results of the closed-loop and open-loop systems to this initial condition.

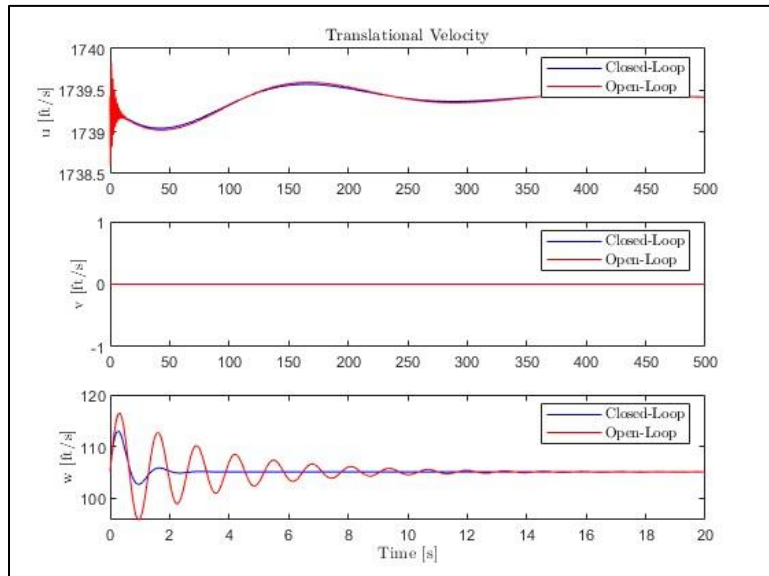


Figure 4-9: Nonlinear Pitch Rate Disturbance Translational Velocities

The first plot shows the translational velocity responses for the open and closed-loop systems. They are very similar to what was seen for the linear longitudinal model, which suggests that over small disturbances from trim, the linear model is a reasonable assumption, even at supersonic conditions. Again, the long period mode dynamics are slightly improved by the slight increase in the desired damping ratio, as seen in the slightly different oscillations in u . Additionally, there is a large improvement in the short period dynamics, due to the large increase in the desired damping ratio from the feedback control system.

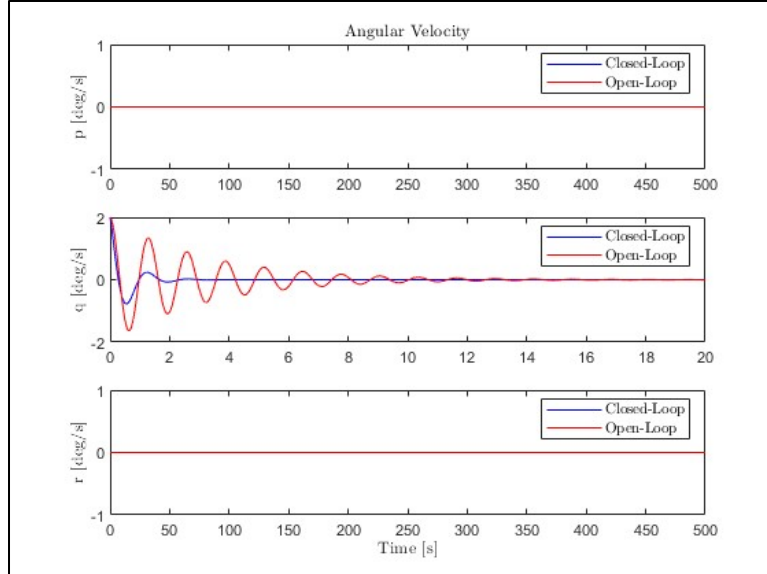


Figure 4-10: Nonlinear Pitch Rate Disturbance Angular Velocities

The initial disturbance is made apparent by plotting the pitch rates against time, where the pitch rate has an initial value of 2 [deg/s]. It is also apparent, however, that due to improved short period dynamics, the oscillations induced by the disturbance are quickly damped out, at a much shorter settling time than the open-loop system with no feedback control.

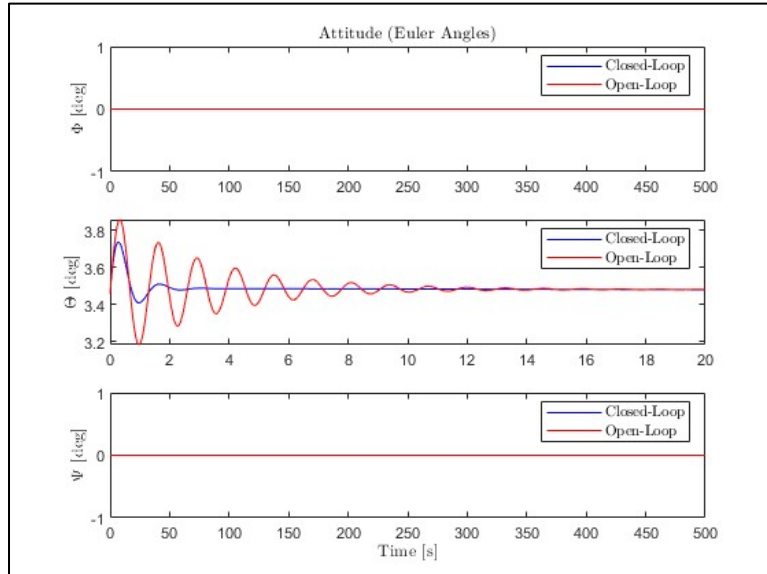


Figure 4-11: Nonlinear Pitch Rate Disturbance Attitude

Again, the attitude plotted against time is very similar to the linear longitudinal model that was simulated with similar initial conditions. As expected, there are no changes in the lateral attitude values as the initial conditions induce a purely longitudinal response from the model. This is true for both the open and closed-loop models. Additionally, the short period mode is again shown to be damped adequately through the settling time seen in the plot of the pitch.

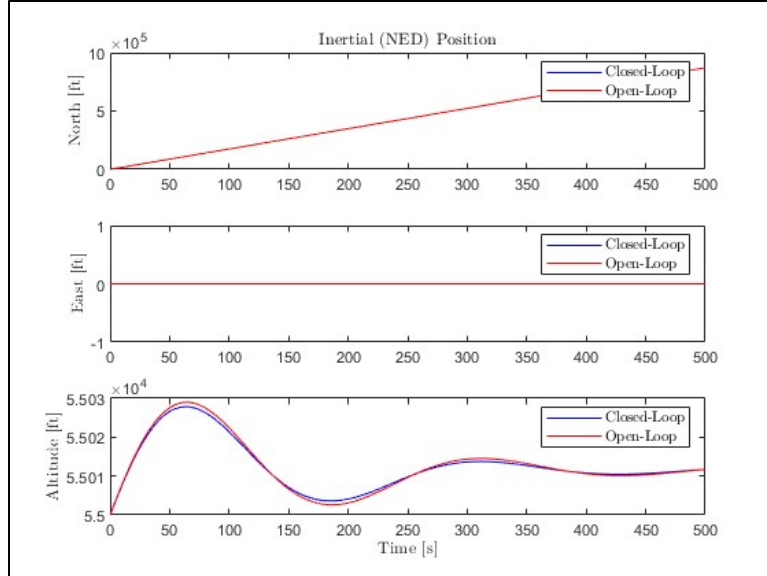


Figure 4-12: Nonlinear Pitch Rate Disturbance Inertial Position

As expected, the north and east flight positions are not affected by only a longitudinal response. A response in the altitude is apparent, however, because of the long period mode. The oscillations, as shown, are over a very long period, allowing the pilot ample time to add control inputs. The closed-loop system also shows to have slightly smaller amplitude, showing a slight increase in the long period damping ratio.

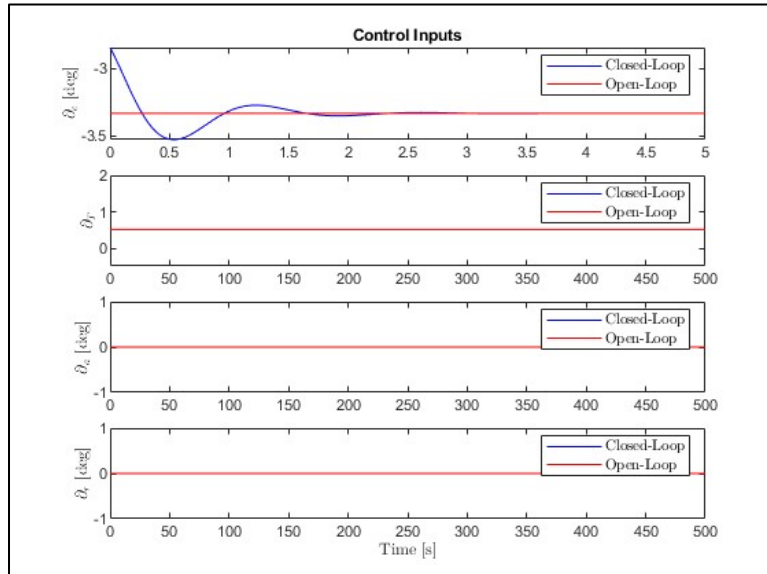


Figure 4-13: Nonlinear Pitch Rate Disturbance Control Inputs

The control inputs show the difference between open-loop and closed-loop systems. Although the “pilot inputs” (the control history) are set to the same, constant value in both simulations, the closed-loop system adds inputs based on the state of the system. In this case, the closed-loop system only reacts with

elevator inputs, as the throttle is not used for longitudinal control, and there were no variances in the lateral state variables that would induce control inputs from the aileron and rudder.

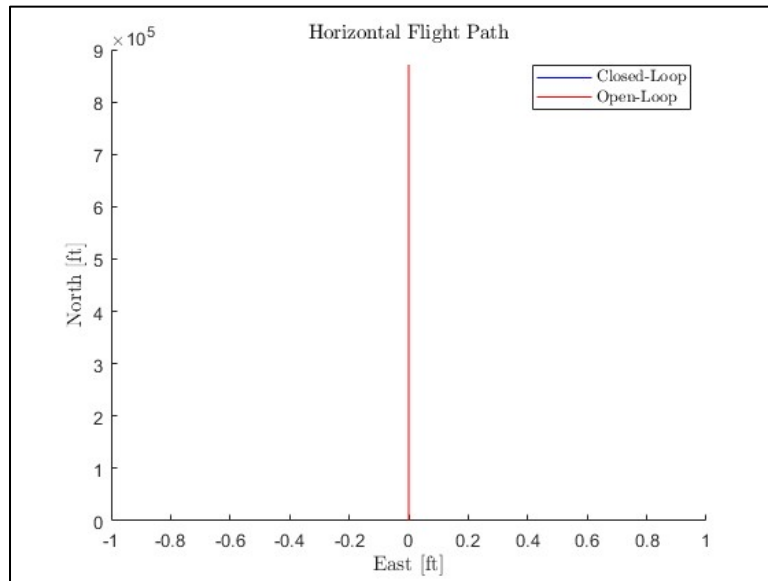


Figure 4-14: Nonlinear Pitch Rate Disturbance Control Inputs

Lastly, the horizontal flight path remains straight due to no lateral control inputs or disturbances.

Yaw Rate Disturbance

Second, the yaw rate was given an initial condition of 2 [deg/s] for the open and close-loop systems applied to the nonlinear model.

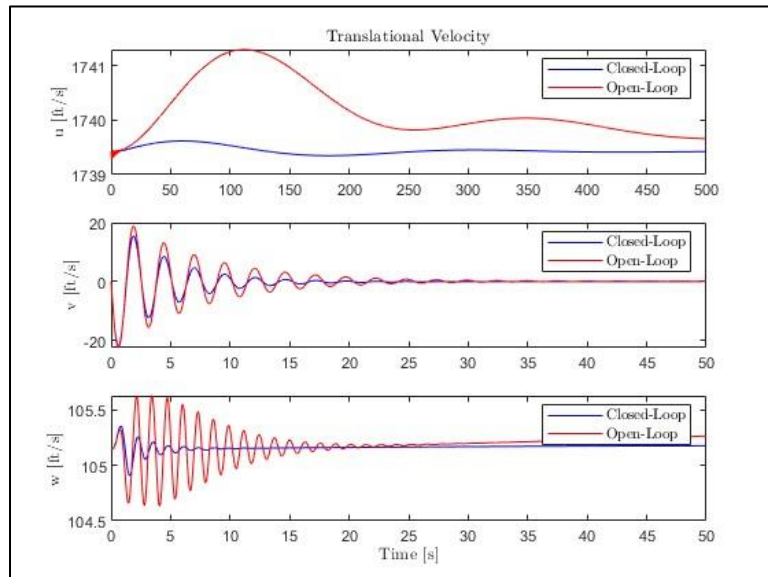


Figure 4-15: Nonlinear Yaw Rate Disturbance Translational Velocities

From the translation velocity responses to the yaw rate disturbance, there are multiple takeaways. The expected outcome of such a disturbance would be Dutch roll, but we can see that the Dutch roll also induces some other dynamics. When modeled in the linear system, the effects of Dutch roll on the longitudinal variables are ignored, but in this case, there are longitudinal effects from Dutch roll dynamics in the full model. It seems that the Dutch roll has induced some long period dynamics in u which are damped out more effectively by the closed-loop system than the open-loop system. Yet, the differences between the oscillations are too large to be accounted for only by the slight increase in the long period damping ratio. Thus, we can assume that the increase in stability in the lateral modes adds to the damping in u , and the oscillations present are not solely due to the phugoid mode. Overall, the feedback control system improved the response to the yaw rate disturbance across every direction. Yet, v did not see a large improvement in settling time, while w did. It can be assumed that the difference between the open-loop and closed-loop system for the lateral model is smaller than the difference in the longitudinal model because the Dutch roll, spiral and roll modes did not need as much improvement as the short period mode.

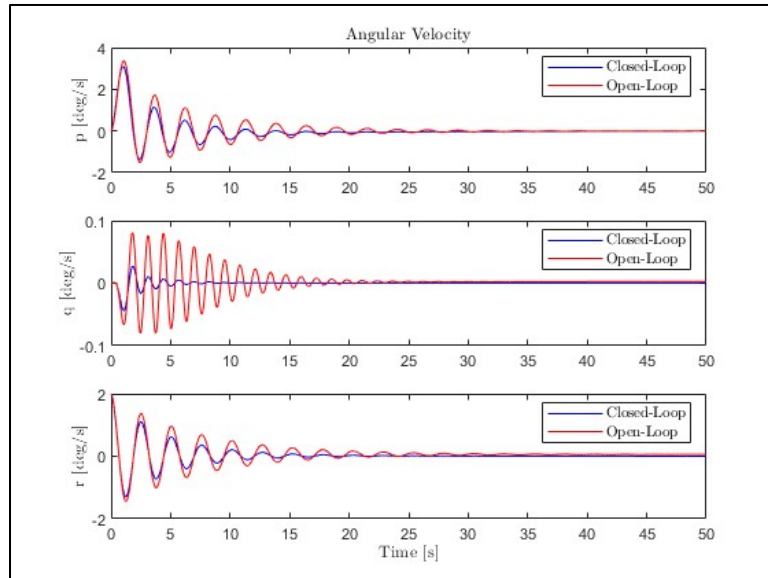


Figure 4-16: Nonlinear Yaw Rate Disturbance Angular Velocities

Again, it seems that the lateral modes are not as affected by the control system. While the roll and yaw rates settle faster with the control active, the differences are not as significant as in the pitch rate. It is again interesting that the yaw rate disturbance induces oscillations in the longitudinal variables, while the pitch rate disturbance did not induce oscillations in the lateral variables.

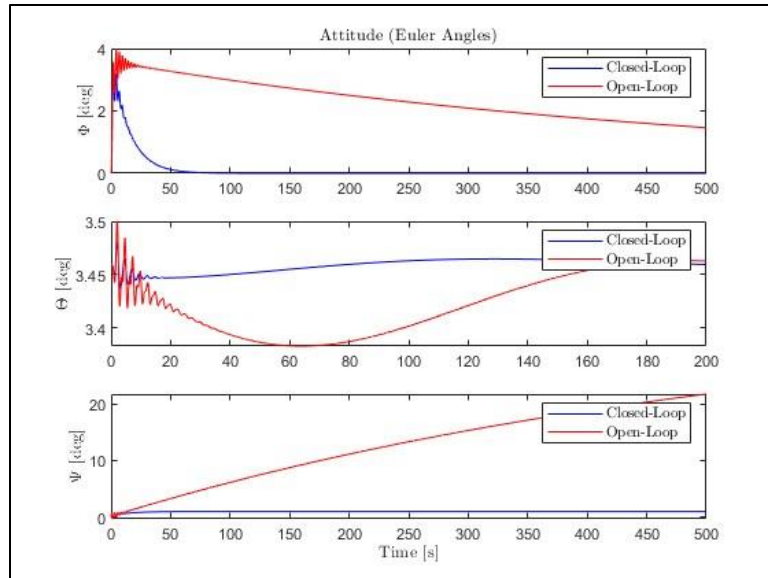


Figure 4-17: Nonlinear Yaw Rate Disturbance Attitude

An interesting aspect of Figure 4-17 can be seen in the roll angle plot. It is evident that the control system has much faster convergence to a zero-roll angle, as expected. The yaw angle also converging to zero in the closed-loop system, while being seemingly unstable in the open-loop system. This is an important indication that the control system is working to return the aircraft to trim, and a large improvement from the open-loop system.

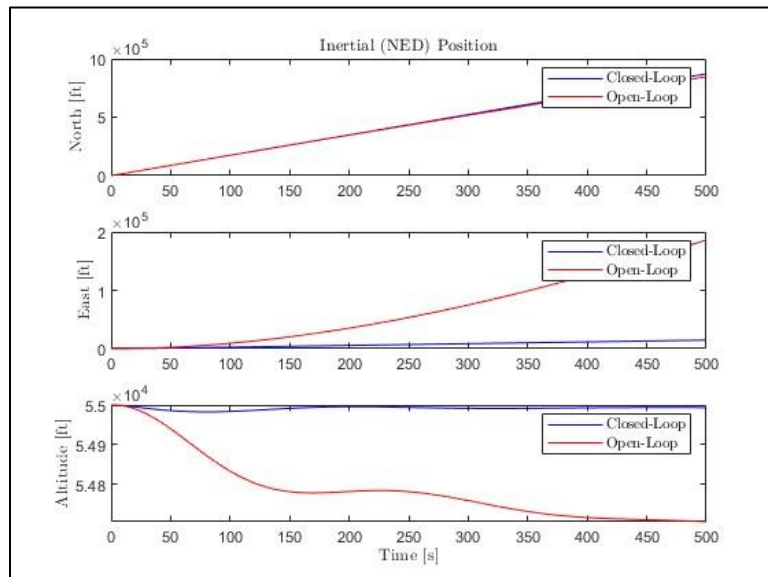


Figure 4-18: Nonlinear Yaw Rate Disturbance Inertial Position

Figure 4-18 again shows that the control system helps to return the aircraft to trim and keep its heading as well as altitude. Again, although altitude is a result of variations in longitudinal variables, the lateral disturbance still affects it, especially in the open-loop system.

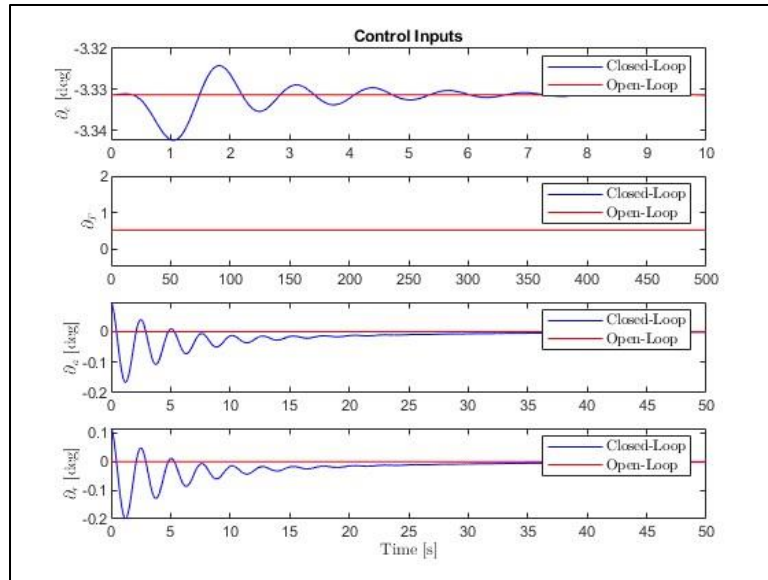


Figure 4-19: Nonlinear Yaw Rate Disturbance Control Inputs

The control inputs again show the expected, where the open-loop control inputs stay at trim, while the closed-loop ones change to damp oscillations and return the aircraft to trim.

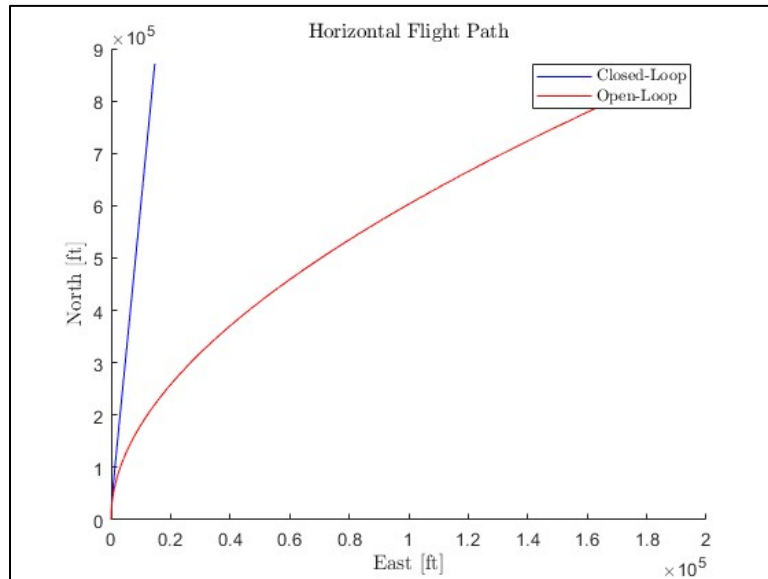


Figure 4-20: Nonlinear Yaw Rate Disturbance Horizontal Flight Path

Lastly, the horizontal flight path also sees the same divergence from trim for the yaw angle as seen in other plots for the open-loop system. The closed-loop system evidently returns to trim, at a similar heading.

Pitch and Yaw Rate Disturbance

Lastly, the yaw and pitch rates were given an initial condition of 2 [deg/s] for the open and closed-loop systems applied to the nonlinear model.

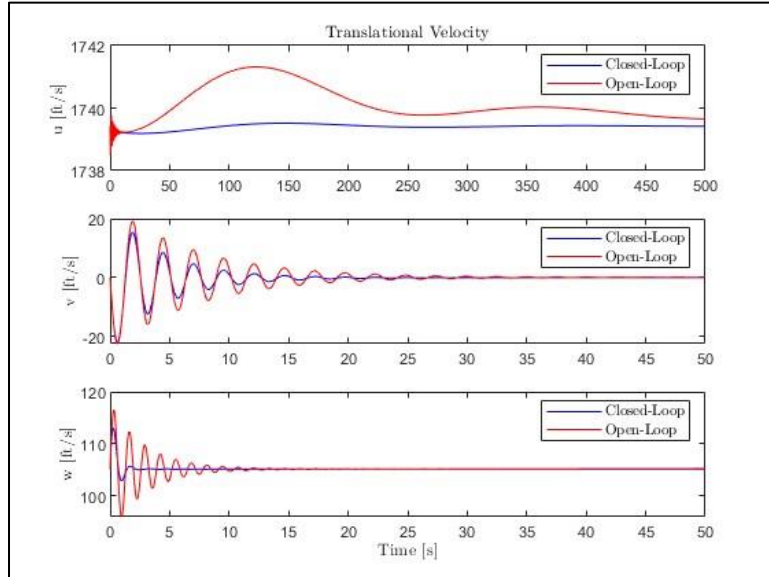


Figure 4-21: Nonlinear Pitch and Yaw Rate Disturbance Translational Velocities

The nonzero pitch and yaw rate initial conditions excited all the modes, with the most prevalent reaction being the Dutch roll dynamics in both the open and closed-loop configurations. The oscillations in v are the largest among the translational velocities, with the closed loop having slight amplitude oscillations. It seems that the longitudinal modes are better controlled by the closed-loop system than the lateral modes.

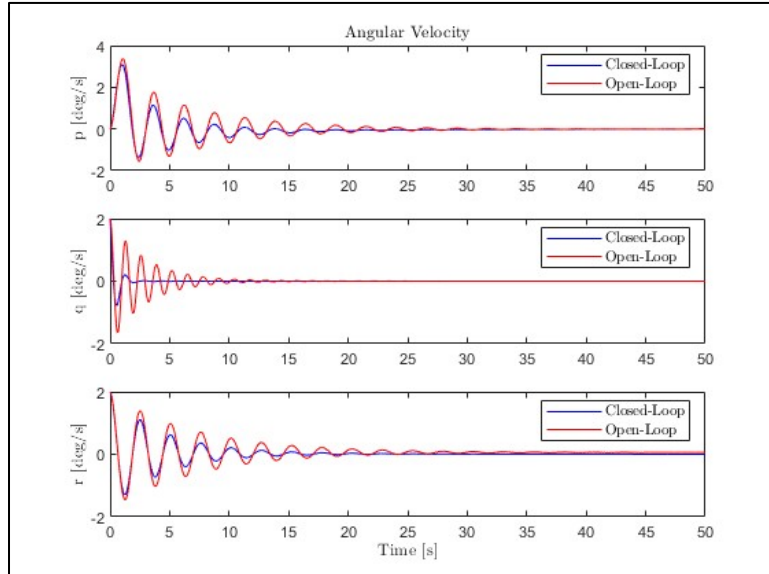


Figure 4-22: Nonlinear Pitch and Yaw Rate Disturbance Angular Velocities

The angular velocities show a similar trend, where the lateral variables are affected the most, suggesting that the control should be edited to have better lateral damping capabilities, specifically for the Dutch roll mode.

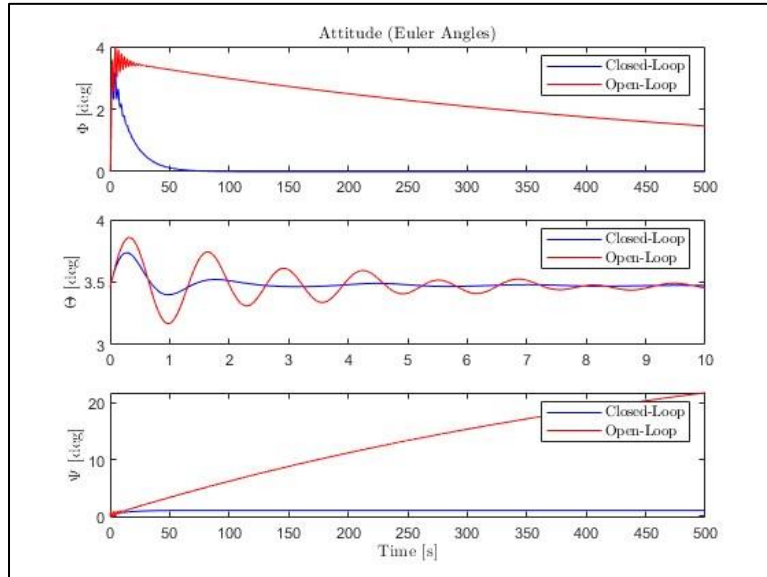


Figure 4-23: Nonlinear Pitch and Yaw Rate Disturbance Attitude

The attitude of the aircraft highlights the improvement of the control in the roll mode, bringing the aircraft to wings level. Additionally, the yaw angle is returned to zero in the close-loop while it is not in the open-loop configuration. Thus, the lateral control system is working, but could be edited specifically for better Dutch roll dynamics.

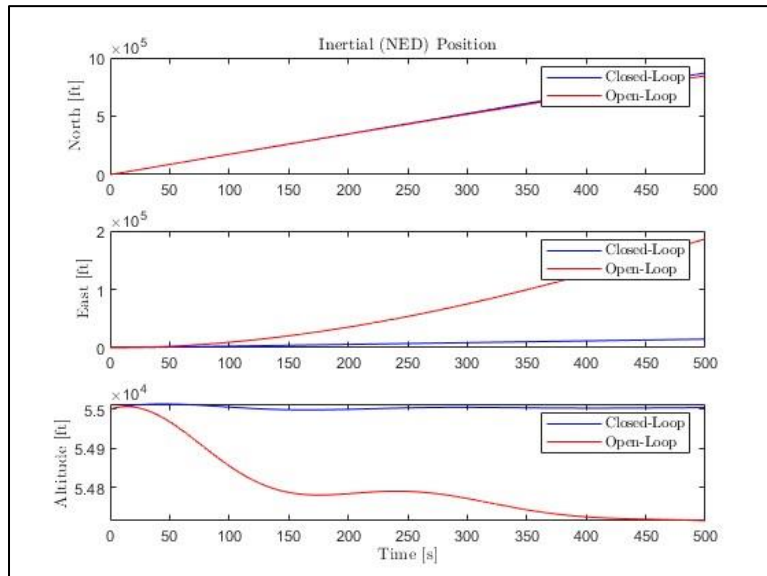


Figure 4-24: Nonlinear Pitch and Yaw Rate Disturbance Inertial Position

Through the inertial position, it is evident that the closed-loop system again brings the aircraft much closer to its initial heading as opposed to the open-loop system. The open-loop system diverges from the initial heading and would be undesirable.

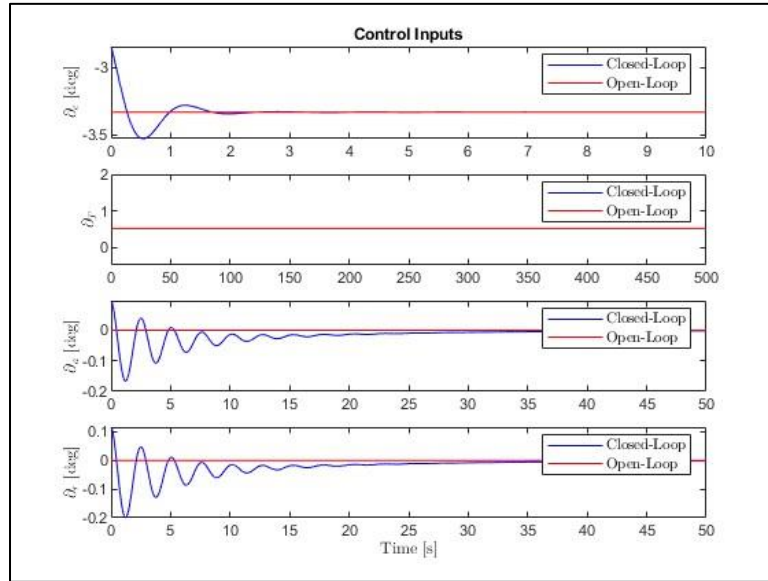


Figure 4-25: Nonlinear Pitch and Yaw Rate Disturbance Control Inputs

The control inputs again act as expected, where the open-loop system control inputs stay at trim conditions, while the closed-loop system has variable control inputs and they eventually return to trim conditions.

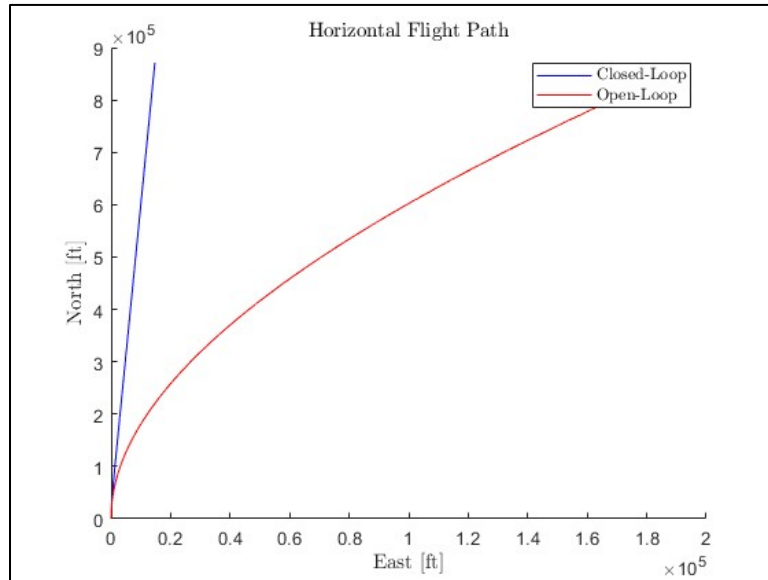


Figure 4-26: Nonlinear Pitch and Yaw Rate Disturbance Horizontal Flight Path

Lastly, the closed-loop system again returns to a heading closer to trim, while the open-loop system diverges.

Autopilot Control Design

Roll Control Autopilot

The roll control autopilot was designed to use the aileron exclusively. Thus, the corresponding system transfer function was used, where the change of aileron is related to the resulting change in roll angle. The following system transfer function was produced using the previously calculated stability derivatives in MATLAB:

$$G_\phi(s) = \frac{\Delta\phi(s)}{\Delta\delta_a(s)} = \frac{\mathcal{L}_{\delta_a}}{s^2 - \mathcal{L}_p s} = \frac{5.334}{s^2 - 0.7911s}$$

The team decided a PID controller would be best for the roll controller as it is the most important controller used for navigation. Using a PID would allow for the most tunability out of the options in the PID family and assure there would be no steady state error. The control goals were then established to find the PID control gains. For ease of tuning, the resulting system of questions was plugged into MATLAB, allowing for the desired values to be changed easily. After tuning, the following desired values were determined as appropriate:

$$\begin{aligned}\bar{\zeta} &= 0.415 \xrightarrow{\text{yields}} 30\% \text{ Overshoot} \\ t_s &= 5 [\text{sec}] \xrightarrow{\text{yields}} \bar{\omega}_n = 1.4458 [\text{rad/s}] \\ \bar{p}_3 &= -1.5(\bar{\omega}_n)(\bar{\zeta})\end{aligned}$$

Note that the 3rd pole needed to be determined due to the use of a PID controller. The following control gains were determined, based on the desired values:

$$\begin{aligned}K_{P,\phi} &= 0.5944 \\ K_{I,\phi} &= 0.3527 \\ K_{D,\phi} &= 0.2454\end{aligned}$$

Using the system transfer function, assuming a perfect actuator and sensor, and implementing a PID controller transfer function, the following closed-loop transfer functions were determined.

$$C(s) = \frac{1.309s^2 + 3.17s + 1.881}{s^3 + 2.1s^2 + 3.17s + 1.881}$$

$$W(s) = \frac{5.334s}{s^3 + 2.1s^2 + 3.17s + 1.881}$$

The resulting closed-loop poles were the following:

$$\lambda_1 = -0.9000$$

$$\lambda_{2,3} = -0.6000 \pm 1.3154i$$

Using Final Value Theorem, the controller could be analyzed to assure there was no steady state error for a step roll command. Evaluating for a step command of 10 degrees:

$$\Delta\phi_{ss}(t) = \lim_{s \rightarrow 0} s C(s) \Delta\phi_{com}(s) = \lim_{s \rightarrow 0} s \left(\frac{1.309s^2 + 3.17s + 1.881}{s^3 + 2.1s^2 + 3.17s + 1.881} \right) \left(\frac{10}{s} \right)$$

$$\Delta\phi_{ss}(t) = 10 \text{ [degrees]}$$

Knowing that the transfer function indicates zero steady-state error, a simulation could be done in the full linearized lateral model where the actuator is not assumed to be perfect, but the sensors are. The simulation was done for a commanded roll angle of 10 degrees, and the results were plotted.

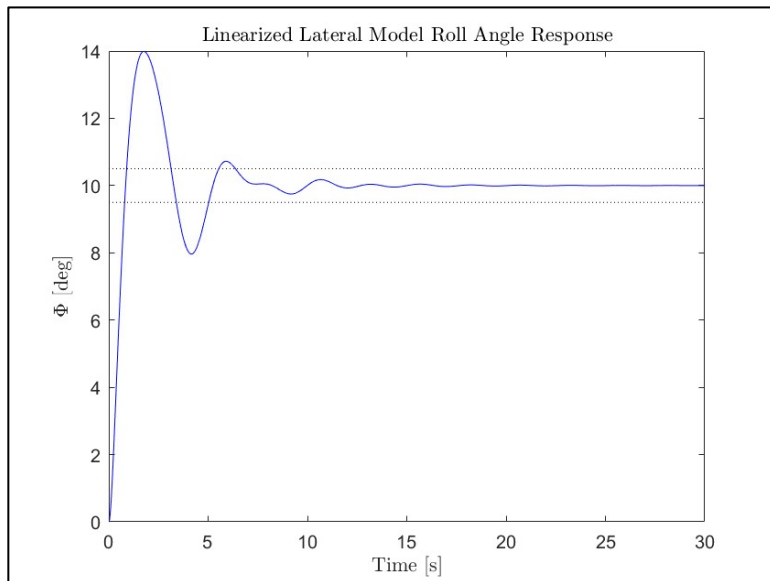


Figure 5-1: Roll Angle Response for a Commanded Roll Angle

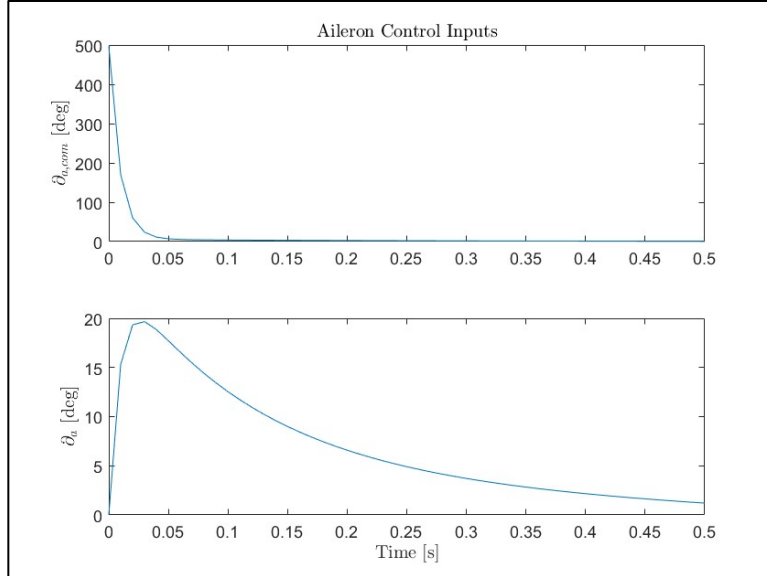


Figure 5-2: Commanded and Actual Aileron Control Input

Using the plots shown in Figure 5-1 and Figure 5-2, the maximum overshoot, maximum aileron deflection, settling time, and steady state error could be estimated as the following:

$$\begin{aligned} M_P &= 39.89 \% \\ \delta_{a,max} &= 19.6669 [\text{degrees}] \\ t_s &= 6.37 [\text{s}] \\ E_{ss} &= 0 [\text{degrees}] \end{aligned}$$

These transient parameters satisfied the team members, while keeping the aileron deflection under the maximum of 20 degrees. Thus, the team members moved to the next controller.

Heading Hold Autopilot

The sideslip control autopilot was designed to use the rudder exclusively. Thus, the corresponding system transfer function was used:

$$G_\beta(s) = \frac{\Delta\beta(s)}{\Delta\delta_r(s)} = \frac{0.005452s + 1.591}{s^2 + 0.2602s + 5.737}$$

The team decided a PID controller would be best for the sideslip controller, again because of the tunability. The control goals were then established to find the PID control gains. For ease of tuning, the resulting system of questions was plugged into MATLAB, allowing for the desired values to be changed easily. After tuning, the following desired values were determined as appropriate:

$$\begin{aligned} \bar{\zeta} &= 0.216 \xrightarrow{\text{yields}} 50\% \text{ Overshoot} \\ t_s &= 15 [\text{sec}] \xrightarrow{\text{yields}} \bar{\omega}_n = 0.9259 [\text{rad/s}] \\ \bar{p}_3 &= -10 (\bar{\omega}_n)(\bar{\zeta}) \end{aligned}$$

Note that the 3rd pole needed to be determined due to the use of a PID controller. After extensive tuning, the following control gains were determined, based on the desired values:

$$\begin{aligned} K_{P,\beta} &= -2.5607 \\ K_{I,\beta} &= 1.0859 \\ K_{D,\beta} &= 1.3651 \end{aligned}$$

Having a negative K_p is normally not desired, but the team found that this was the only reasonable result for the PID sideslip controller. The controller tended to reach values unattainable by the actual aircraft due to rudder deflection limitations. Even in this extreme case, the rudder command still accumulates to a maximum value higher than what is capable of the aircraft. This can be explained by the trim conditions, where the aircraft is at supersonic conditions. It seems that the rudder at this trim condition has little control authority and could be part of the reason for the aforementioned characteristic to spin. Thus, using the system transfer function, assuming a perfect actuator and sensor, and implementing the PID controller transfer function, the following closed-loop transfer functions were determined.

$$\begin{aligned} C(s) &= \frac{0.007387s^3 + 2.142s^2 - 4.037s + 1.715}{s^3 + 2.4s^2 + 1.657s + 1.715} \\ W(s) &= \frac{0.005411s^2 + 1.579s}{s^3 + 2.4s^2 + 1.657s + 1.715} \end{aligned}$$

The resulting closed-loop poles were the following:

$$\begin{aligned} \lambda_1 &= -2.0000 \\ \lambda_{2,3} &= -0.2000 \pm 0.9041i \end{aligned}$$

Using Final Value Theorem, the controller could be analyzed to assure there was no steady state error for a step roll command. Evaluating for a step command of 10 degrees:

$$\begin{aligned} \Delta\beta_{ss}(t) &= \lim_{s \rightarrow 0} s C(s) \Delta\beta_{com}(s) = \lim_{s \rightarrow 0} s \left(\frac{0.007387s^3 + 2.142s^2 - 4.037s + 1.715}{s^3 + 2.4s^2 + 1.657s + 1.715} \right) \left(\frac{10}{s} \right) \\ \Delta\beta_{ss}(t) &= 2 \text{ [degrees]} \end{aligned}$$

Knowing that the transfer function indicates zero steady-state error, a simulation could be done in the full linearized lateral model where the actuator is not assumed to be perfect, but the sensors are. The simulation was done for a commanded sideslip angle of 2 degrees, and the results were plotted.

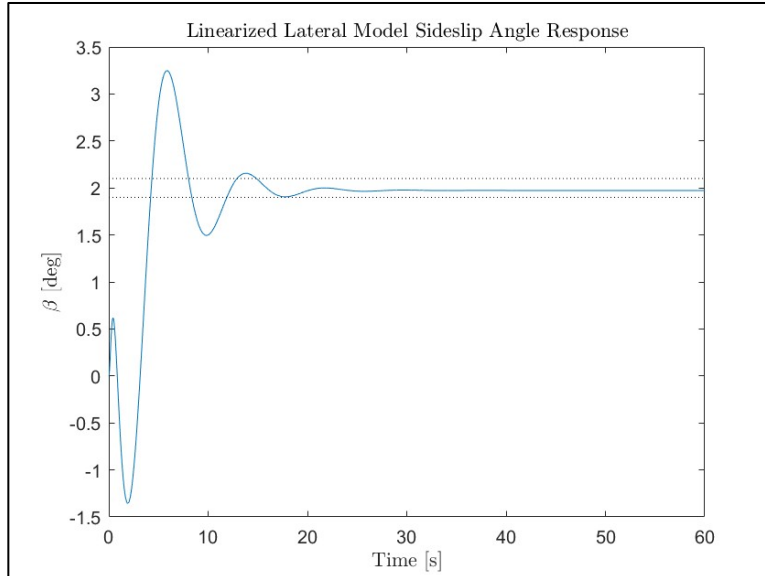


Figure 5-3: Sideslip Angle Response for a Commanded Sideslip Angle

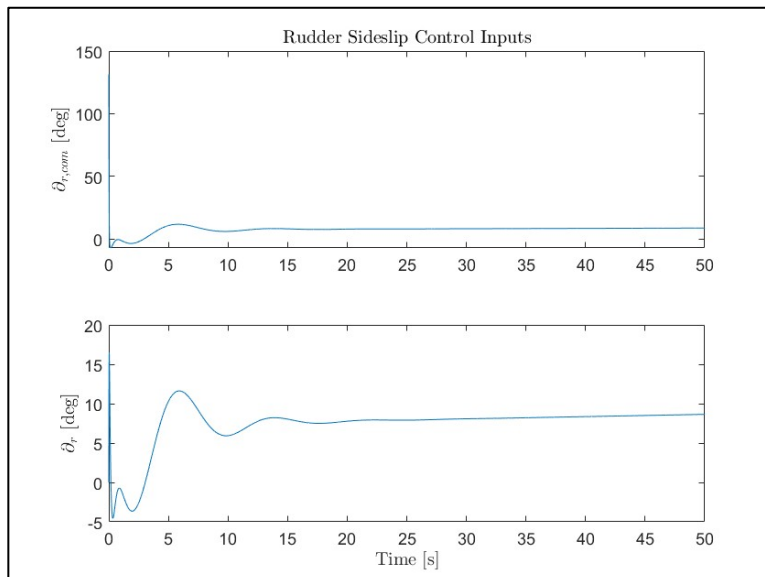


Figure 5-4: Commanded and Actual Rudder Control Input

Using the plots shown in Figure 5-3 and Figure 5-4, the maximum overshoot, maximum aileron deflection, settling time, and steady state error could be estimated as the following:

$$\begin{aligned}
 M_P &= 62.42 \% \\
 \delta_{r,max} &= 29.4275 [\text{degrees}] \\
 t_s &= 14.9 [\text{s}] \\
 E_{ss} &= 0.070 [\text{degrees}]
 \end{aligned}$$

These transient parameters satisfied the team members, while keeping the rudder deflection under the maximum of 20 degrees for most of the simulation. Thus, the team members moved to integrating the two lateral controllers to perform a coordinated turn.

Roll and Sideslip Control Autopilot

With both the roll and sideslip controls created, they could then be tested together. As directed, a commanded roll angle was set with zero sideslip. These conditions, being that of a coordinated turn, are crucial for waypoint navigation. The roll angle command was set to 10 degrees, while keeping the sideslip at 0 degrees. The resulting simulation using the linearized lateral model was plotted and shown below.

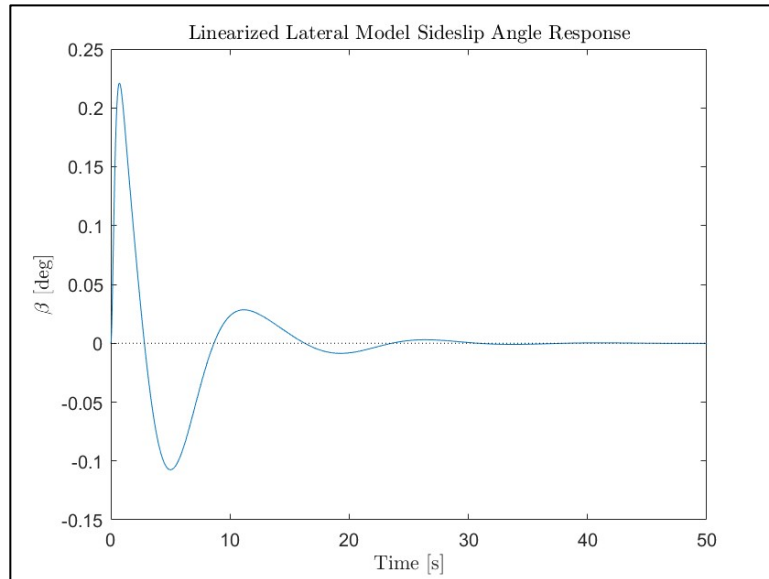


Figure 5-5: Coordinated Turn Sideslip Angle Response for a Commanded Sideslip Angle

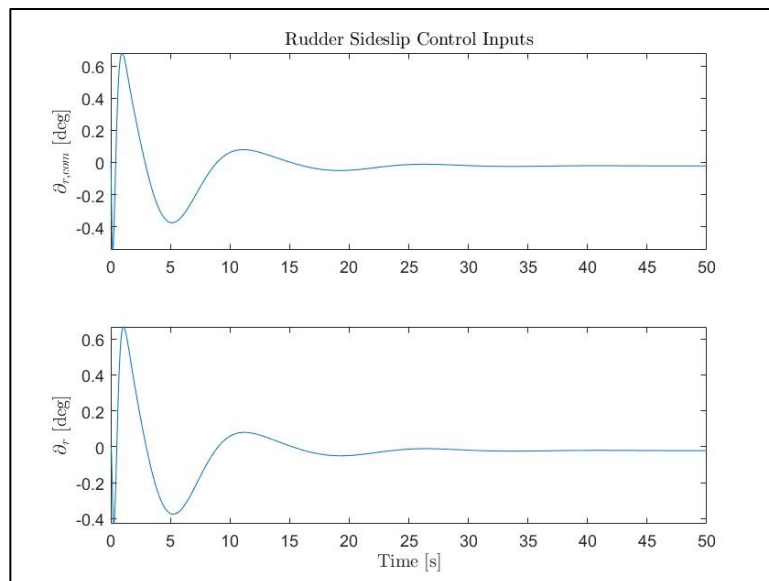


Figure 5-6: Coordinated Turn Commanded and Actual Rudder Control Input

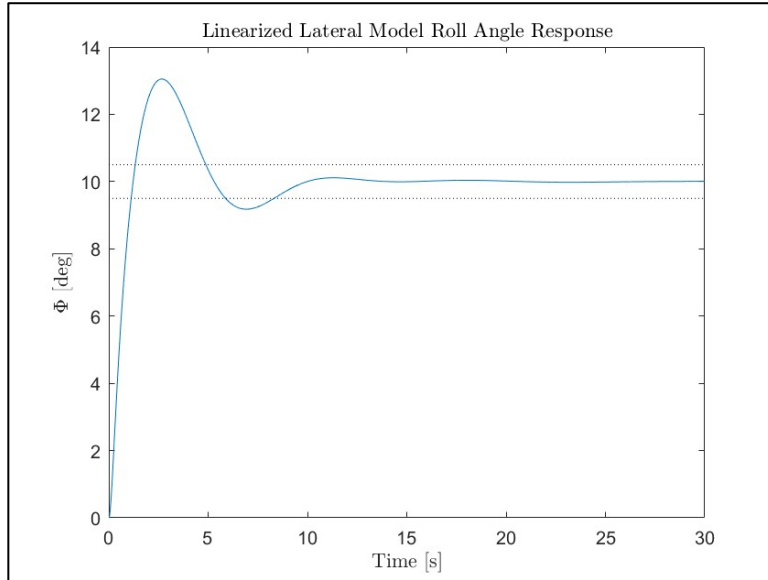


Figure 5-7: Coordinated Turn Roll Angle Response for a Commanded Roll Angle

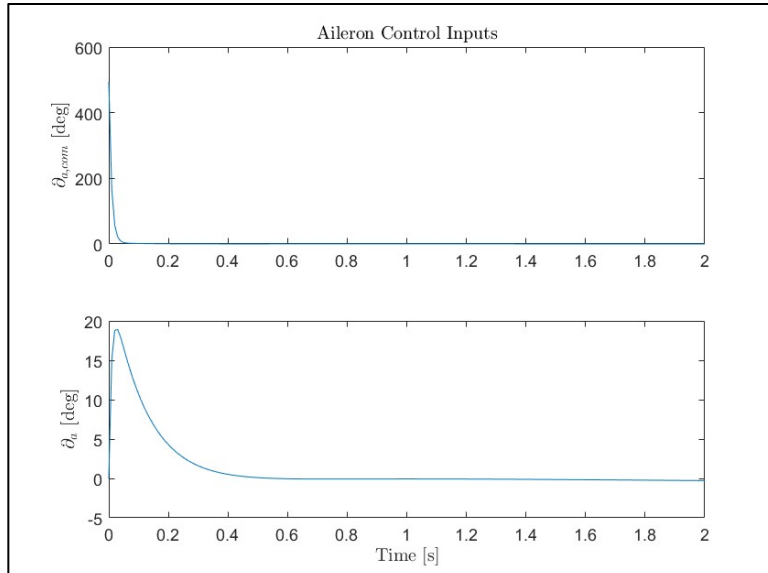


Figure 5-8: Coordinated Turn Commanded and Actual Aileron Control Input

As shown in the various plots, the aircraft rolls to the desired roll angle, and the sideslip control stabilizes to zero sideslip. Thus, the coordinated turn was completed and the roll and sideslip controls were successful.

Altitude Hold Autopilot

The altitude hold was designed to use the elevator exclusively. Again, the corresponding system transfer function was used. Yet, for this control system, the longitudinal A and B matrices needed to be edited to include the altitude as one of the states. The altitude equation was first linearized, and then added to the A matrix. Since the altitude is not directly controlled by the thrust or elevator, a row of zeros was added to the B matrix. The following is the system transfer function for the altitude hold autopilot:

$$G_h(s) = \frac{\Delta h(s)}{\Delta \delta_e(s)} = \frac{47.58s^3 + 1.708s^2 - 5136s - 7.043}{s^5 + 0.638s^4 + 23.72s^3 + 0.3035s^2 - 0.01661s}$$

Instead of assuming a perfect actuator, the following transfer function was used to represent the actuator dynamics, accounting for the need to flip the sign of the elevator for altitude control:

$$G_a(s) = \frac{-10}{s + 10}$$

The Ziegler Nichols method was then used to find the ultimate gain and ultimate period, using the system and actuator transfer functions.

$$\begin{aligned} K_{Pu} &= 4.0908 \times 10^{-4} \\ T_u &= 20.9929 \text{ [sec]} \end{aligned}$$

A PID controller was then deemed accurate, after other controllers in the PID family were experimented on. The resulting PID gains were the following:

$$\begin{aligned} K_{P,h} &= 5.7271 \times 10^{-4} \\ K_{I,h} &= 2.3384 \times 10^{-5} \\ K_{D,h} &= 0.0018 \end{aligned}$$

With these control gains, the closed-loop transfer functions become:

$$\begin{aligned} C(s) &= \frac{-0.8581s^5 - 0.3033s^4 + 92.6s^3 + 29.54s^2 - 1.241s - 0.001647}{s^7 + 10.64s^6 + 29.24s^5 + 237.2s^4 + 95.65s^3 + 29.71s^2 - 1.241s + 0.001647} \\ W(s) &= \frac{47.58s^5 + 477.5s^4 - 5119s^3 - 5.137 \times 10^4 s^2 - 70.43s}{s^7 + 10.64s^6 + 29.24s^5 + 237.2s^4 + 95.65s^3 + 29.71s^2 - 1.241s + 0.001647} \end{aligned}$$

With the following corresponding poles:

$$\begin{aligned} \lambda_1 &= -9.9940 \\ \lambda_{2,3} &= -0.1174 \pm 4.7503i \\ \lambda_{4,5} &= -0.1805 \pm 0.2846i \\ \lambda_6 &= -0.0469 \\ \lambda_7 &= -0.0014 \end{aligned}$$

Using Final Value Theorem, the controller could be analyzed to assure there was no steady state error for a step altitude command. Evaluating for a step command of 10 feet:

$$\Delta\phi_{ss}(t) = \lim_{s \rightarrow 0} s C(s) \Delta\phi_{com}(s)$$

$$\Delta\phi_{ss} = \lim_{s \rightarrow 0} s \left(\frac{-0.8581s^5 - 0.3033s^4 + 92.6s^3 + 29.54s^2 - 1.241s - 0.001647}{s^7 + 10.64s^6 + 29.24s^5 + 237.2s^4 + 95.65s^3 + 29.71s^2 - 1.241s + 0.001647} \right) \frac{10}{s}$$

$$\Delta\phi_{ss}(t) = 10 [ft]$$

Knowing that the transfer function indicates zero steady-state error, a simulation could be done in the full linearized longitudinal model. The simulation was done for a commanded change of altitude of 10 feet, and the results were plotted.

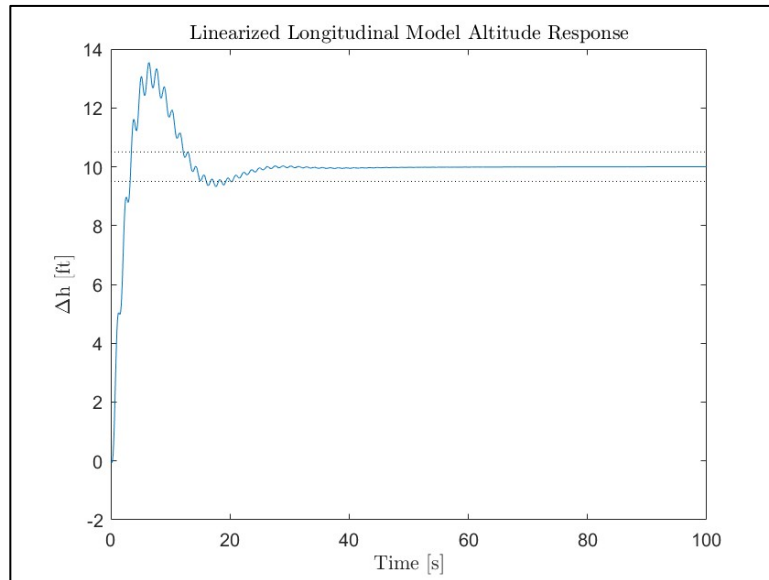


Figure 5-9: Altitude Response for a Step Altitude Command

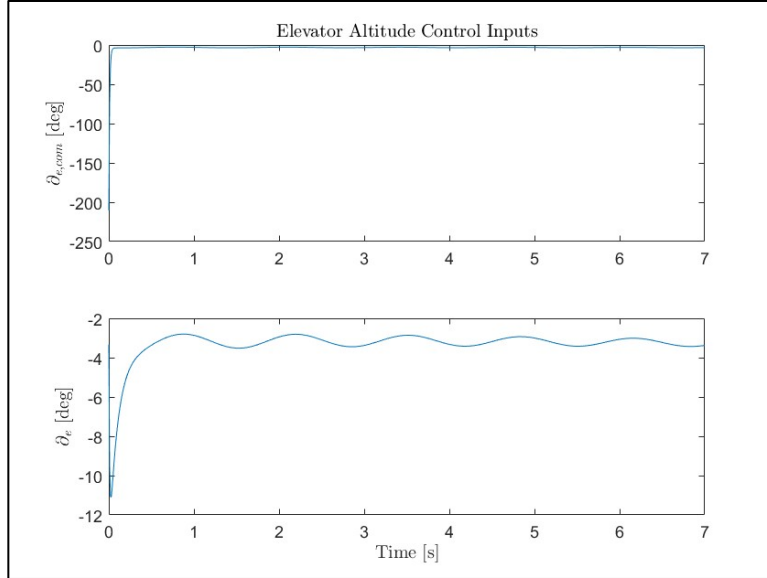


Figure 5-10: Elevator Control Inputs for a Step Altitude Command

Using the plots shown in Figure 5-3 and Figure 5-4, the maximum overshoot, maximum aileron deflection, settling time, and steady state error could be estimated as the following:

$$\begin{aligned} M_p &= 35.41 \% \\ \delta_{e,max} &= 11.0880 [\text{degrees}] \\ t_s &= 20.36 [\text{s}] \\ E_{ss} &= 0 [\text{ft}] \end{aligned}$$

These transient parameters satisfied the team members, while keeping the elevator deflection under the maximum of 20 degrees. Thus, the team members moved to the next controller.

Velocity Hold Autopilot

The velocity hold was designed to use thrust exclusively. As with the prior controllers, the system transfer function was found:

$$G_u(s) = \frac{\Delta u(s)}{\Delta \delta_T(s)} = \frac{28.07s^3 + 17.63s^2 - 662.9s - 0.7382}{s^4 + 0.638s^3 + 23.72s^2 + 0.3035s - 0.01661}$$

Again, instead of assuming a perfect actuator, the following transfer function was used to model the actuator dynamics:

$$G_a(s) = \frac{10}{s + 10}$$

In addition to modeling for the actuator dynamics, this control also took into account the lag of the F4's twin jet engines with the following transfer function:

$$G_a(s) = \frac{0.1}{s + 0.1}$$

The Ziegler Nichols method was then used to find the ultimate gain and ultimate period, using the system, actuator, and engine lag transfer functions.

$$\begin{aligned} K_{P,u} &= 0.4036 \\ T_u &= 5.9427 [\text{sec}] \end{aligned}$$

A PID controller was then deemed adequate, after other controllers in the PID family were experimented on. The resulting PID gains were the following:

$$\begin{aligned} K_{P,u} &= 0.0484 \\ K_{I,u} &= 0.0034 \\ K_{D,h} &= 0.0300 \end{aligned}$$

With these control gains, the closed-loop transfer functions become:

$$\begin{aligned} C(s) &= \frac{0.8416s^5 + 1.888s^4 + 20.82s^3 + 32.15s^2 + 2.215s - 0.002507}{s^7 + 10.74s^6 + 32.01s^5 + 242.4s^4 + 47.63s^3 + 32.62s^2 - 2.232s - 0.002507} \\ W(s) &= \frac{28.07s^6 + 301.2s^5 + 869.1s^4 + 6713s^3 + 655.5s^2 - 0.7382s}{s^7 + 10.74s^6 + 32.01s^5 + 242.4s^4 + 47.63s^3 + 32.62s^2 + 2.232s - 0.002507} \end{aligned}$$

With the following corresponding poles:

$$\begin{aligned} \lambda_1 &= -9.92282 \\ \lambda_{2,3} &= -0.3127 \pm 4.8596i \\ \lambda_{4,5} &= -0.0555 \pm 0.3552i \\ \lambda_6 &= -0.0745 \\ \lambda_7 &= 0.0011 \end{aligned}$$

Using Final Value Theorem, the controller could be analyzed to assure there was no steady state error for a step velocity command. Evaluating for a step command of 10 feet per second:

$$\Delta\phi_{ss}(t) = \lim_{s \rightarrow 0} s C(s) \Delta\phi_{com}(s)$$

$$\Delta\phi_{ss} = \lim_{s \rightarrow 0} s \left(\frac{0.8416s^5 + 1.888s^4 + 20.82s^3 + 32.15s^2 + 2.215s - 0.002507}{s^7 + 10.74s^6 + 32.01s^5 + 242.4s^4 + 47.63s^3 + 32.62s^2 - 2.232s - 0.002507} \right) \frac{10}{s}$$

$$\Delta\phi_{ss}(t) = 10 [\text{ft/s}]$$

Knowing that the transfer function indicates zero steady-state error, a simulation could be done in the full linearized longitudinal model. The simulation was done for a commanded change of velocity of 10 feet per second, and the results were plotted. Note that the trim thrust command was added to the control inputs to ensure the aircraft stayed with the thrust control limits in its response to the step input.

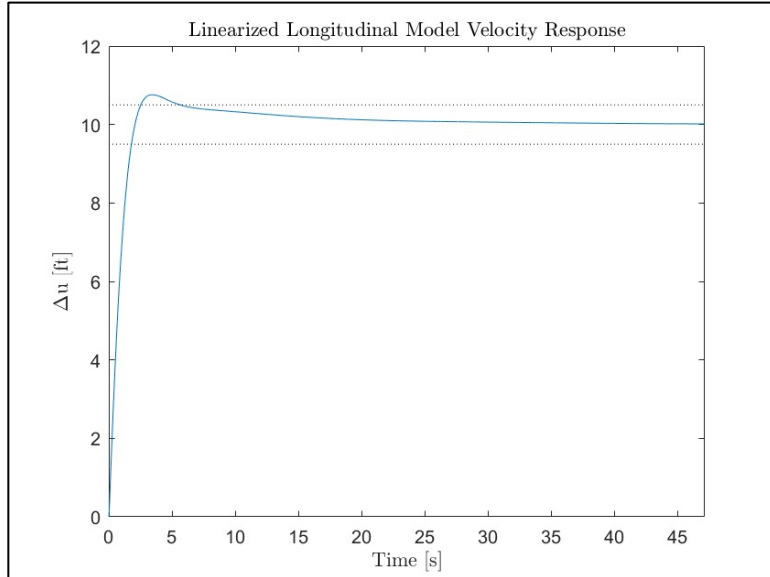


Figure 5-11: Velocity Response for a Step Velocity Command

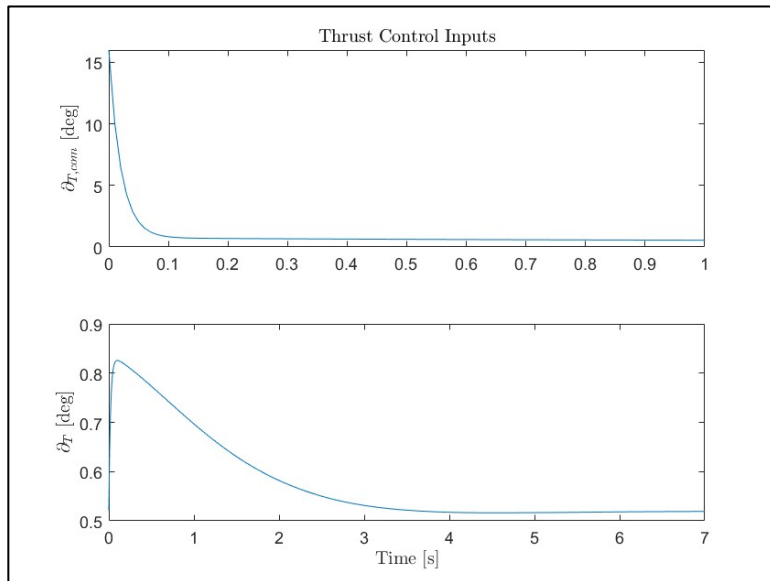


Figure 5-12: Thrust Control Inputs for a Step Velocity Command

Using the plots shown in Figure 5-5 and Figure 5-6, the maximum overshoot, maximum aileron deflection, settling time, and steady state error could be estimated as the following:

$$M_P = 7.58 \%$$

$$\begin{aligned}\delta_{e,max} &= 0.8258 \\ t_s &= 5.3 [s] \\ E_{ss} &= 0 [ft/s]\end{aligned}$$

These transient parameters satisfied the team members, while keeping the thrust command under the maximum of 1. Thus, the team members could now evaluate the altitude and velocity holds work together.

Altitude and Velocity Hold Autopilot

Now, testing the integrated longitudinal control system, the altitude and velocity controllers were activated at the same time. The first test gave an initial displacement of 10 feet in change of altitude and a commanded trim altitude and trim velocity. The following plots display the results of the simulation.

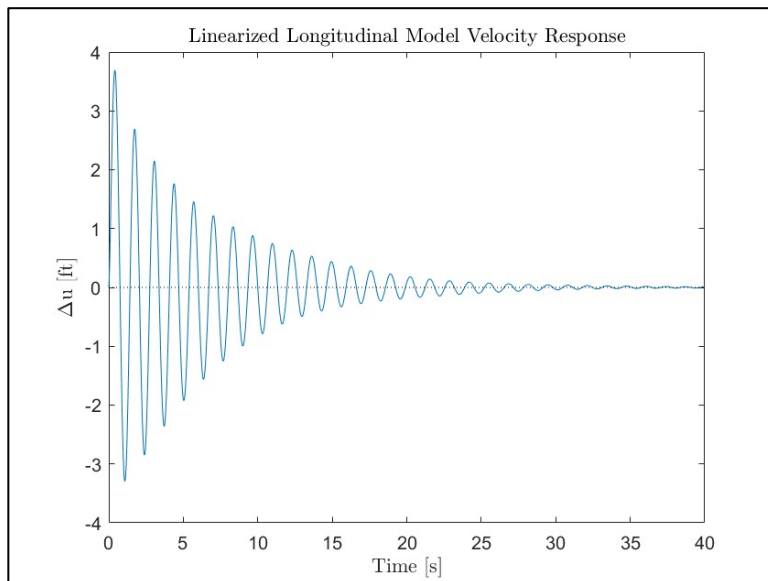


Figure 5-13: Velocity Response for Initial Altitude Displacement

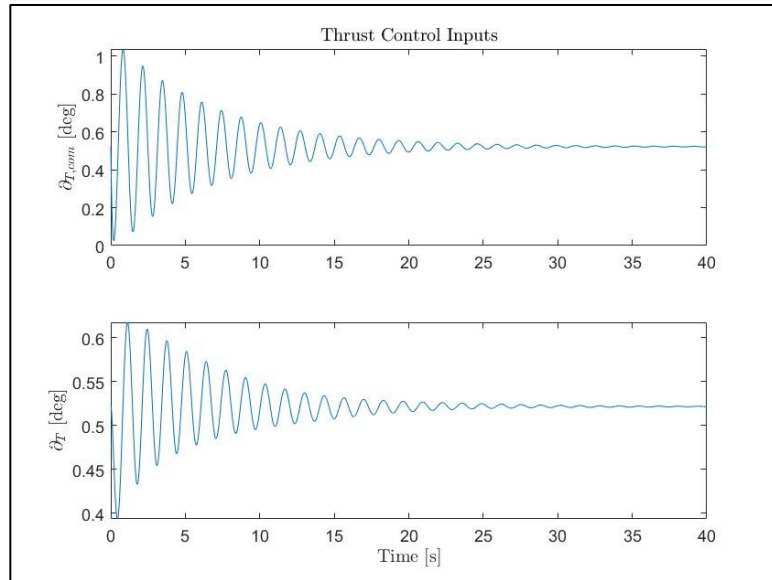


Figure 5-14: Thrust Commands for Initial Altitude Displacement

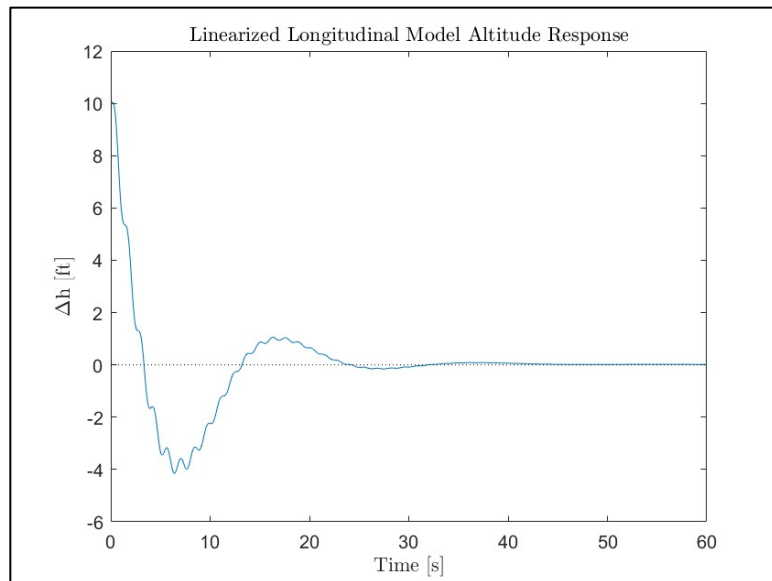


Figure 5-15: Altitude Response for Initial Altitude Displacement

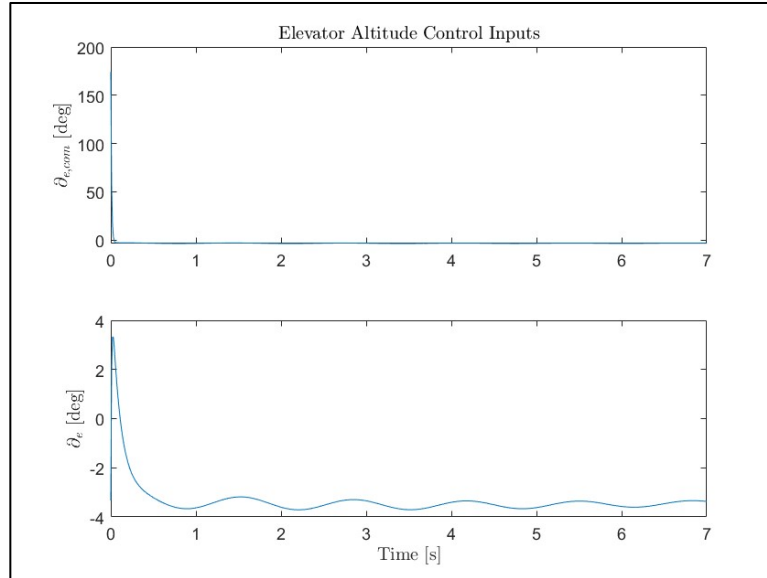


Figure 5-16: Elevator Commands for Initial Altitude Displacement

From the various figures, it is evident that the full integrated control system is working. The altitude is returned to trim over a reasonable interval of time, while the resulting change in velocity is removed by thrust commands. The transient characteristics of the velocity are not perfect but are reasonable due to the jet lag and actuator dynamics. The next test gave an initial displacement of 10 feet per second in change of velocity and a commanded trim altitude and trim velocity. The following plots display the results of the simulation.

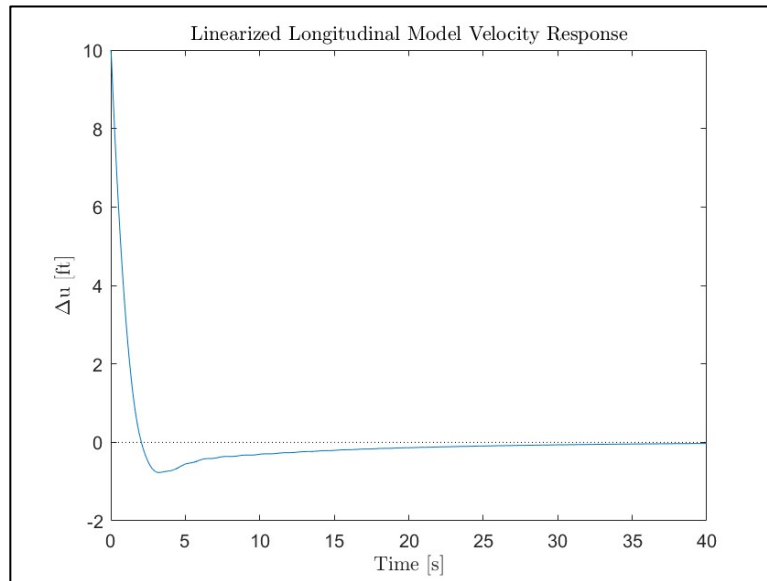


Figure 5-17: Velocity Response for Initial Velocity Displacement

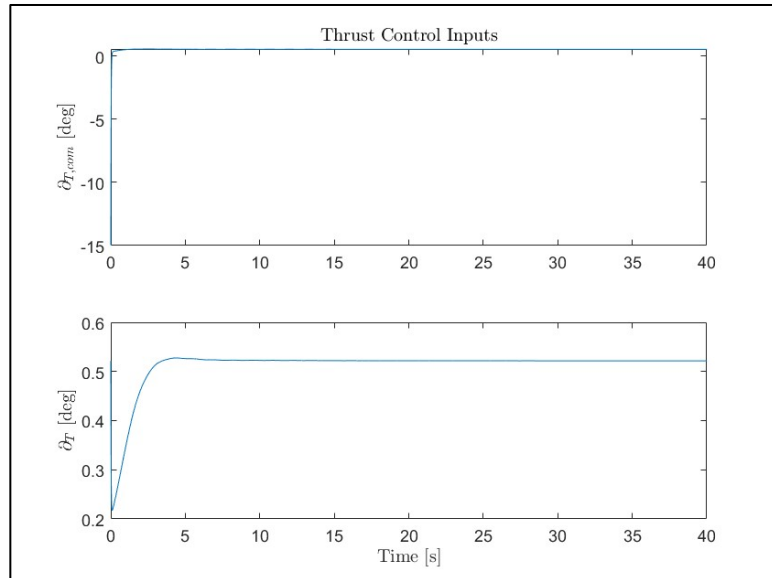


Figure 5-18: Thrust Commands for Initial Velocity Displacement

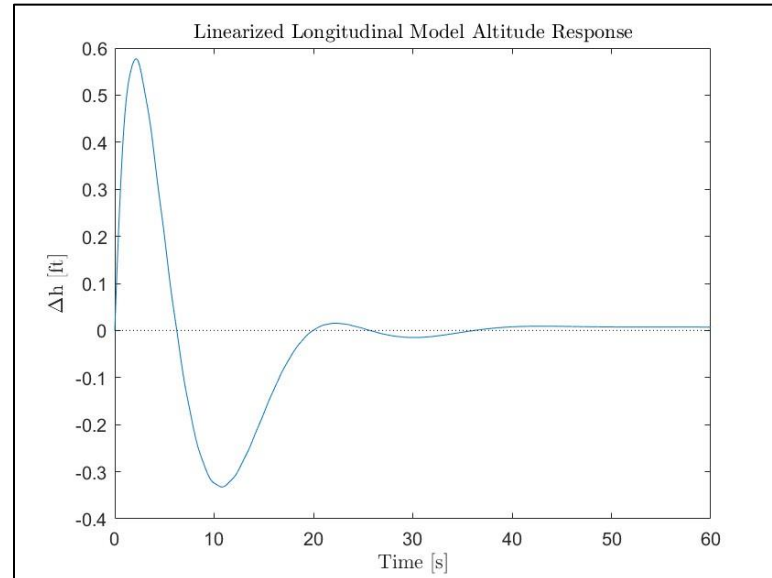


Figure 5-19: Altitude Response for Initial Velocity Displacement

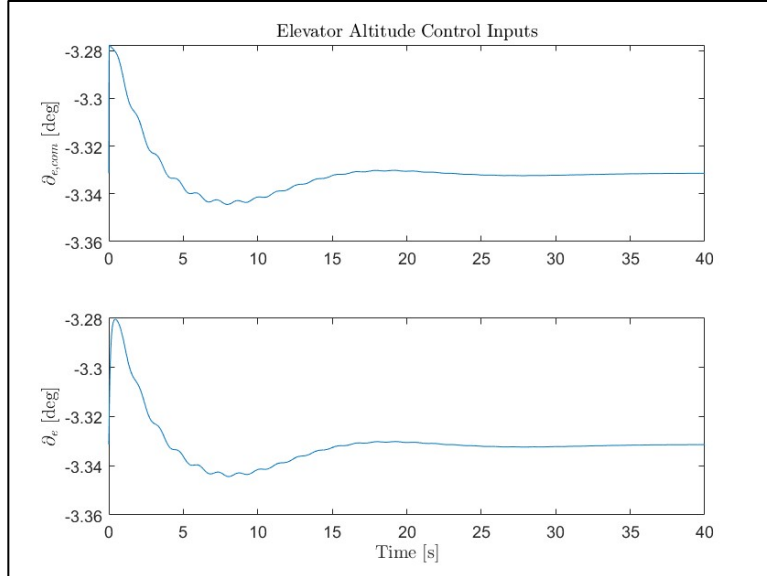


Figure 5-20: Elevator Commands for Initial Velocity Displacement

Like the first test, it is evident that the controllers are working. Both the velocity and altitude are returned to trim with reasonable elevator and thrust commands. The longitudinal controls are verified.

Waypoint Navigation

Waypoint Navigation Overview and Control Implementation

The navigation simulation set 5 waypoints for the aircraft to navigate to. Using its current heading, the algorithm determined a desired roll angle such that the aircraft banks and turns towards the desired waypoint. Based on the trim velocity, the waypoint radii are set, determining how close to the point the aircraft needs to get to say it reached the waypoint.

The provided waypoint navigation Simulink model needed to be edited for the F4 by replacing the propellor engine model with a jet engine model. After that, the PID controllers needed to be slightly edited by adding the variables to be defined in the .m file to tune the PID controllers. The four controllers implemented in the Simulink model are the same ones found in the Autopilot Control Design section. In this case, however, saturation limits are applied, and thus if the control system is asking for rudder past the limit, the rudder will stay at the limit.

Simulation Results and Controller Performance

Initially, the controls designed in the Autopilot Control Design section of the report were implemented into the model. These controllers did not work and resulted in the aircraft spinning and nose-diving into the ground. Even after extensive tuning, the aircraft was never adequately controlled, and the waypoints were never reached. One of the attempts has been plotted and will be discussed.

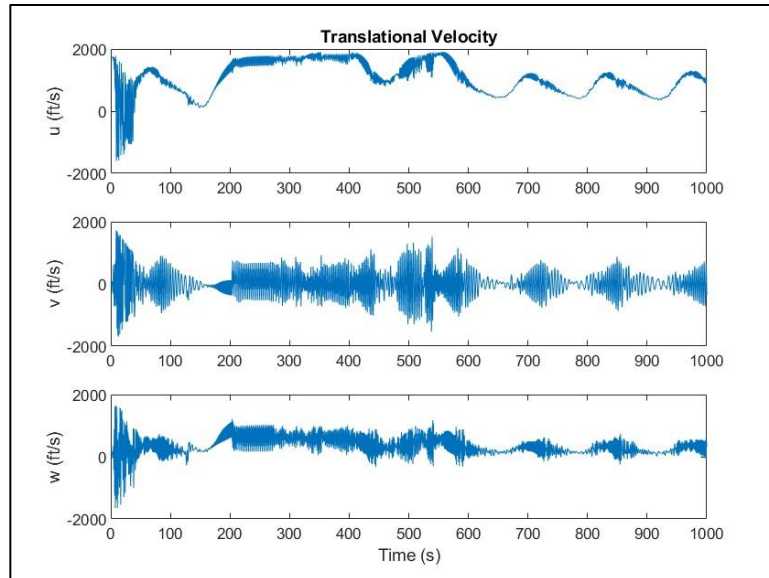


Figure 6-1: Translational Velocities for Waypoint Navigation

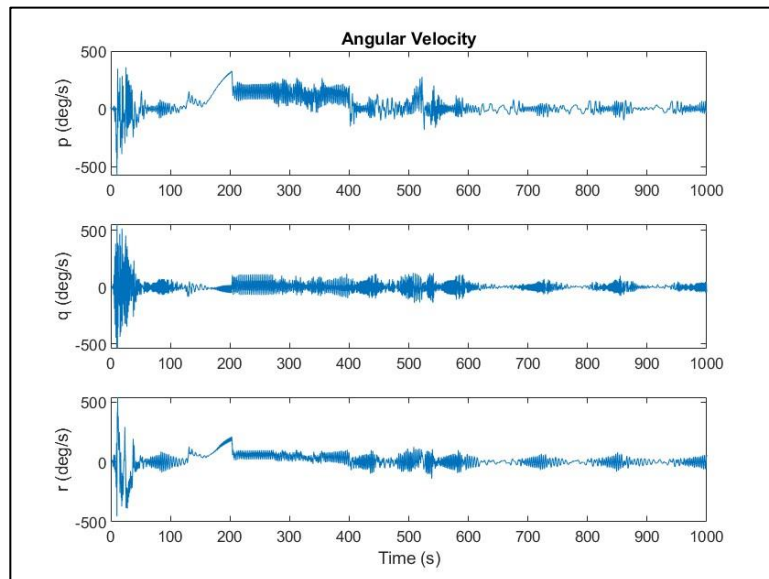


Figure 6-2: Angular Velocities for Waypoint Navigation

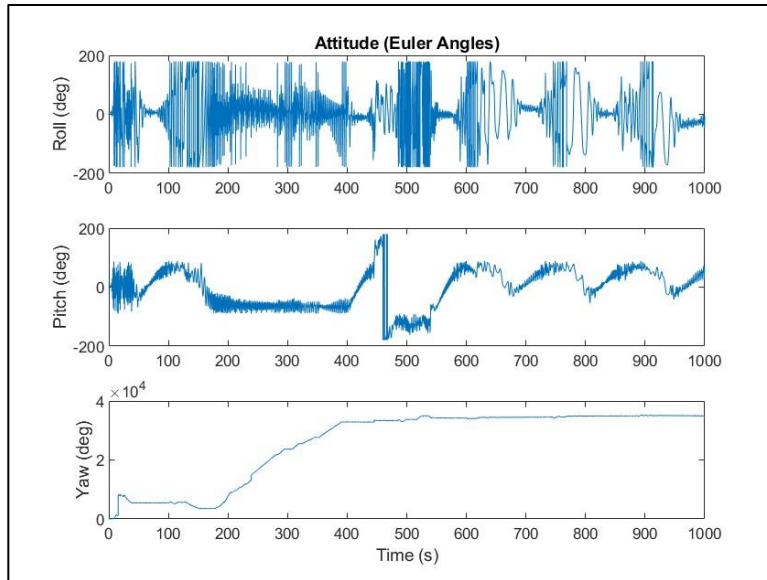


Figure 6-3: Attitude for Waypoint Navigation

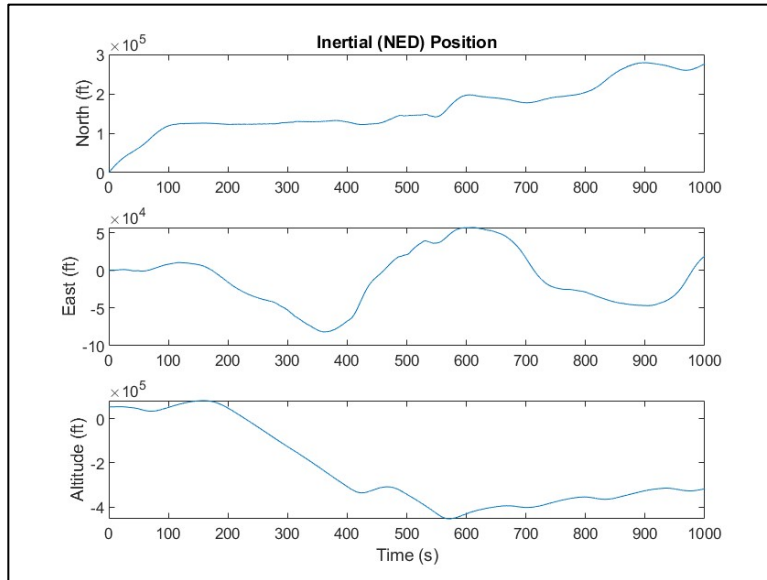


Figure 6-4: Inertial Position for Waypoint Navigation

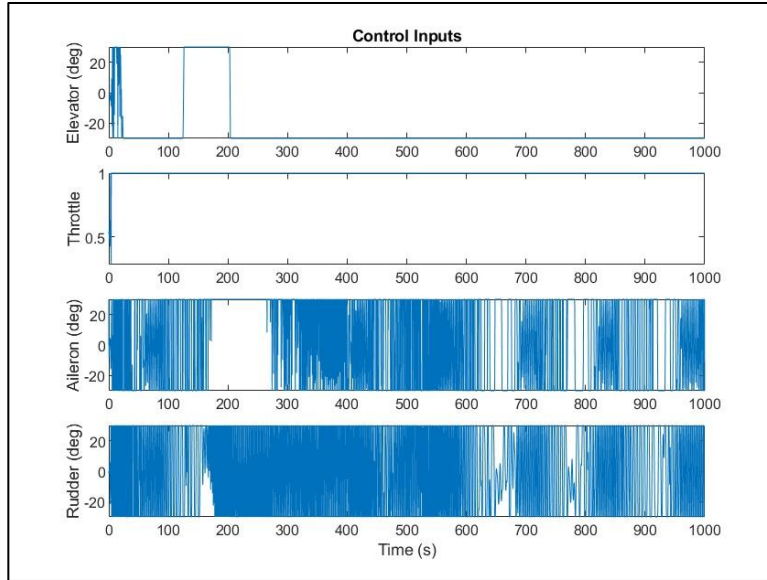


Figure 6-5: Control Inputs for Waypoint Navigation

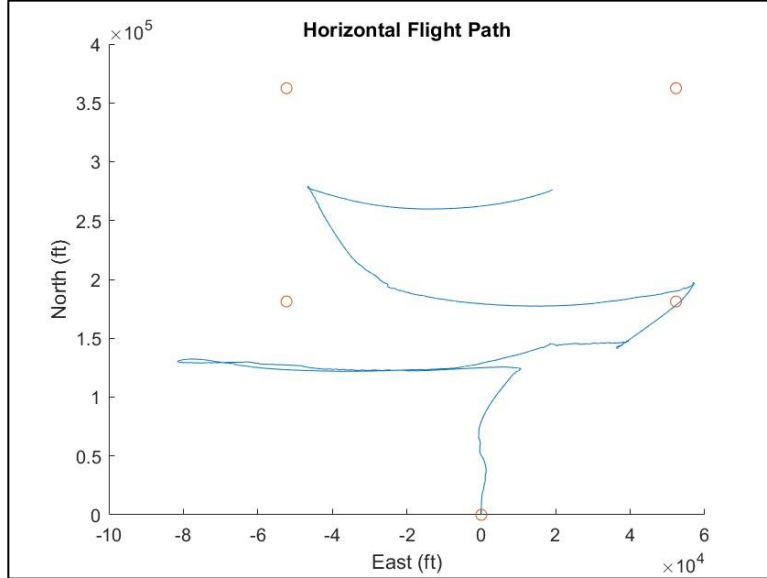


Figure 6-5: Horizontal Flight Path for Waypoint Navigation

The control gains were essentially randomized and produced the plots above. This was the result after many different iterations, across P, PI, PD, and PID controllers for each. Evidently, the control inputs are saturating quickly, and often. This would suggest that the gains are too large for almost every mode. Yet, each mode affects the other, so it is difficult to determine what to change. Most notably, while two waypoints are reached, the aircraft is essentially nose-diving and would crash into the ground before achieving the waypoints. In summation, the attempts to implement the controls into the waypoint simulation were unsuccessful and would require more time and tuning capabilities.

Conclusion

In summation, the F4 was an interesting aircraft to investigate, especially at a supersonic trim condition. The most notable characteristic, in the team's opinion, is the striking similarity between the linear and nonlinear models for small deflections. Even at supersonic conditions, the linearized model still provides amazing insight into the aircraft dynamics and serves as a good basis for developing controls. In the end, however, the control developed in this report cannot be said to be successful as it did not result in the aircraft completing its waypoint mission. To improve this, the team would suggest running optimization algorithms set with bounds like the controls found in the Autopilot Control Design section of the report. That way the algorithm can find optimal results. The performance metric for the optimization function could be the ratio of waypoints hit over the number of waypoints, as well as altitude held over the trim altitude. These two metrics could help determine a good starting point for further optimization.

Appendix

The following guide is structured similar to the zip file that was uploaded to canvas. The first number denotes the Deliverable folder the file can be found in.

Deliverable 1 Folder:

- 1.1 Deliverable1_TrimCond Trim conditions solver.
- 1.2 runsim_F4: File to run the nonlinear F4 model.
- 1.3 F4_6_DoF_runsim (Simulink): Full nonlinear F4 model.

Deliverable 2 Folder:

- 2.1 F4_linear_lat_runsim: Open loop analysis of linear lateral model with lateral doublets.
- 2.2 F4_linear_long_runsim: Open loop analysis of linear longitudinal model with longitudinal doublets
- 2.3 F4_runsim_alldeliv2: Combination of nonlinear and linear models to compare doublet simulations.
- 2.4 F4_linear_long_sim: Simulink linear longitudinal model.
- 2.5 F4_linear_lat_sim: Simulink linear lateral model.
- 2.6 F4_6DoF_runsim: Simulink full nonlinear model.

Deliverable 3 Folder:

- 3.1 desired_eigs_lat: Function to find desired lateral eigenvalues.
- 3.2 desired_eigs_long: Function to find desired longitudinal eigenvalues.
- 3.3 F4_linear_lat_SAS_runsim: File to run linear lateral model with stability augmentation.
- 3.4 F4_linear_lat_sim_SAS: Simulink linear lateral model with stability augmentation.
- 3.5 F4_linear_long_SAS_runsim: File to run linear longitudinal model with stability augmentation.
- 3.6 F4_linear_long_sim_SAS: Simulink linear longitudinal model with stability augmentation.
- 3.7 F4_runsim_deliv3: File to run nonlinear model with stability augmentation implemented.
- 3.8 F4_6DoF_runsim_SAS: Nonlinear Simulink model with stability augmentation.

Deliverable 4 Folder:

- 4.1 Roll_control_runsim: Code to drive the roll angle using aileron.
- 4.2 Sideslip_control_runsim: Code to control the sideslip using rudder.
- 4.3 Roll_Sideslip_control_runsim: Code that's integrated the roll and sideslip controls.
- 4.4 Altitude_Control_runsim: Code that maintains constant altitude using elevator.
- 4.5 Velocity_control_runsim: Code that maintains constant forward velocity by using thrust controller.
- 4.6 Altitude_velocity_control_runsim: Integrated model of the altitude and velocity control codes.
- 4.7 Lateral_control_roll_sideslip: Simulink model of the integrated controls affecting the lateral stability of the F4.
- 4.8 Longitudinal_control_altitude_velocity: Simulink Model of the integrated altitude and velocity controls.

Deliverable 5 Folder:

- 5.1 eval_perf: Function to determine the success of a Kp's for waypoint navigation.
- 5.2 Finding_Kps: Optimization algorithm to try and determine control gains.
- 5.3 runsim_F4_waypoint: File to run waypoint Simulink model.

5.4 F4_6DoF_runsim_waypoint_complete: Simulink model to follow waypoints.

References